Entrainment Coefficient of a Turbulent Plume

An Experimental Investigation with PIV and LIF

MSc Thesis

Dongliang Liu

Delft University of Technology

TU Delft

Entrainment Coefficient of a Turbulent Plume

An Experimental Investigation with PIV and LIF

by

Dongliang Liu

to obtain the degree of Master of Science
at the Delft University of Technology,
to be defended publicly on Monday, August 28, 2023, at 11:00.

Student number:	5466083
Thesis committee:	Prof.dr. Kamel Hooman, supervisor, TU Delft
	Dr.ir. Gerrit Elsinga, supervisor, TU Delft
	Dr.ir. Mark Tummers, TU Delft
	Dr. Domenico Lahaye, TU Delft
Place:	Delft, the Netherlands
Duration:	Nov., 2022 - Aug., 2023

Cover Image: A rising hot plume near the geothermal spa *Blue Lagoon* in Iceland.

TU Delft

Abstract

Buoyancy-driven plumes are natural phenomena that occur in widespread applications, such as geological flows or pollutant dispersion from a chimney. One characteristic of plumes is the entrainment process, where the plume stream drags in ambient fluid and mixes with the ambient fluid, and classic plume theory has used an entrainment coefficient to describe the entrainment process. Literature research reveals that there is a general lack of experiment data on the entrainment process of an axisymmetric plume, and there is little consensus on the entrainment coefficient. The *aims* of the thesis are to address the problem of insufficient experimental evidence and to investigate the entrainment coefficient using two theories (classic entrainment theory and new energy-consistent theory).

The thesis's *method* is experimental. Buoyancy-driven plumes with different initial conditions were created in a water tank, and the velocity field and buoyancy field were measured using particle image velocimetry (PIV) and laser induced fluorescence (LIF). In addition, a new combination of urea and sodium sulfate was proposed to perform the refractive index matching (RIM), which is a crucial step for accurate velocity and buoyancy measurements.

The thesis's *results* highlighted that the entrainment coefficient is approximately 0.11, despite large variations when using the classic theory to determine the entrainment coefficient, which may help explain different values in previous literature. In addition, the existence of a refractive index field was observed to affect both the velocity and buoyancy measurements. Specifically, the refractive index field caused PIV and LIF to overestimate the velocity field and underestimate the buoyancy field, respectively.

Keywords: buoyant plume, entrainment coefficient, PIV, LIF.

Acknowledgments

Time is fleeting. It's already been two years since I came to this beautiful country to embark on this amazing journey. As I am near the milestone of my journey, I would like to express my heartfelt appreciation to all those who have supported and guided me along the way.

First, I am grateful for the guidance from my supervisors, Prof.dr. Kamel Hooman and Dr.ir. Gerrit Elsinga. Their expertise, patience, and dedication have been instrumental in shaping the direction of this research and refining its outcomes.

I am also indebted to the supporting experts in the P&E lab. The experimental setup would not have been possible without the help of the optics engineer Edwin Overmars, the mechanical engineer Bart Hoek, and the chemical engineer Michel van den Brink.

I would also like to thank my friends for providing emotional support throughout this journey. Our friendship has made this experience memorable and enjoyable.

Last but not least, I want to express my deepest gratitude to my parents. Even though separated (geographically), their unwavering and unconditional love and encouragement have helped me to approach all ups and downs during the journey.

Dongliang Liu
August 14, 2023
Delft, the Netherlands

Contents

Nomenclature

Abbreviations

Abbreviation	Definition
PIV	Particle Image Velocimetry
LIF	Laser Induced Fluorescence
RIM	Refractive Index Matching
CFD	Computational Fluid Dynamics simulation
RANS	Reynolds-averaged Navier–Stokes equations

Symbols

Symbol	Definition	Unit
ϱ	Density	kg/m^3
Q	Volume Flux	m^3/s
M	Momentum Flux	m^4/s
F	Buoyancy Flux	m^4/s^3
B	Integral buoyancy	m^3/s^2
C	Concentration	g/l
$\mathcal{L}$	length scale of Large eddies	m
$\mathcal{U}$	characteristic velocity of large eddies	m/s
τ_{eddy}	eddy turnover time	s
τ_{trav}	eddy transverse time	s
τ_{avail}	available time window	s
ϑ	a scalar	-
α	Entrainment Coefficient	-
u_{e}	entrainment velocity	m/s
u_z	Vertical/streamwise velocity	m/s
u_r	radial velocity	m/s

Symbol	Definition	Unit
u_{zc}	Characteristic vertical/streamwise velocity	m/s
r_c	characteristics plume width	m
b	Buoyancy	m/s^2
b_c	Characteristics buoyancy	m/s^2
Γ	Richardson number/Plume parameter	-
Re	Reynolds number	-

List of Figures

List of Tables

1 Introduction

Plumes arise when a source steadily supplies buoyant forces, and plumes are a form of free-boundary flows that can evolve freely without any constraint. The study of plumes is important due to the widespread occurrence of plumes in different forms. This chapter unfolds the motivation for studying buoyancy-driven plumes and outlines the objectives of the thesis by reviewing the literature on plumes. §1.1 gives background information about the problem by describing the various plumes in daily life. After that, the available research about thermal plumes is retrieved and discussed in §1.2, and this section highlights several scientific gaps to be investigated. And finally, in §1.3, the three research objectives are formed based on the current scientific gaps.

1.1 The Omnipresent Plumes

Plumes are everywhere. On a large scale, a city can be regarded as a source that generates a thermal plume because the human activities in the city produce heat (known as the *urban heat island* effect), and the generated thermal energy can drive a flow of ambient air. Large-scale flow like this can be related to city ventilation or pollutant dispersion and therefore has received attention (Fan et al., 2020). On a smaller scale, the flow shown in Fig. 1.1 that expels from a chimney is also an example of various plumes.

Even bounded (natural convection) flows will finally become free-boundary plumes. In actual practice, all the boundaries are of finite size, meaning any flow must leave the boundary at some point and evolve in the form of a plume (Jaluria, 1980). Consider, for example, the radiators used for domestic heating. Although the air near the radiator surface may be regarded as natural convection bounded by a warm surface, the air above

the top of the radiator is a buoyant plume as there is no boundary to constrain the fluid motion.

Figure 1.1: Near the city of Delft, an outflow from a chimney is also a plume. As the plume keeps rising in the environment, it drags ambient air into itself, and arrows in the picture indicate the direction of the entrained air.

One characteristic of plumes is *entrainment*. Entrainment refers to the phenomenon that a plume can drag the ambient fluid into itself when it rises. In the previous chimney flow (Fig. 1.1), ambient air is continuously pulled into the rising plume, mixing with

the rising plume.

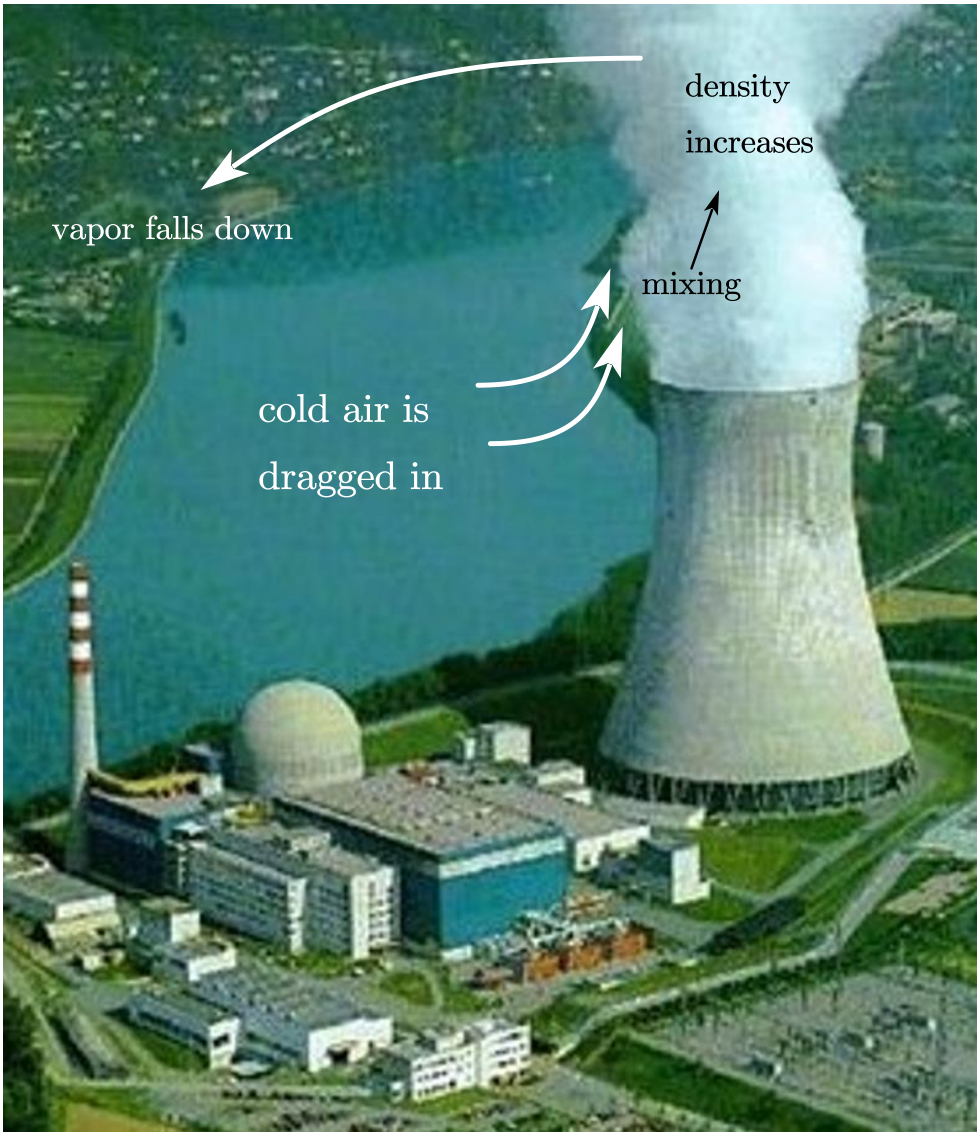

Figure 1.2: The water vapor coming out from the natural draft cooling tower drags ambient air and exchanges heat with the environment. Figure modified from Dey (2018).

Understanding the entrainment is necessary due to the widespread applications and occurrence of buoyant plumes. For instance, understanding the entrainment of a hot vapor plume is important in urban planning. If a natural cooling tower (Fig. 1.2) is constructed near a road, the water vapor (buoyant plume) may pose a problem. The hot rising water vapor will decrease its temperature due to the continuous mixing of cold ambient air entrained by the plume. As the bulk temperature of the plume drops continuously, the plume's density will increase up to a point when the buoyancy forces (caused by density difference) can no longer sustain the plume's rising. The dense and moist air will then fall down onto the road at some distance, causing the road to be slippery

and dangerous if severe weather conditions are encountered. Hence, the entrainment process of thermal plumes warrants a closer look, and we shall continue our journey by reviewing some available studies.

1.2 Previous Research on Thermal Plumes

The research on a buoyant plume is not easy due to the complexity of the coupled governing equations. The three governing equations are the continuity equation, momentum equation, scalar conservation equation (temperature or species concentration):

$$\frac{\partial \varrho}{\partial t} + \nabla \cdot (\varrho \mathbf{u}) = 0, \tag{1.1}$$

$$\frac{\partial (\varrho \mathbf{u})}{\partial t} + \nabla \cdot (\varrho \mathbf{u}\mathbf{u}) = -\nabla p + \mu \nabla^2 \mathbf{u} + \varrho \mathbf{g}, \tag{1.2}$$

$$\frac{\partial (\varrho \vartheta)}{\partial t} + \nabla \cdot (\varrho \vartheta \mathbf{u}) = \nabla \cdot (D_{\text{diff}} \nabla \vartheta) + q_\vartheta, \tag{1.3}$$

where ϱ is the density, t is the time, $\mathbf{u}$ is the velocity vector, p is the pressure, μ is the dynamics viscosity, $\mathbf{g}$ is the gravitational vector, ϑ is the quantity of the passive scalar, D_{diff} is the diffusivity (or the diffusion coefficient) for the passive scalar ϑ, and q_ϑ is the source or sink of ϑ. As mentioned earlier, a plume is driven by buoyancy forces fueled by density differences; furthermore, the density itself is a function of temperature (or concentration). This means that the governing equations are coupled together by the variation of density ϱ. In other words, it is impossible to solve the momentum equation without solving the energy equation; while the energy equation is affected by the momentum equation (because it can alter the heat transfer rate).

In general, these highly coupled elliptic governing equations are difficult to solve analytically, and this fact has promoted many researchers to use other approaches. Roughly speaking, the research themes can be divided into three categories. Some researchers tried simplifying the governing equation by introducing extra assumptions, while others resorted to numerical and experimental methods. We begin our discussion by introducing several simplified analytical models.

1.2.1 Simplified Theoretical Models of Thermal Plume

Various proposed theoretical models intend to simplify the governing equations of a thermal plume, and these models, later on, constituted the classic plume theory (Kaye, 2008). For example, one possible simplification for a laminar plume was proposed by Gebhart et al. (1970) and Jaluria (1980), in which the Boussinesq approximation for density variation and the assumption that the temperature distribution is in a power

law form were used. The macro energy balance can be applied to determine the constants in the temperature power-law profile, and a self-similar solution may be obtained. The results show that the maximum temperature in the plume decreases with plume height z, and has a relation of $z^{-5/3}$, while the mass flow rate increases at the same rate (Gebhart et al., 1970).

The emergence of the so-called MTT model marked one of the milestones in the development of plume theory. Morton et al. (1956) argued that the above model cannot be used to analyze turbulent plumes. Therefore, Morton et al. (1956) introduced another model, later known as the MTT model, which considers the turbulent entrainment by assuming that the entrainment is proportional to the turbulent plume's vertical velocity with a constant entrainment coefficient α. Furthermore, by assuming density variation is small compared with the ambient density and incompressible flow, they were able to rewrite mass conservation Eq. (1.1) as volume conservation and consider density changes only in terms associated with buoyancy forces (e.g., consider density variation only in $\varrho\mathbf{g}$ and energy equation). Rewriting the energy equation as conservation of density deficiency and considering only *time-averaged (quasi-steady)* motions, the governing equations now simplify to a set of ODEs:

$$\frac{dQ}{dz} = 2\alpha M^{1/2}, \quad \frac{dM}{dz} = \frac{QF}{M}, \quad \frac{dF}{dz} = -N^2 Q, \tag{1.4a,b,c}$$

where the entrainment coefficient α is an assumed closure model for a turbulent plume problem, and it dictates that entrainment velocity u_e is proportional to the mean vertical velocity u_z at any given height, namely

$$u_\mathrm{e} = \alpha u_z. \tag{1.5}$$

The volume flux Q, momentum flux M, buoyancy flux F, and buoyancy frequency N^2 are defined respectively as

$$Q \equiv 2\int_0^\infty u_z\,(r,z) r dr, \quad M \equiv 2\int_0^\infty u_z^2\,(r,z) r dr, \tag{1.6a,b}$$

$$F \equiv 2\int_0^\infty u_z\,(r,z) b(r,z) r dr, \quad N^2 \equiv -\frac{g}{\varrho_\mathrm{e}}\frac{d\varrho_\mathrm{e}}{dz}. \tag{1.6c,d}$$

In above equations $b = \frac{g(\varrho-\varrho_\mathrm{e})}{\varrho_0}$, where ϱ_e is the environment density and ϱ_0 is the reference density (which is the ambient density at the same altitude as the source). Note that the buoyance frequency $N^2 = 0$ if there is no stratification.

The simple yet powerful entrainment coefficient α is the key ingredient that makes the MTT model so successful in classic plume theory. Not only can the model give

predictions on a plume's vertical velocity and identifies the maximum height the plume can reach (Morton et al., 1956), but it also promotes many other studies based on it. Scase et al. (2006), for example, based on a modification of the MTT model and presented another analytic solution for the forced plume with a time-varying source strength. One may refer to Kaye (2008) and Woods (2010) for a more comprehensive review of these works.

However, it turned out that the exact value of the coefficient α would later be the center of disagreement over many years. Richardson and Hunt (2022) summarized several previously measured entrainment coefficient results and found that the variation of entrainment coefficients could be up to 100%, warning that the choice of two different entrainment coefficients can lead to up to a 60% difference in the MTT predicted distance at which the buoyancy of the plume has decreased to a certain value. Parker et al. (2020) also mentioned that there exists a significant disagreement in the entrainment coefficient. The review work by Kaye (2008) also considered determining the entrainment coefficient as one open question.

As a result, many theorists tried to devise new methods to reconcile the different entrainment coefficients in different studies. These theorists seemed to follow two different approaches. Following the original approach adopted by Morton et al. (1956), Richardson and Hunt (2022) created a method to assess the measurement in existing literature to identify why there are variations, concluding that the entrainment coefficient should be $\alpha = 0.11 \pm 15\%$. Other theorists adopted another approach, which was first outlined by Priestley and Ball (1955), in an attempt to link turbulent kinetic energy with the entrainment process. Reeuwijk and Craske (2015) further developed the idea and discussed restrictions on the entrainment coefficient from the perspective of turbulent kinetic energy. Craske et al. (2017) also derived a new expression for the entrainment coefficient from the perspective of squared mean buoyancy. It should be noted, however, that the above two approaches can be related to each other (as the entrainment process is invariant no matter what approach to be adopted), and Fox (1970) presented the discussion about the link between the two approaches.

Nonetheless, lacking experimental data is a general problem in verifying the validity of the above theories. To the author's best knowledge, there is limited and restricted experimental knowledge that can provide support for the above theories. On the one hand, even the inventor of the above theories called for observational studies to confirm their theories (Craske et al., 2017); on the other hand, Richardson and Hunt (2022) mentioned the scarcity of available comprehensive data, which makes re-using the existing data to test the newly-developed theories difficult. This point of insufficient supporting evidence shall become more straightforward after reviewing available experimental and

numerical studies.

1.2.2 Experimental/Numerical Studies on Entrainment Coefficient

Less than 20 pertinent research papers were found after literature retrieval. In order to retrieve studies that focused on the entrainment coefficient, the following search operators were used: {[(buoyant plume) AND (entrainment coefficient)] OR [(thermal plume) AND (entrainment coefficient)]}. Among the total 425 results returned from Scopus and Web of Science, only 19 papers are highly relevant to the current topic. After excluding theoretical studies from the 19 papers, only 11 papers (either experimental or numerical studies) are left, and the details of these papers are summarized in table 1.1.

Table 1.1: Summary of available experimental/numerical studies on entrainment coefficient. In the approach column, the "O" approach means the original MTT approach mentioned in §1.2.1, which measures the entrainment coefficient based on the volume flux change; and the "N" approach refers to the newly-developed method that evaluates the entrainment coefficient with a focus on turbulent statistics. In the category column, the "E" stands for experimental study, while the "N" refers to numerical study.

Author	Category	Methodology	Approach
Ramaprian and Chandrasekhara (1989)	E	LDA + thermistor.	O
Kumar et al. (1996)	E	Pressure tubes + concentration measurement.	O
Contini et al. (2011)	E	Quantitative plume visualizations with neon lighting.	O
Dadonau et al. (2019)	E	conductivity sensor and thermocouple.	O
Ezzamel et al. (2015)	E	PIV + thermocouple.	O
Milton-McGurk et al. (2022)	E	PIV + LIF.	N
Zhang et al. (2017)	E	PIV + density measurement at different locations.	O
Dellino et al. (2014)	E & N	image/video analysis.	O
Kewalramani et al. (2022)	N	Large eddy simulation.	N
Abdalla et al. (2009)	N	Large eddy simulation.	O
Plourde et al. (2008)	N	Direct numerical simulation.	NA

Indeed, the above review of available research on the plume entrainment coefficient confirms the scientific gap that there is limited observational evidence to confirm newly-developed theories. Except for the latest study by Milton-McGurk et al. (2022), all other experimental studies adopted the original method to analyze the entrainment coefficient; however, the focus of Milton-McGurk et al. (2022) was on negative buoyant jets and fountains (not plumes). Hence, the scientific gap still exists. The author attributes the

scientific gap to insufficient access to high spatial resolution measurement techniques (such as PIV or LIF) because all the recently developed theories require measurements of turbulent quantities at a reasonable spatial resolution, which might not be possible for earlier studies (Mayinger et al., 2001).

Besides reaffirming the above scientific gap, the review further reveals two interesting facts. The first fact is that some numerical studies have already shed light on the current study. As a strong example, the LES study by Kewalramani et al. (2022) analyzed the entrainment coefficient in axisymmetric plumes from the perspective of turbulent kinetic energy and compared the result against the original method, concluding that the two results agree reasonably well with each other. As another example, the numerical study by Abdalla et al. (2009) also gave some insight into the entrainment mechanism of thermal plumes: they observed that small packets/eddies of hot fluid detach from the main plume stream and then encompass the cold ambient fluid. Hence, observations by Abdalla et al. (2009) suggested that the entrainment coefficient should be linked with turbulent quantities, and one should not separate entrainment coefficient measurement from the measurement of turbulent statistics as was done so in many previous measurements (the "O" approach in table 1.1). Still, it should be noted that there are limited experimental studies to confirm either these numerical results or the theoretical results mentioned above.

The second fact is that some experimentalists began to address the dependence of the entrainment coefficient on the Richardson number Γ, despite lacking accurate measurement. The Richardson number Γ is defined as

$$\Gamma = \frac{5FQ^2}{2^{7/2}\pi^{1/2}\alpha_{\mathrm{p}}M^{5/2}}, \tag{1.7}$$

where α_{p} is the entrainment coefficient of a pure plume. Historically, theorists first noticed the dependence of the entrainment coefficient α on Γ. At an earlier time, Morton and Middleton (1973) used the Richardson number at the plume source Γ_0 to distinguish different plumes, where Γ_0 provides a measure of the relative strength of initial momentum flux and buoyancy flux: for $0 < \Gamma_0 < 1$, the plume is termed as a *forced plume*; for $\Gamma_0 > 1$, the plume is termed as a *lazy plume*; while for $\Gamma_0 = 1$, the plume is termed as a *pure plume*. More recently, in their theoretical modeling, Reeuwijk and Craske (2015) pointed out the dependence of the entrainment coefficient on the Γ. Nevertheless, these theoretical conclusions were never tested experimentally until Ezzamel et al. (2015). Ezzamel et al. (2015), to the best of the author's knowledge, was the first to experimentally address the problem; in their paper, they used PIV and thermocouple to determine the entrainment coefficient and measure the local Γ. By varying the source strength (particularly the momentum), they were able to obtain different Γ. It was observed that force

plume and jet both tend to become pure plume as they evolve (Γ becomes unity), and local Γ alters α directly and indirectly by changing turbulence (yet no clear link was offered). Ezzamel et al. (2015) also motivates the current study due to two facts. First, their buoyancy measurement was of low spatial resolution: they used a thermocouple array (thermocouples in a row at a spacing of 10 mm) to measure the buoyancy profile, and this method has a relatively low spatial resolution which might result in a wrong interpretation of buoyancy profile (and thus the local Γ). Second, since they would need to insert the thermocouple array into the plume, they had to measure the temperature and velocity separately; however, it is not clear if separate measurements of velocity and temperature could be under different ambient conditions, as they recognized that background flow is a noise source (Ezzamel et al., 2015).

It is evident that the previous literature review (on either theoretical or experimental/numerical studies) shows several scientific gaps to be filled, and these gaps motivate the current study. Still, it would be helpful to formulate and summarize the research objectives formally before proceeding to the methodology of the current study.

1.3 Research Objectives

The current study has, in total, three research objectives based on different scientific gaps and motivations. The first objective is to *measure the entrainment coefficient of an axisymmetric plume* with state-of-the-art measurement techniques. This objective is intended to address the problem of the general lack of experimental data mentioned by Richardson and Hunt (2022). By doing so, the current study hopes to provide the classic plume theory with more experimental evidence.

The second objective of the current study is to *confirm the validity of the recently-conceived theories*, as there is limited experimental support for for entrainment coefficient measurements (Craske et al., 2017; Reeuwijk & Craske, 2015). By reassuring the new theories that can predict the entrainment coefficient, the objective is expected to improve the reliability of the widespread usage of the classic plume theory.

The third objective is to *investigate the dependence of the entrainment coefficient α on the local Richardson number Γ*. Despite one emerging experimental study on determining such a dependence relation (Ezzamel et al., 2015), there is still a lack of accurate knowledge on how α could be related to Γ; and the object aims to shed light on the point.

2 Methodology

The previous chapter outlined the research gaps in previous studies and the research objectives of the current thesis. The focus of this chapter is to discuss the methodology of the thesis, including theories behind the experimental setup, how could the turbulent plume be created, and how the measurement may be performed. §2.1 will formally introduce the new theory used for entrainment coefficient measurement, which will also be the theoretical basis for choosing proper measurement methods for the experiment. §2.2 explains the creation of a turbulent plume in a water tank. Finally, §2.3 and §2.4 discuss the measurement techniques in detail and address possible measurement uncertainty.

2.1 Theoretical Basis for Entrainment Coefficient

This section gives a review of the theory for entrainment coefficient measurement in turbulent plumes and motivates the choice of measurement techniques. Although the definition of the entrainment coefficient of a turbulent plume was introduced in chapter 1, no knowledge about its measurement has been discussed. This section first delineates relevant theories used in entrainment coefficient measurements in §2.1.1, and then examines different measurement techniques and selects the proper measurements for our experiment in §2.1.2.

2.1.1 Relevant Theories for Turbulent Plumes

Turbulent and Laminar Plumes

The magnitude of the Reynolds number determines whether a plume, created by releasing/injecting a solution with a density difference in a water tank, is laminar or turbulent. The liquid-liquid injection experiment done by Reynolds (1962) showed that the flow regime remains laminar only when $Re = \frac{\varrho u d}{\mu} \lesssim 30$ (here ϱ is the density, u is the velocity, d is the diameter of the nozzle, and μ is the dynamic viscosity). It should be noted that the numeric value is an approximate value, and the exact values of transition to turbulence vary from experiment to experiment; what matters is the order of magnitude.

In the current study, the magnitudes of Reynolds number at the inlet will be hundreds (200 to 700), which means the plume will be turbulent. However, it should be noted that both a laminar plume and a turbulent plume can entrain ambient fluid, where the laminar plume entrains fluid by viscous drag, while the turbulent counterpart shows a more complex entrainment pattern (Davidson, 2004). We start our journey toward the entrainment coefficient with the different scales presented in a turbulent plume.

Various Scales in Turbulent Plumes

A turbulent plume is characterized by various scales, and these scales prove useful when designing the experiment (Fig. 2.1). In general, there are two types of scales in turbulence, the first type being length scales and the second being time scales. Both types are important for the design of the experiment. Length scales, for example, are useful when choosing the measurement region so that measurements can fully cover the plume stream. Time scales are useful when determining the measurement acquisition time; for instance, a short measurement may not be sufficient to converge the flow field when time-averaged quantities are concerned.

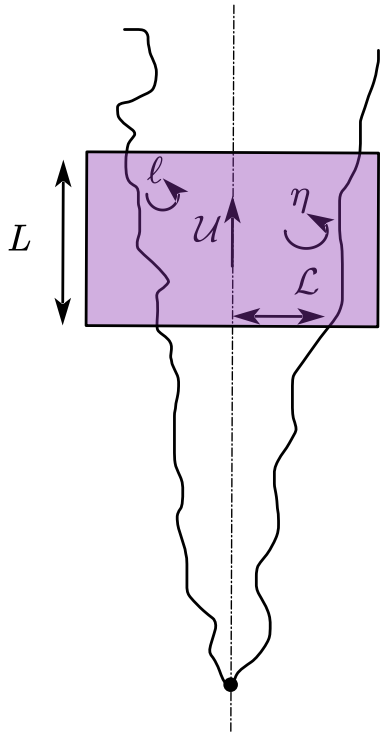

Figure 2.1: Various scales in a plume.

There are a series of length scales associated with turbulence to describe various sizes of eddies. For the macroscale, there are large eddies whose dimensions are comparable to the plume half-width $\mathcal{L}$, and those large eddies usually have a characteristic velocity of the mean flow velocity $\mathcal{U}$ (Nieuwstadt et al., 2016). In a jet, $\mathcal{U}$ will be on the same order of magnitude as the centerline velocity.

For the microscale, the smallest eddies for energy dissipation usually have length scales comparable to the *Kolmogorov scale* η. The Kolmogorov scale is defined as

$$\eta \simeq \left(\frac{\nu^3}{\epsilon}\right)^{\frac{1}{4}}, \tag{2.1}$$

where ϵ is the dissipation rate of turbulent kinetic energy. Since all the kinetic energy has to be dissipated on the smallest scale, the dissipation rate (in equilibrium conditions) can be calculated by

$$\epsilon \simeq \frac{\mathcal{U}^3}{\mathcal{L}}. \tag{2.2}$$

Similar to the small eddies for energy dissipation, there are tiny eddies responsible for the molecular diffusion of a scalar. These little eddies act to smooth out the different concentrations, and their length scale is usually called the Batchelor length scale (Paul

et al., 2004), defined by

$$\ell \simeq \left(\frac{\nu D^2}{\epsilon}\right)^{\frac{1}{4}}. \tag{2.3}$$

It should be noted that the ratio of Kolmogorov scale to the Batchelor scale is the square root of the Schmidt number, namely $\frac{\eta}{\ell} \simeq Sc^{1/2}$, which implies that the Kolmogorov scale is greater than the Batchelor scale for mixtures with a large Sc.

Besides all the above length scales, there are also various time scales. Among the different time scales, three temporal scales prove to be useful in our experiment. The first time scale is the *eddy turnover time*, which is the time required for one large eddy to break up into smaller eddies or the time needed for a large eddy with energy $\sim \mathcal{U}^2$ to lose its energy (Nieuwstadt et al., 2016). Therefore, the eddy turnover time may be estimated as

$$\tau_{\text{eddy}} \simeq \frac{\mathcal{L}}{\mathcal{U}}. \tag{2.4}$$

It was mentioned in §1.2.1 that the description of the entrainment coefficient presumes that the flow is quasi-steady, and this fact put a restriction on the measurement time: *The time duration to perform the measurement has to be larger than the eddy turnover time*, so that when taking time average, the measurement results converge statistically and represent a quasi-steady description of the flow.

The second time scale worthy of attention is the *eddy transverse time* (Richardson & Hunt, 2022). For the measurement to correctly capture the quasi-steady description of the flow, the measurement *time window should be able to fully record the history of every eddy in the measurement region*. In other words, the measurement time should be long enough to record one eddy from first entering the measurement region to leaving the measurement region. The time required for any eddy to pass the measurement region is called the eddy transverse time

$$\tau_{\text{trav}} \simeq \frac{L}{\mathcal{U}}, \tag{2.5}$$

where L is the length of the measurement window (Fig. 2.1). One should not confuse L with $\mathcal{L}$, where $\mathcal{L}$ is the macro length scale for large eddies.

The last time scale is the *available time window* τ_{avail}. There are two factors that may limit the available measurement window, one being the plume collapsing and the other being the "filling-box" effect. The plume collapse phenomenon was analyzed previously in §1.1, and a straightforward visualization of such a collapsing phenomenon in a lab setting was provided by Carey et al. (1988). The "filling-box" effect refers to the accumulation of plume fluid, and this problem can become dominant when the experiment setup is of finite size (Turner, 1973). Both the collapsing and "filling-box" effects may limit the available measurement time by making it harder to distinguish the plume fluid

from the ambient fluid. Unfortunately, there is no direct way to estimate the available time. As a result, we will use flow visualization to estimate the available time, and it will be shown that the "filling-box" effect is the prime factor that puts an upper bound on τ_{avail}.

Transport of a Scalar

It is important to understand the transport of the scalar before deriving the entrainment relation since the plume is, ultimately, fueled by a scalar. Recall that in chapter 1, it was explained that the density difference drives the plume. In practice, the density difference is related to some other scalar—be it the temperature of the fluid or the concentration of a chemical species. In our case, the scalar will be the concentration C of a dilute solution (the reason for choosing concentration rather than temperature as the buoyancy source will be discussed later in §2.2.)

For the transportation of species concentration C, the conservation equation, namely Eq. (1.3), simplifies to the convection-diffusion equation (Bejan, 2013):

$$\frac{\partial C}{\partial t} + \mathbf{u} \cdot \nabla C = D \nabla^2 C, \tag{2.6}$$

where D is the mass diffusion coefficient of the species in solution. The underlying assumptions of the above equation are that the flow is incompressible, there are no sources or sinks for the species, and the diffusion coefficient D is constant. The first assumption is valid because the experiment would be held in a water tank, and water is clearly incompressible in the experiment. The second assumption is correct since there is no chemical reaction during the plume rising, and only advection and diffusion are present in the species transport. Finally, the mass diffusivity can be considered as a constant because the solution in our experiment will be a dilute solution, and there will be no temperature changes (Wilke & Chang, 1955).

Now that the governing equation is simplified a little bit, one can start deriving the entrainment relations. As mentioned in the previous chapter, there are two distinct approaches to the formulation of entrainment calculation: One is called the "original" approach (Morton et al., 1956), while the other is called the "newly-developed" approach (Reeuwijk & Craske, 2015). We start by discussing the new approach.

New Approach to Calculating Entrainment Coefficient

To derive the relation for the calculation of the entrainment coefficient, one has to relate the coordinate-free governing equations of a turbulent plume (Eqs. 1.1 to 1.3) to the MTT model equations (Eqs. 1.4). Since the plume will be created using a round nozzle, the plume will be an axisymmetric plume shown in the following figure.

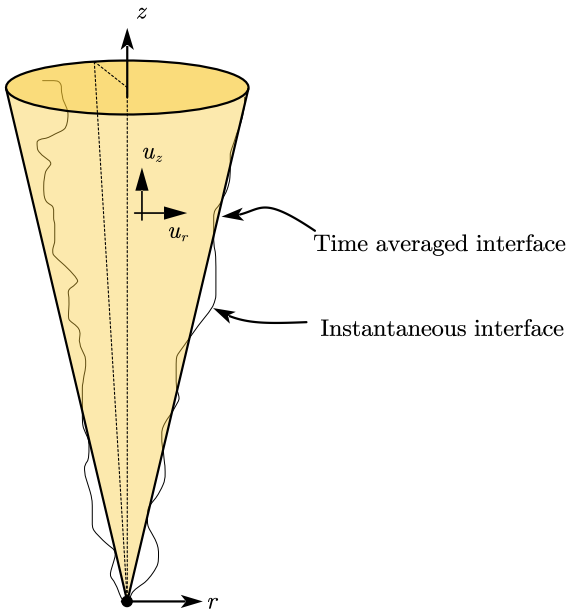

Figure 2.2: The sketch of a time-averaged plume from a point source is axisymmetric.

It is better to rewrite the coordinate-free governing equations using a cylindrical coordinate system for the plume. In other words, the operator $\mathbf{u}\cdot\nabla = u_r\frac{\partial}{\partial r} + \frac{u_\theta}{r}\frac{\partial}{\partial\theta} + u_z\frac{\partial}{\partial z}$ and $\nabla^2 = \frac{1}{r}\frac{\partial}{\partial r}\left(r\frac{\partial}{\partial r}\right) + \frac{1}{r^2}\frac{\partial^2}{\partial\theta^2} + \frac{\partial^2}{\partial z^2}$. Now the continuity equation (Eq. 1.1) becomes

$$\frac{\partial \varrho}{\partial t} + \frac{1}{r}\frac{\partial}{\partial r}(r u_r) + \frac{\partial u_z}{\partial z} = 0, \tag{2.7}$$

the momentum equation in the z-direction (Eq. 1.2) becomes

$$\frac{\partial u_z}{\partial t} + u_r\frac{\partial u_z}{\partial r} + \frac{u_\theta}{r}\frac{\partial u_z}{\partial\theta} + u_z\frac{\partial u_z}{\partial z} = -\frac{1}{\varrho}\frac{\partial p}{\partial z} + \nu\left\{\frac{1}{r}\frac{\partial}{\partial r}\left(r\frac{\partial u_z}{\partial r}\right) + \frac{1}{r^2}\frac{\partial^2 u_z}{\partial\theta^2} + \frac{\partial^2 u_z}{\partial z^2}\right\} + g\frac{C}{C_0} \tag{2.8}$$

where C_0 is the reference concentration and the conservation equation of species transport (Eq. 2.6) becomes

$$\frac{\partial C}{\partial t} + u_r\frac{\partial C}{\partial r} + \frac{u_\theta}{r}\frac{\partial C}{\partial\theta} + u_z\frac{\partial C}{\partial z} = \frac{D}{\varrho}\left[\frac{1}{r}\frac{\partial}{\partial r}\left(r\frac{\partial C}{\partial r}\right) + \frac{1}{r^2}\frac{\partial^2 C}{\partial\theta^2} + \frac{\partial^2 C}{\partial z^2}\right]. \tag{2.9}$$

In accordance with the methodology outlined by Reeuwijk and Craske (2015), one can apply Reynolds decomposition to rewrite the governing equation with the Boussinesq approximation and the assumption of neglecting viscous effects (see Appendix A for the derivation):

$$\frac{1}{r}\frac{\partial}{\partial r}(r\overline{u_r}) + \frac{\partial \overline{u_z}}{\partial z} = 0, \tag{2.10}$$

$$\frac{1}{r}\frac{\partial}{\partial r}\left(r\overline{u_z u_r}+r\overline{u_z' u_r'}\right)+\frac{\partial}{\partial z}\left(\overline{u_z u_z}+\overline{u_z' u_z'}\right)=-\frac{\partial \overline{p}}{\partial z}+\frac{g}{C_0}\overline{C}, \tag{2.11}$$

$$\frac{1}{r}\frac{\partial}{\partial r}\left(r\overline{u_z}\,\overline{C}+r\overline{u_z' C'}\right)+\frac{\partial}{\partial z}\left(\overline{u_z}\,\overline{C}+\overline{u_z' C'}\right)=0. \tag{2.12}$$

Furthermore, the turbulent kinetic energy may be derived as:

$$\begin{aligned}\frac{1}{r}\frac{\partial}{\partial r}\left(r\overline{u_r}(\overline{u_z})^2+2r\overline{u_r' u_z'}\,\overline{u_z}\right)+\frac{\partial}{\partial z}\left(\overline{u_z}^3+2\overline{u_z'^2}\,\overline{u_z}+2\overline{p u_z}\right)\\ =2\overline{u_r' u_z'}\frac{\partial \overline{u_z}}{\partial r}+2\overline{u_z'^2}\frac{\partial \overline{u_z}}{\partial z}+2\overline{p}\frac{\partial \overline{u_z}}{\partial z}+2\overline{u_z}\frac{g}{C_0}\overline{C}.\end{aligned} \tag{2.13}$$

Integrating Eqs. 2.10 –2.13 over r will give a result similar to Eqs. 1.4 but with some profile coefficients

$$\begin{cases}\frac{dQ}{dz}=2\alpha M^{1/2},\\ \frac{d}{dz}\left(\beta_g M\right)=\frac{QF}{\theta_m M},\\ \frac{d}{dz}\left(\frac{\theta_g}{\theta_m}F\right)=0,\\ \frac{\mathrm{d}}{\mathrm{d}z}\left(\gamma_g\frac{M^2}{Q}\right)=\delta_g\frac{M^{5/2}}{Q^2}+2F.\end{cases} \tag{2.14}$$

where the profile coefficients are given by

$$\begin{aligned}&\beta_m\equiv\frac{M}{u_{zc}^2 r_C^2}\equiv 1,\ \beta_f\equiv\frac{2}{u_{zc}^2 r_C^2}\int_0^\infty\overline{u_z'^2}r\mathrm{d}r,\ \beta_p\equiv\frac{2}{u_{zc}^2 r_C^2}\int_0^\infty\overline{p}rdr,\\ &\gamma_m\equiv\frac{2}{u_{zc}^3 r_C^2}\int_0^\infty\overline{u_z}^3 rdr,\ \gamma_f\equiv\frac{4}{u_{zc}^3 r_C^2}\int_0^\infty\overline{u_z}\,\overline{u_z'^2}rdr,\ \gamma_p\equiv\frac{4}{u_{zc}^3 r_C^2}\int_0^\infty\overline{u_z p}rdr,\\ &\delta_m\equiv\frac{4}{u_{zc}^3 r_C}\int_0^\infty\overline{u_z' u_r'}\frac{d\overline{u_z}}{dr}rdr,\delta_f\equiv\frac{4}{u_{zc}^3 r_C}\int_0^\infty\overline{u_z' u_z'}\frac{\mathrm{d}\overline{u_z}}{dz}rdr,\delta_p\equiv\frac{4}{u_{zc}^3 r_C}\int_0^\infty\overline{p}\frac{\mathrm{d}\overline{u_z}}{dz}rdr,\\ &\theta_m\equiv\frac{F}{u_{zc}b_c r_C^2},\ \theta_f\equiv\frac{2}{u_{zc}b_c r_C^2}\int_0^\infty\overline{u_z' c'}rdr,\\ &\beta_g=\beta_m+\beta_f+\beta_p,\ \gamma_g=\gamma_m+\gamma_f+\gamma_p,\ \delta_g=\delta_m+\delta_f+\delta_p,\end{aligned} \tag{2.15}$$

and the characteristics plume width r_c, velocity u_{zc}, and buoyancy b_c are

$$r_c=\frac{Q}{M^{1/2}},\ u_{zc}=\frac{M}{Q},\ b_c=\frac{BM}{Q^2},B\equiv 2\frac{g}{C_0}\int_0^\infty\overline{C}rdr. \tag{2.16}$$

Finally, the entrainment coefficient is obtained by considering the restriction posed by the overdetermined governing equations, Eqs. 2.14, as there are four equations for three variables Q, M, F:

$$\alpha=-\frac{\delta_g}{2\gamma_g}+\left(\frac{1}{\beta_g}-\frac{\theta_m}{\gamma_g}\right)\frac{8\alpha_{\mathrm{p}}\beta_g}{5}\Gamma+\frac{Q}{2M^{1/2}}\frac{d}{dz}\left(\log\frac{\gamma_g}{\beta_g^2}\right), \tag{2.17}$$

where Γ is the local Richardson number defined in Eq. 1.7. If the pressure effect is

neglected and the mean flow is self-similar, the entrainment relation further simplifies to

$$\alpha = -\frac{\delta_m}{2\gamma_m} + \left(1 - \frac{\theta_m}{\gamma_m}\right)\frac{8\alpha_\mathrm{p}}{5}\Gamma \tag{2.18}$$

Eq. 2.18 will be the entrainment relation for the evaluation of our experimental data. The discussion of choosing measurement techniques will be presented in the next subsection §2.1.2 based on the formulation of Eq. 2.18.

Old Approach to Calculating Entrianment Coefficient

The old approach considers the entrainment coefficient evaluation in a rather straightforward way, drastically simplifying a complicated entrainment process. Combine the definition of volume flux, namely Eq. 1.4, with the characteristic scales Eqs. 2.16 to give

$$\frac{dQ}{dz} = 2\alpha M^{1/2} = 2\alpha r_c u_{zc},$$

or

$$\alpha = \frac{1}{2M^{1/2}}\frac{dQ}{dz}, \tag{2.19}$$

where the quantities needed to determine the entrainment coefficient can be obtained from the velocity measurement alone. It should be noted that the definitions of r_c and u_{zc} do not depend on any presumed velocity profile according to Eqs. 2.16 yet several previous studies used the distance in which the velocity drops to $1/e$ of the centerline velocity u_{zc} as the value for r_c (Paillat & Kaminski, 2014; Richardson & Hunt, 2022).

2.1.2 Measurement of Turbulent Plume

It was shown that the calculation of the entrainment coefficient α requires the measurement of the velocity and buoyancy profiles. Therefore, choosing proper measurement techniques for data acquisition is very important. A brief overview of velocity and concentration measurement will be given first, and then proper techniques will be chosen based on the formulation of the entrainment coefficient relation (Eqs. 2.18 and 2.19).

Velocity Measurement

There are a lot of velocity measurements available. Common techniques for velocity measurements are Pitot–Static pressure probe, thermal anemometry, doppler anemometry, and particle image velocimetry (PIV) (Figliola & Beasley, 2014).

For the measurement of the velocity field, PIV proves to be suitable. The Pitot–Static pressure probe is not suitable for the velocity measurement because of the invalid underlying assumptions that the density is a constant. Thermal anemometry should better be avoided because the technique is an intrusive measurement and it may disturb the plume. LDA cannot be applied due to the time window limit mentioned in §2.1.1.

LDA is a point-wise measurement, and measuring multiple positions means one has to move the measurement volume by a traverse system. According to the author's experience with LDA, measuring dozens of points could easily take ten minutes, which exceeds the available time window τ_{avail} described in §2.1.1. Therefore, it is preferable to choose PIV as the velocity field measurement technique.

Particle image velocimetry (PIV) is an non-intrusive optical measurement for flow velocity (Raffel et al., 2018). The technique illuminates the flow field (seeded with particles) with a laser sheet and then takes two images of the flow field consecutively in a short time, where the particles on the image would appear as white spots (Fig. 2.3). Cross-correlation is then used to determine the small displacement of a particle on the two images. With the known separation time, which is the time interval in which two images are taken, the velocity of the whole flow field can be calculated. PIV is an advanced technology to measure the velocity of the whole flow field without affecting the flow. Yet, care must be taken to ensure that particles can faithfully follow the actuall flow and the image quality is high.

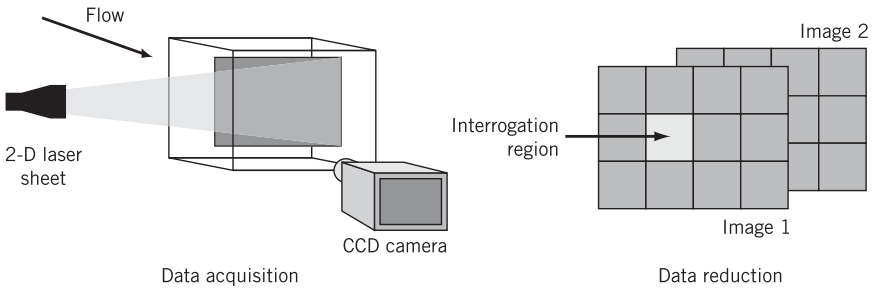

Figure 2.3: The sketch of a PIV system (Figliola & Beasley, 2014).

Concentration Measurement

Two possible approaches can lead to the measurement of concentration. This first approach measures the concentration using probes, while the second method measures the concentration of specific species directly by optical methods.

The probe-based methods utilize the fact that the electrical properties of the fluid are closely related to the concentration of salt concentration (Gavish & Promislow, 2016); namely, by measuring the electrical properties, one may deduce the concentration information. For the measurement of electrical properties of salt solutions, two methods have been used, including conductivity meters and Impedance spectroscopy.

The optics-based method tries to visualize and quantify the concentration of chemical species directly. Since chemical species' concentration can change the optical properties of the fluid, one can obtain the flow information by analyzing the optical images of the flow field. These methods include shadowgraphy, interferometer, Schlieren method, or

laser induced fluorescence (LIF).

For the measurement of the concentration field, direct measurement using LIF would be a better choice than the other options. First, all the probe-based measurement options (namely, conductivity sensor or impedance spectroscopy) are intrusive. Since inserting a probe may disturb the flow, introduce noises, and affect the measurement of PIV, it is proper to choose a non-intrusive method. Second, while all the optical others are non-intrusive measurement techniques, LIF would be the better choice for concentration measurement. It is hard to quantify the density field with the shadowgraph, and therefore shadowgraph is not suitable for our purposes. The many difficulties with the interferometer setup prevent it from being the best choice. The Schlieren method is to be ruled out if the buoyant plume needs a refractive index match, as will be described in §2.3.3, the Schlieren method will completely malfunction because there is no refractive index field anymore.

Laser induced fluorescence (LIF) is one of the most powerful and commonly used techniques to measure the concentration of tracer species in a fluid flow (Chrzan, 2012; Mayinger et al., 2001). Adding certain types of fluorescence to the flow allows observation of the concentration of the fluorescence, provided a laser is applied to excite the fluorescence. LIF is a non-intrusive measurement of the fluorescence concentration and gives quantitative information about the concentration. However, as will be discussed in §2.4.2, this technique requires careful calibration and correction procedure.

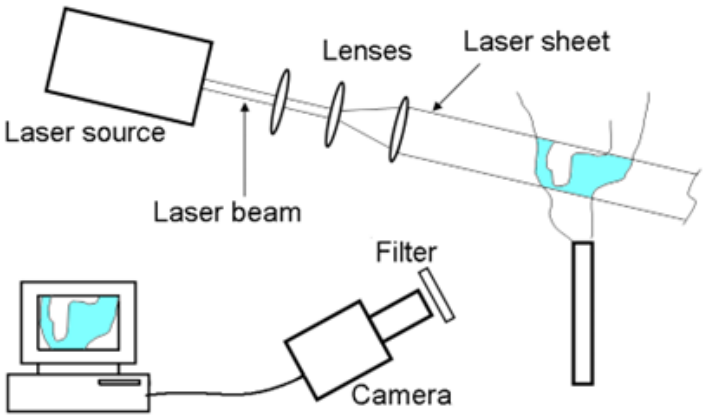

Figure 2.4: Sketch of LIF.

2.2 Plume Creation

As mentioned earlier, the plume is created by releasing/injecting fluids with different densities into a tank. The creation of such a plume, however, needs more discussion on the realization in a lab setup. This section first explains how the setup was designed (§2.2.1) and then describes the apparatus of the experimental setup in §2.2.2.

2.2.1 Preliminary Design

There are two key considerations to be addressed in the plume creation. The first question is, what is the geometry within which the plume will be released, held, and measured? The second question is how to obtain the density difference. These questions shall be discussed as follows.

The Geometry of the Setup

The plume is to be released from a round outlet, creating an axisymmetric plume. Furthermore, a cuboid tank will be used to hold the plume for its evolution, and Fig. 2.5 is the cross-section view of the setup. Even though a cylindrical tank seems to be a better choice when considering the system's symmetry (the round plume outlet matches the round shape tank), a cuboid tank was chosen. The reason is that the water tank's cylindrical shape may pose a problem on the optical measurement due to refraction, and as a result, the option of using a cylinder tank is discarded.

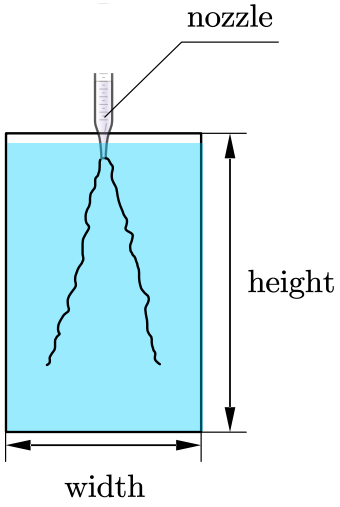

Figure 2.5: Preliminary design of the experiment setup. A cuboid tank is used as the reservoir of the less dense fluid, and the heavy fluid is to be released from the top using a nozzle.

The vertical dimension of the tank should be much larger than the dimension of the plume nozzle so that the plume becomes self-similar. It was reported by Ezzamel et al. (2015) that after a distance of 10 times the nozzle diameter, the second-order velocity statics becomes self-similar. As a result, the outlet nozzle is chosen to be 3 mm, whereas the height of the cuboid tank is 495 mm, large enough for the plume to develop.

Similarly, the horizontal dimension of the tank should also be chosen correctly to minimize the effect of the plume-tank interaction. If the tank's width is too small, the plume might interact with the tank wall. Furthermore, the choice of width is also constrained by the aspect ratio (width to height) as mentioned by Barnett (1992), where

the aspect ratio value between 1 and 5.8 was recommended. As a result, the width of the tank was decided to be 293 mm.

Up to this point, the general geometric parameters of the experiment setup are specified. In the next experiment design stage, the method used to generate buoyancy will be discussed.

Buoyancy Source: Different Density Solutions

The density difference is achieved by adding sodium sulfate to water, creating a heavier solution than fresh water. Although density difference may also be obtained by adjusting the species concentration or changing the temperature, using temperature difference to create the density difference is not favorable for several reasons.

Had a temperature difference been used to create the plume, there would be two difficulties. First, there would be difficulties in creating a uniform/flat temperature profile at the inlet. In classical plume theory, the plume is assumed to be a point source (Morton et al., 1956), and a point source clearly has no buoyancy profile. Since it was chosen to create a plume from a circular nozzle inlet, it is desirable to have a uniform buoyancy profile at the inlet. However, obtaining a uniform temperature profile at the inlet can be quite a challenge due to heat transfer. Let's say cold water is to be used as the source of the plume. Before being injected into the tank, the cold water has to pass a transporting pipe and the nozzle, and a certain temperature profile will develop because of the temperature difference between the pipe and the running cold water (see Fig. 2.6). It would probably be difficult to flatten the temperature profile.

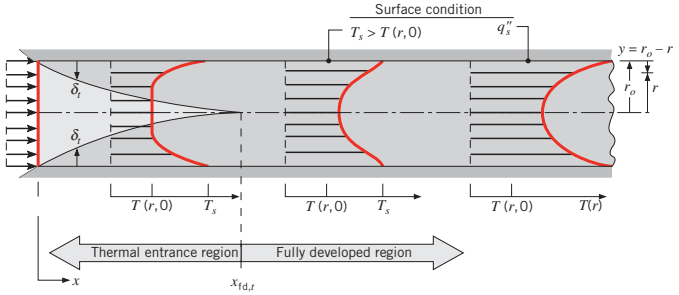

Figure 2.6: Typical temperature profiles of a pipe flow (Bergman et al., 2018).

Second, there would be difficulties in monitoring the source temperature. To know the inlet buoyancy condition requires measurement of inlet temperature. Even if the cold water is generated and kept in a constant temperature water bath/reservoir, whose temperature is a known value, chances are that the temperature at the nozzle outlet will not be the same due to heat transfer in the transportation pipe. Since the inlet nozzle diameter is so small (3 mm), it could be difficult to monitor the source temperature

without affecting the flow (especially when considering the sizes of a typical temperature probe).

Contrary to the above difficulties, using a denser fluid (with a higher concentration of chemical substance) would be a good choice. First, there is no difficulty in obtaining a uniform buoyancy profile at the inlet, as there is no mass transfer along the transportation pipe. Second, there is no need to measure the inlet concentration/buoyancy because the desired concentration will be specified as a priori constant, where the amount of sodium sulfate will be calculated and the concentration will be adjusted.

The density difference can be adjusted by varying the concentration of sodium sulfate. By looking up concentrative property table provided by Haynes (2016), desired density values can be obtained. For example, assuming the freshwater density is 998 kg/m^3, then the density of 6 wt% sodium sulfate solution will be 1052.6 kg/m^3.

Experimental Parameters

The experimental conditions can be specified by two parameters, including the source Reynolds number Re_0 and the source Richardson number Γ_0 (Li et al., 2019). These parameters can be calculated in the following way. Recall that earlier in this section, it was decided the nozzle diameter would be $d = 3$ mm. The source Reynolds number will then be given by

$$Re_0 = \frac{\varrho_0 u_0 d}{\mu_0}, \tag{2.20}$$

where the subscript "0" means values evaluated at the source. The source Richardson number Γ_0 can be found by plugging the source volume flux $Q_0 = \frac{\pi}{4} d^2 u_0$, the scource momentum flux $M_0 = \frac{\pi}{4} d^2 u_0^2$, and the source buoyancy flux $F_0 = g\frac{\varrho_0 - \varrho_e}{\varrho_e} Q_0$ into the definition of the Richardson number given in Eq. 1.7.

With the mass fraction of the sodium sulfate in the dense fluid to be 6%, one can obtain different forms of plumes by varying changing the inlet velocity, and the experimental parameters are summarized in table 2.1 (experiment number 1 to 10). Experiments 11 to 20 are measurements with refractive index matching (RIM), and experimental parameters in these measurements are the same with experiments 1 to 10, except there is no refractive index field. As a result, the mass fraction of sodium sulfate needs to be adjusted accordingly to eliminate the refractive index field, and this will be explained in §2.3.3.

Table 2.1: Experimental Parameters.

Exp. No.	u_0 (cm/s)	ρ_0 (g/ml)	ρ_e (kg/m^3)	Q_0 (ml/s)	Re_0	Γ_0
1	2.45	1053.21	997.44	0.17	64.37	13.80
2	3.41	1053.21	997.44	0.24	89.67	7.11
3	4.14	1053.21	997.44	0.29	108.65	4.84
4	5.10	1053.21	997.44	0.36	133.95	3.19
5	6.06	1053.21	997.44	0.43	159.26	2.25
6	7.03	1053.21	997.44	0.50	184.56	1.68
7	7.99	1053.21	997.44	0.56	209.86	1.30
8	8.95	1053.21	997.44	0.63	235.17	1.03
9	9.91	1053.21	997.44	0.70	260.47	0.84
10	10.88	1053.21	997.44	0.77	285.77	0.70
11	2.45	1072.45	1020.45	0.17	63.55	12.58
12	3.41	1072.45	1020.45	0.24	88.53	6.48
13	4.14	1072.45	1020.45	0.29	107.26	4.41
14	5.10	1072.45	1020.89	0.36	132.24	2.88
15	6.06	1072.45	1020.89	0.43	157.22	2.04
16	7.03	1072.45	1020.89	0.50	182.20	1.52
17	7.99	1072.45	1020.89	0.56	207.18	1.17
18	8.95	1072.45	1020.13	0.63	232.16	0.95
19	9.91	1072.45	1020.13	0.70	257.14	0.77
20	10.88	1072.45	1019.66	0.77	282.12	0.65

2.2.2 Plume Delivery Instrumentation

The plume creation system contains several parts, namely the plume injection nozzle, the pumping system, and the piping system. The nozzle will be introduced first.

The Nozzle

The outflow from the nozzle should be as uniform as possible, and a pipette with an outlet diameter of 3 mm was used to create the plume. Similar to getting a flat buoyancy profile, it is desirable to have a uniform velocity profile at the outlet of the nozzle. In many experiments, a contraction duct is used to reduce the fluctuating velocity component and accelerate the flow, resulting in a uniform flow (Abdelhamed et al., 2015). Our experiment uses a pipette as the nozzle, given its streamlined contraction design, to flatten the velocity profile. As shown in the following figure, the pipette has an outlet diameter of 3mm and an inlet diameter of 10 mm.

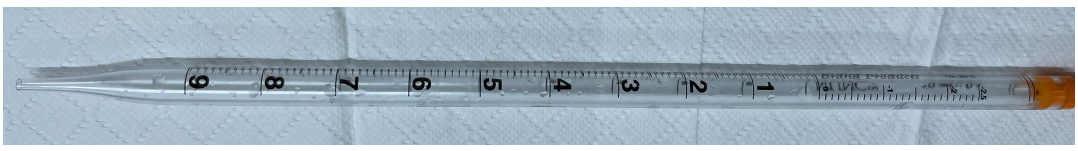

Figure 2.7: A pipette was used as the nozzle to inject fluids with higher density. Notice that the outlet of the pipette has a contract, which can be used to flatten the velocity profile.

The Pumping

The pumping system uses one pump that drives the liquid into the nozzle. There are two approaches to driving the fluid, and the first method is using a pump and the other is using gravity. It is possible to use gravity as the driving force, where the high-density fluid is placed in a tank at a higher altitude, and the fluid will flow downward naturally under gravity. However, based on the lab's logistics, controlling the flow rate is difficult in this scenario because a valve and an accurate flowmeter will be required. In contrast, if a pump is to be used as the driving force, one can adjust the flow rate by simply controlling the pump. Therefore, a pump is decided to be the driving force.

There are many different types of pumps available (Nesbitt, 2006a), and when choosing the pump type, one needs to consider the requirements of the experiment. As revealed by the experimental parameters in table 2.1, the volume flow rate is quite low, and it is required to control the flow rate. Therefore, a low-speed pump with a flow rate regulating ability is preferable.

Among all the pump types, positive displacement pumps offer a good ability to achieve a low flow rate while maintaining the possibility to adjust the volume flow rate. This is because the working principle of positive displacement pumps is to suck fluid by continuously compressing and discharging the fluid at any given speed (Nesbitt, 2006a).

In the fluid mechanics lab at Delft University of Technology, there are two types of positive displacement pumps available: syringe infusion pumps and peristaltic pumps. A syringe pump typically consists of a syringe holder and a stepper motor. When working, the syringe pump's stepper motor moves and pushes the plunger flange of the syringe while the syringe is held firmly by the syringe holder. And by controlling the speed of the motor, the syringe pump can deliver the amounts of fluid at a desired rate. A peristaltic pump often has a rotating roller and a flexible/elastic tube. The peristaltic pump transport fluid by mechanically squeezing the flexible tube using the rotating roller. The flow rate can be adjusted by changing the speed at which the roller rotates.

(a) The syringe pump **(b)** The peristaltic pump.

Figure 2.8: Available pumps in the lab.

The peristaltic pump was decided as the pump in the experiment. There are two main limitations associated with the syringe pump in the lab. First, the syringe pump has a limited capacity. Notice that the largest size of the syringe that the available syringe pump can hold is 50 ml. Given that the flow rate decided in table 2.1 is on the order of ml/s, the pump will run out of liquid after about 1 minute, which restricts the measurement of the experiment. Second, the syringe pump has a limited flow rate. It was tested that the existing pump has a maximum flow rate of 300 ml per hour, and this flow rate was not even close to the desired value of ml per second. The two major limitations ruled out the possibility of using the existing syringe pump in the lab, and the peristaltic pump was chosen as the pumping unit.

Yet, the existing peristaltic pump (Watson Marlow 505Du) poses other challenges in the experiment. One of the major challenges is the fluctuating flow rate caused by the peristaltic pump (Klespitz & Kovács, 2014; Nesbitt, 2006b). Nonetheless, the drawbacks of pulsation can be mitigated. There are several methods to mitigate the effects of fluctuations, including adding more rollers to the pump, purging out air bubbles, and modifying the pipework (Nesbitt, 2006b). One should consider combining as many the above methods as possible when designing the pumping system, and in the following discussion about the pipework, it will be shown that our design can combine all the techniques together, mitigating the pulsation to a large extent.

The Piping

The piping system contains a series of tubing and containers that transport the fluid, and two designs of the piping system have been tested. The first method is to transport the

sodium sulfate solution directly, and the second is to transport the solution indirectly.

The direct method involves sucking the solution directly from a reservoir and transporting it to the nozzle. However, since the pipes were originally empty and full of air before the experiment startup, it was tested that the method usually traps a lot of air bubbles in the tubing between the rollers during the experiment, *causing the pulsation phenomenon to deteriorate*. Hence, this method is abandoned.

The current design aims to resolve the air-bubble-trapping problem by pumping air directly and using the air to move the sodium solution indirectly. This design was motivated by previous practices, which successfully reduced the fluctuations in flow by taking advantage of air compressibility (Jiao et al., 2019; Kang et al., 2014). A gas-washing bottle from the chemical lab (Fig. 2.9) was added to the piping system, but it was used in a reverse direction: use the air to purge out the sodium sulfate solution. The trick of adding a gas-washing bottle solves two problems simultaneously. First, by separating the air and the solution, the method solves the air-bubble-trapping problem because the peristaltic pump now works solely for pumping air. Second, the method adds a pulsation damper by introducing a thick layer of air before pumping the solution; moreover, it was demonstrated that *when the gas-washing bottle is half-filled with air, the pulsation could be almost damped out.*

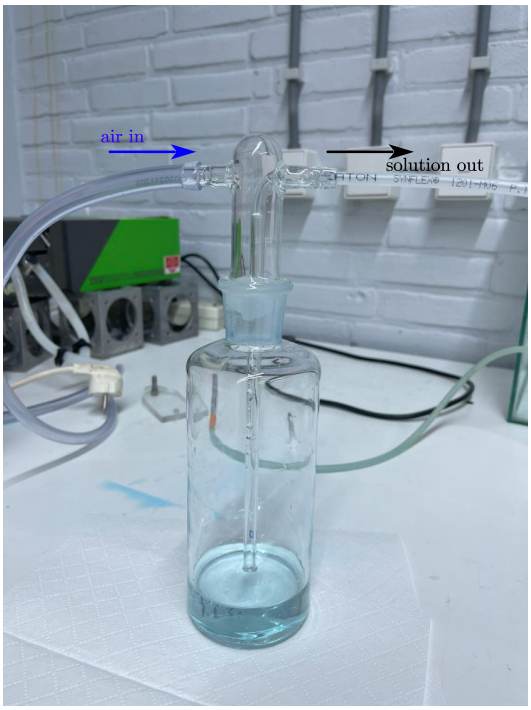

Figure 2.9: A gas washing bottle was used in the reverse direction as the damper to limit flow fluctuations. The left end is connected to the peristaltic pump, and air will be pumped into the gas washing bottle. The high-density solution will be purged out from the right end of the gas washing bottle.

Quick Summary: The Plume Delivery Instrumentation

The plume delivery system consists of all the components mentioned above and is mounted on a rigid aluminum support (Fig. 2.10). The following sketch shows how all the parts for plume delivery are placed and arranged, and the corresponding setup photo is also shown. It should be noted that the aluminum structure provides extra space for mounting optics, which, as will be shown in §2.3.2, allows the laser sheet to be projected through the lateral wall of the tank.

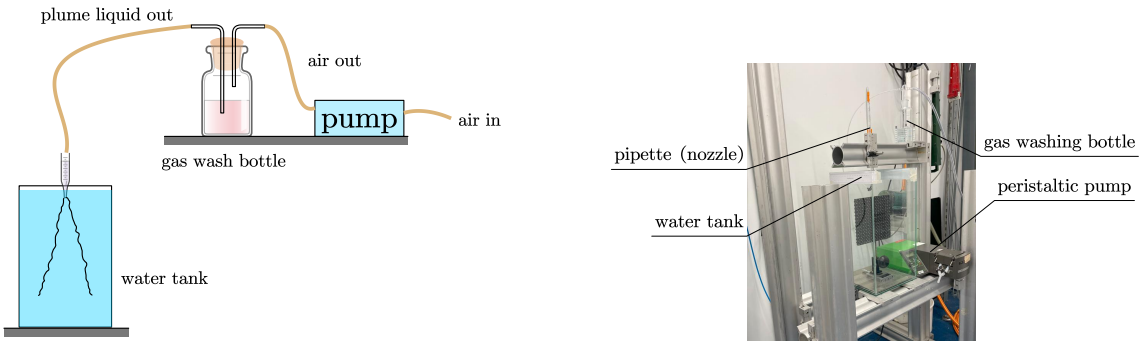

(a) The plume delivery system sketch.

(b) The plume delivery system lab setup.

Figure 2.10: The plume delivery system. (a) The sketch of the plume delivery system, and (b) the setup photo in the lab, and the whole setup is placed on a rigid aluminum frame.

2.3 PIV Setup

This section discusses the velocity measurement technique that was chosen in §2.1.2, the particle image velocimetry (PIV). First, a brief introduction to the PIV measurement system will be explained (§2.3.1). Then, experiment apparatuses in our experiment will be outlined in §2.3.2, followed by a discussion of refractive index matching (§2.3.3).

2.3.1 Introduction to PIV

The working principle mentioned previously in §2.1.2 specified that PIV works on capturing the displacement of small particles carried by the flow during a very short time interval. The working principle implies that one PIV system consists of at least four steps. The first step is flow seeding, which means some tracer particles must be added to the flow. The second step is flow illumination, where the flow field must be illuminated by proper light in order to make particles visible. The third step is flow imaging, in which the images of seeded flow are recorded by a camera. The last step involves processing images and extracting velocity information from images.

Flow Seeding

Since most fluids, including the liquid used in our water tank experiment, are transparent, visualizing the flow and calculating velocity information requires seeding the fluid with some microparticles. The microparticles should be expected to have good mechanical properties and optical properties.

The microparticles must have good mechanical properties such that they can follow the flow faithfully. The dynamical analysis of small tracer particles used in typical PIV systems shows that the only term that dominates the dynamics of one particle is the quasi-steady viscous term (Stokes drag), and the response time of the particle is

$$\tau_p = d_p^2 \frac{\varrho_p}{18\mu}.$$

The formula indicates that the smaller the particle size d_p, the faster the particle can respond to the flow condition changes (such as changes in flow direction or velocity magnitude). In other words, small particles are preferred so that the seeding particles can follow the flow faithfully.

Yet, using small particles compromises optical properties. For spherical particles with a diameter larger than the laser wavelength, Mie's theory is applicable, and the theory dictates that the light scattering ability depends on the particle diameter, laser light wavelength, and refractive index of the particle. Since both the laser wavelength and the refractive index cannot be changed because they are inherent properties of the laser and the particle, the common guideline for PIV is to choose the largest particles, provided that the particle can still follow the flow.

Illumination

Particles are only visible when the laser is on. If the laser is off, the camera will not capture any visible particles because the experiment is performed in a dark room, and the PIV image is black without any light source. On the other hand, when the laser is on, it illuminates the particles, and the camera records the images (Fig. 2.11).

Because particles will be visible when the laser is on, it is desirable to keep the illumination time (pulse duration δt) as small as possible. If the pulse duration δt is very long, the particles stay visible while they keep moving with the flow, and this will result in streaks in the image, causing the image quality to deteriorate (Fig. 2.11). The laser used in the present study has a pulse duration of around 150 nanoseconds, which is reasonably small for the PIV measurement (Photonics Industries, 2023).

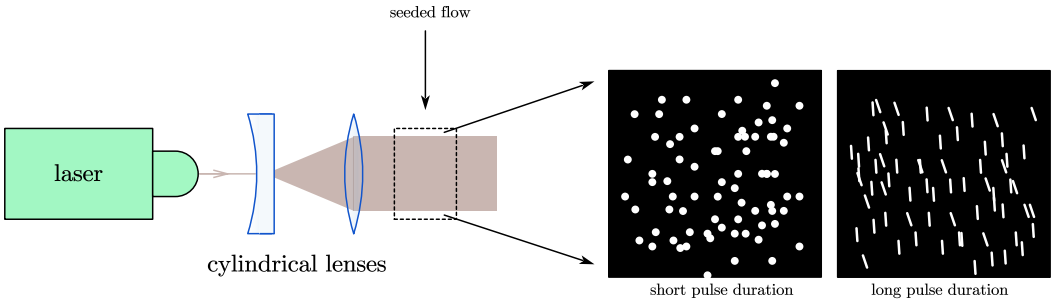

Figure 2.11: Sketch of PIV measurement. When the laser is on, the laser beam is expanded to a laser sheet and illustrates the whole flow field. When the seeded flow passes the measurement window, the particles in the flow begin to scatter laser light and show up as dots on the image, provided that the pulse duration is short. However, if the pulse duration is too long, particles will appear as streaks because they constantly scatter light while moving.

If particles are imaged as dots for every pulse, it is possible to analyze two consecutive images of the flow field that have been illuminated *twice* to obtain the instantaneous velocity field. In other words, one measurement by PIV requires *two* laser pulses. The time between the two pulses is called separation time Δt.

The proper choice of Δt is important for image processing at later stages. The choice of Δt must ensure that most particles are captured in the same window during both exposures so that there are enough particle pairs contribute to the cross-correlation. In practice, one can follow the *one-quarter rule* (Raffel et al., 2018). The one-quarter rule asserts that during the separation time Δt, the displacement of particles should not exceed a quarter of the interrogation window, namely

$$\text{displacement} = Mu\Delta t < \frac{1}{4} \text{ interrogation window}, \tag{2.21}$$

where M is the magnification factor, u is the flow velocity, and the interrogation window size can be calculated from the (known) pixel pitch.

Imaging

The image of particles in the flow field must go through lenses before being received by the camera sensor, and the schematic is shown in Fig. 2.12. The imaging lens system has several attributes, such as the focal length of the lens f, aperture number (f-stop) $f_\#$, magnification factor M, object distance d_o, and image distance d_i.

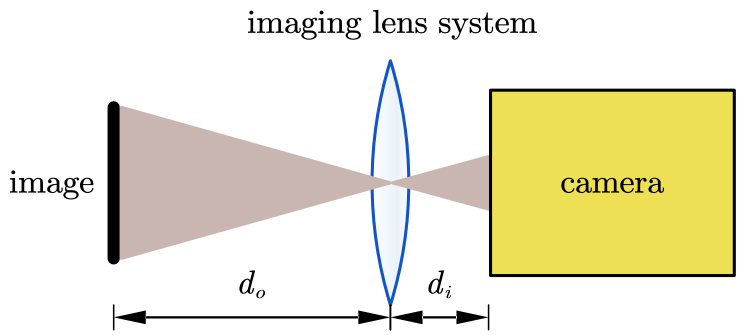

Figure 2.12: Ray path of the imaging process.

Apparently, the position where the camera can be placed is restricted by the imaging lens system. With the thin lens formula, the image distance d_i and object distance d_o can be related by the focal length f:

$$\begin{cases} \frac{1}{f} = \frac{1}{d_i} + \frac{1}{d_o}, \\ M = \frac{d_i}{d_o}, \end{cases} \tag{2.22}$$

where the magnification factor M can also be determined from the ratio of camera sensor size to measurement window size.

Furthermore, the aperture number $f_\#$ is also restricted by physical constraints. On the one hand, there is a physical constraint—the focal depth should be thicker than the laser sheet thickness—that puts a lower limit on $f_\#$. The reason is that if the focal depth is thinner than the laser sheet thickness, particles will stay out of focus, causing blurs in images. The focal depth δz can be calculated as

$$\delta z = 4.88 \lambda f_\#^2 \left(\frac{M+1}{M} \right)^2, \tag{2.23}$$

where λ is the wavelength of the laser. Since the typical laser sheet thickness in an experiment is a constant, the above equation puts a lower limit on the choice of $f_\#$.

On the other hand, there is an upper limit on the aperture number $f_\#$ because of the particle image size (Raffel et al., 2018). If the particles' size on the image is too small (smaller than 1 pixel), *peak locking* or *pixel locking* phenomenon can occur, which means that the accurate position of particles cannot be detected by the camera sensor. If the particles' size on the image is too big (bigger than 3 pixels), individual particles appearing on the image may begin to overlap, which compromises the spatial resolution of the measurement. As a rule of thumb, it is desirable to have the particle image size around 2 pixels. The particle image size can be calculated as the Euclidean sum of

diffraction particle size and effective particle size

$$d_{p,\mathrm{im}} = \sqrt{(Md_p)^2 + (d_{\mathrm{diff}})^2} \approx d_{\mathrm{diff}} = 2.44\lambda(1+M)f_{\#}, \tag{2.24}$$

where $d_{p,\mathrm{im}}$ is the particle image size, d_p is the actual particle size, and $d_{\mathrm{diff}} = 2.44\lambda(1+M)f_{\#}$ is the *Airy disc* diameter caused by diffraction effects. It should be noted that d_{diff} is the dominant term in general. It is evident that Eq. 2.24 puts an upper limit on the choice of $f_{\#}$ because it is required that $2 < d_{p,\mathrm{im}} < 3$ px.

Image-Processing

Image-processing is a series of operations in order to extract displacement information from image pairs. In general, data processing consists of four steps. In the first step, the image has to be partitioned into a number of cells (interrogation window) depending on the specified interrogation window size. It is tempting to choose a small interrogation window as this would increase the resolution of the measurement. However, a small interrogation window makes it difficult to figure out displacement information because most particles may have left the interrogation window, and PIV may return a misleading displacement result.

In the second step, cross-correlation analysis is applied to each cell. The cross-correlation analysis will give the displacement value of each cell by finding the peak or maximum value. And later in the third step, a correlation-peak interpolation will usually be used to provide more accurate information about the displacement.

In the last step, the particle image displacement value is converted to velocity in the flow field. Because the separation time between two images is known, and the velocity of an interrogation window is readily available by dividing the displacement by the separation time. Eventually, the velocity on the image has to be rescaled to the actual velocity in the flow field.

2.3.2 PIV Instrumentation

Based on the working principles of PIV measurement, instruments used in our experiments will be introduced. Major components include the PIV camera, the laser system, the optics, and the PC control.

The PIV Camera

LaVision's Imager sCMOS CLHS camera was used as the PIV camera. According to the manufacturer, the camera has 2560×2160 pixels with a pixel pitch of 6.5μm, and the maximum frame rate is 50 fps (LaVision, 2023).

The camera should be equipped with a suitable lens per the requirements outlined in previous §2.3.1. The magnification factor, for example, can be determined by the field

of view (FOV) size and the camera sensor size. Other parameters, such as $f_{\#}$, should be calculted by Eq. 2.22 and 2.23. After a visualization experiment (which will be explained in §3.1), it is possible to find the desired FOV and choose the correct lens for the camera: $f = 50$ mm, $f_{\#} = 5.6$.

Moreover, a bandpass filter should be applied to the PIV camera. Since the PIV particles scatter laser light without changing the wavelength, the filter should allow wavelengths around the laser wavelength to pass while blocking other wavelengths, such as the fluorescence from the LIF measurement, which is around 550 nm. Specifically, the Edmund OD 6 Fluorescence Filter has been used for the PIV camera. This filter allows wavelengths between 510 and 540 nm to pass and effectively blocks other wavelengths (Edmund, 2023).

The Laser

One Nd:YLF (Neodymium-doped Yttrium Lithium Fluoride) laser was used for both PIV and LIF measurements. The dual head Nd:YLF laser, made by Photonics Industries, can lase at a wavelength of 527 nm. Furthermore, the laser has relatively high pulse-to-pulse stability, with variation smaller than 0.5% rms (Photonics Industries, 2023).

The laser was placed at a height similar to the water tank, simplifying the ray path. The laser head is mounted on rigid aluminum bars and is lifted to a similar height as the water tank, and the space below the laser head are the temperature and the laser control units for the laser head. Moreover, because the laser beam will be projected at a similar height as the measurement region, this reduces mirrors and simplifies the optical setup.

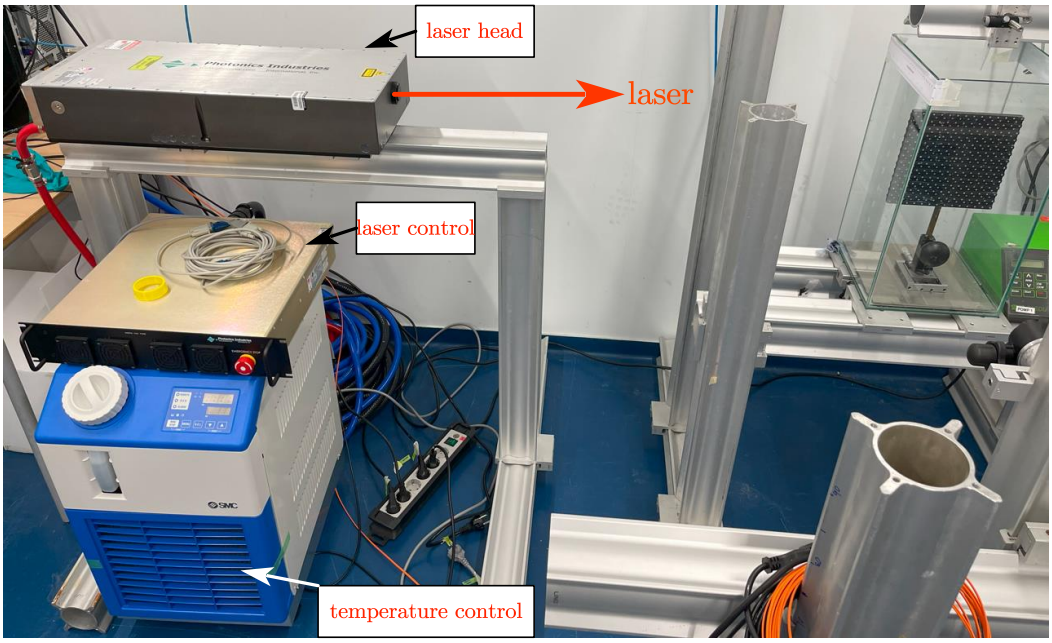

Figure 2.13: The Nd:YLF laser system.

The required laser pulse separation time Δt can be estimated after a plume visualization, which will be explained in the §3.1. Once the plume is visualized, it is possible to estimate the centerline velocity of the plume, and thus calculate the separation time using Eq. 2.21. Ultimately, the separation time should be optimized to meet the one-quarter rule of PIV measurements, and in our experiments, Δt is a variable under different inlet conditions.

Lastly, a filter should be applied to the PIV camera to block light with a higher wavelength. It will be explained in §2.4.3 that the LIF signal will have a higher wavelength, and a filter must be applied to block the LIF signal to prevent the LIF signal from affecting the PIV measurement.

The Optics

Two mirrors were used to change the position of the laser sheet. The laser beam coming out from the laser head is not aligned with the vertical position of the measurement region, and thus the laser beam cannot be expanded directly. Instead, the laser beam should be collimated at the desired vertical position (z-direction) before expanding, and this is done by changing the vertical *distance* between the two mirrors, marked as "mirror 1" and "mirror 2" in Fig. 2.14. Similarly, in the x-direction, the laser beam may not be aligned with the desired laser sheet position, and this problem may be solved by varying the relative *angle* between the two mirrors.

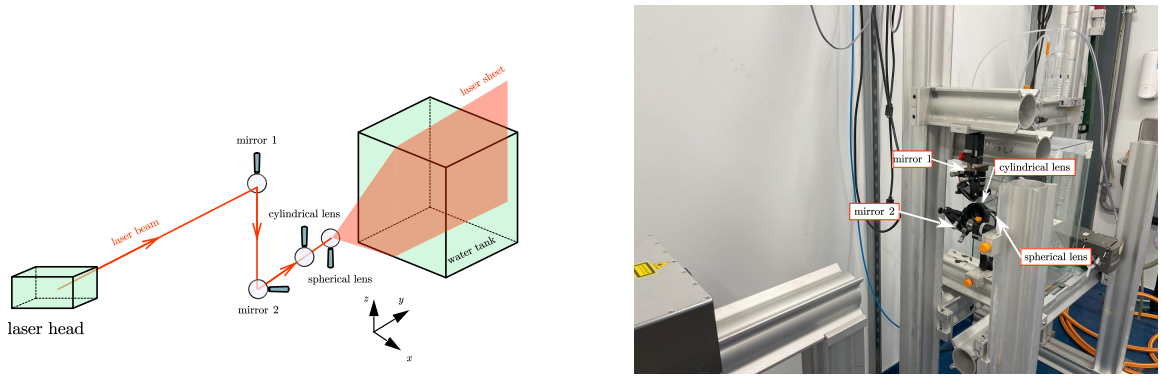

(a) A sketch. **(b)** The lab configuration.

Figure 2.14: The optical setup.

A combination of a cylindrical lens and a spherical lens was used to reshape/expand the laser beam into a laser sheet. The cylindrical lens serves to expand the beam vertically while the spherical lens converges the expanded laser beam. As a result, the combination not only elongates the beam vertically (in the z-direction) but also compresses the laser beam horizontally (in the x-direction), forming a laser sheet with a contracting cross-section. The thinnest cross-section of the laser beam is termed the *waist*.

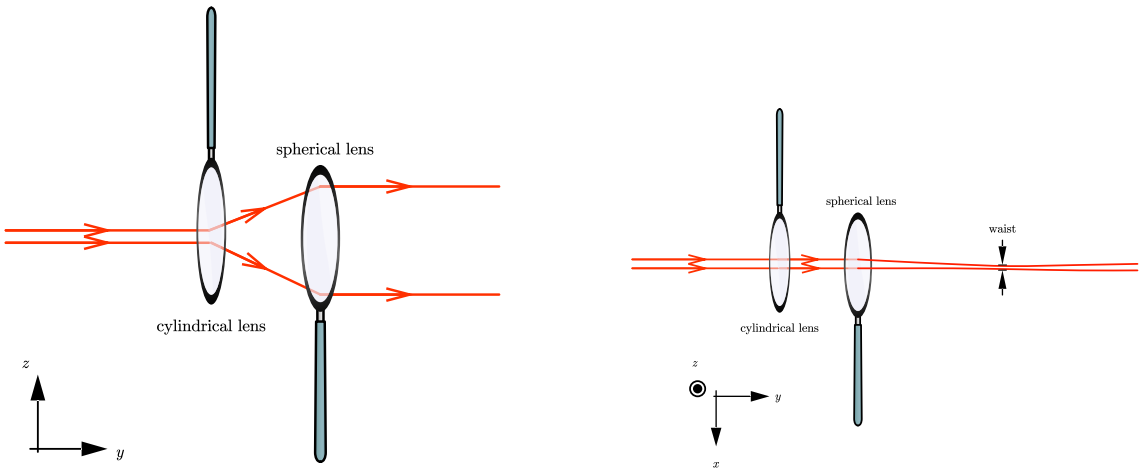

(a) Front view of laser sheet. **(b)** Top view of laser sheet.

Figure 2.15: The laser sheet formation illustration.

It is desirable to position the measurement region around the waist area to optimize the image quality. The position of the waist can be changed by choosing a spherical lens with a different focal length because the spherical lens converges the laser sheet at a distance equal to its focal length.

Furthermore, as a rule of thumb, the thickness of the waist should be roughly the same as the interrogation window size. Since the interrogation window is usually 32 by

32 pixels, and the pixel pitch can be known from the manufacturer's specification, one can determine that the interrogation window size is around 1.6 mm. Thus, the waist thickness, a function of the spherical lens' focal length and laser properties, should be about 2 mm.

2.3.3 Refractive Index Matching

A known issue with PIV measurement is the existence of a refractive index field in the flow (Mishra & Philip, 2021). In §2.3.1, it was discussed that high-quality images are the key to the success of PIV measurement, which implies that particles should appear as dots on images. However, if a refractive index field presents in the flow, some particles may become blurred due to variations in ray paths. Elsinga et al. (2005) identified two types of errors associated with the refractive index field, namely the position error and the velocity error, and according to their description, the particles that would have been circular dots started to stretch, forming blurry regions.

The particle-blur effect was observed in our experiment, as shown in Fig. 2.16. The reason for such a blur should not be surprising; after all, the plume is a sodium sulfate solution with high density, and the refractive index for sodium sulfate solution cannot be the same as fresh water.

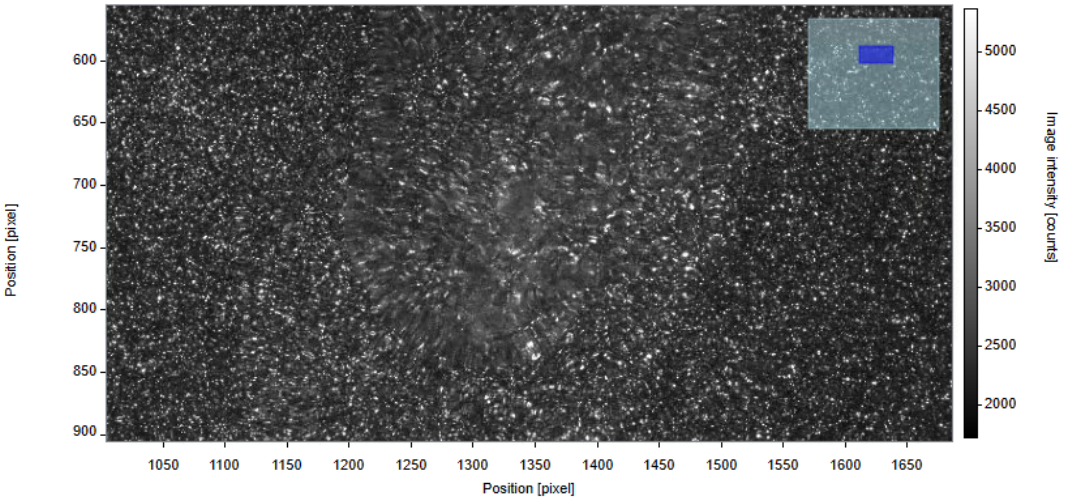

Figure 2.16: A PIV image in the experiment. In the center of the image, large lumps of blurred particles can be observed.

The particle-blur problem may be solved by refractive index matching (RIM). RIM is a technique to ensure that the refractive index field is the same throughout the entire flow regime by utilizing distinctive properties of different chemicals. Ethanol, for example, when added to fresh water, can increase the refractive index while decreasing the density. On the other hand, the addition of sodium sulfate increases both the refractive index and

the density when added to fresh water. In a nutshell, when choosing proper chemicals, RIM allows a uniform refractive index field while retaining density difference.

Urea was chosen as the counterpart of sodium sulfate in an attempt to perform RIM. There are many promising chemicals that can be used as RIM, and researchers in the past used ethynol or sodium nitrate to perform RIM (Mishra & Philip, 2021). Yet the two choices were discarded due to lab safety considerations in terms of lab regulations. Haynes (2016) provides a comprehensive list of chemicals and their aqueous solutions' concentrative properties, and urea was chosen for RIM because it is relatively safe and cheap. With data from Haynes (2016), the properties of both urea and sodium sulfate solution can be plotted in Fig. 2.17. By changing the mass concentration of glycerol and sodium sulfate, one can obtain the same refractive index while keeping the density difference.

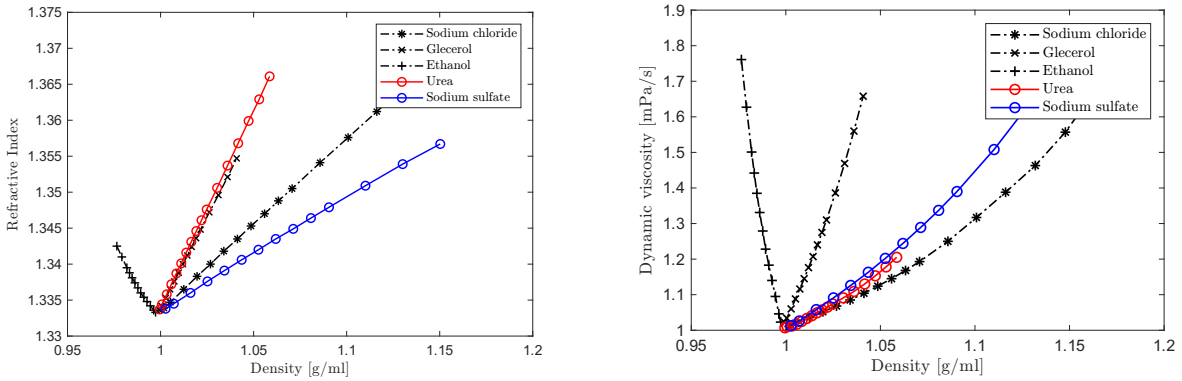

(a) **(b)**

Figure 2.17: The physical properties of promising RIM materials. (a) the refractive index as a function of concentration (density), and the combination of urea and sodium sulfate is good for RIM because the difference in curves' slope is large. On the contrary, the difference in curves' slope for sodium chloride and sodium sulfate is relatively small, and as a result, a certain density difference cannot be achieved without using a high concentration of solute. (b) the dynamic viscosity as a function of concentration (density), and the chosen combination of urea and sodium sulfate shows a similar viscosity under various concentrations.

The above data from Haynes (2016) was measured in mass fractions (wt%), which greatly simplifies the solution-preparation process if validated. Every data point in the above figure has a different mass fractions; in other words, one can easily prepare a solution with desired density (and refractive index) by simply changing the mass fractions. Changing the mass fractions requires only mass measurement, and volume measurement is unnecessary, which is a great advantage when considering the volume change when mixing. The mass concentration can be calculated as

$$\text{wt}\% = \frac{m_{\text{solute}}}{m_{\text{solute}} + m_{\text{solvent}}} \times 100\%,$$

and the equation can be solved when any two of the following variables are known: mass

of the solute m_{solute}, mass concentration of the solute C_{solute}, mass of the solvent m_{solvent}, or mass of the solution $(m_{\text{solute}} + m_{\text{solvent}})$.

Fig. 2.17 can be used as a reference when preparing solutions *only if* the validity is checked. Due to differences in water quality or temperature, the data provided by Haynes (2016), namely Fig. 2.17, could differ from our experiment; as a result, validation of data in Fig. 2.17 was carried out. The validation procedure involves comparing the predicted density value of a sodium sulfate solution with the actual value obtained through laboratory measurement. A sample sodium sulfate solution with mass fraction wt% = 6.02 was prepared, and the density predicted by Fig. 2.17 is 1.053788 g/ml while the density measured by a precise density meter in the chemical lab is 1.053478 g/ml, implying that the error of using Fig. 2.17 should be within 0.03 %.

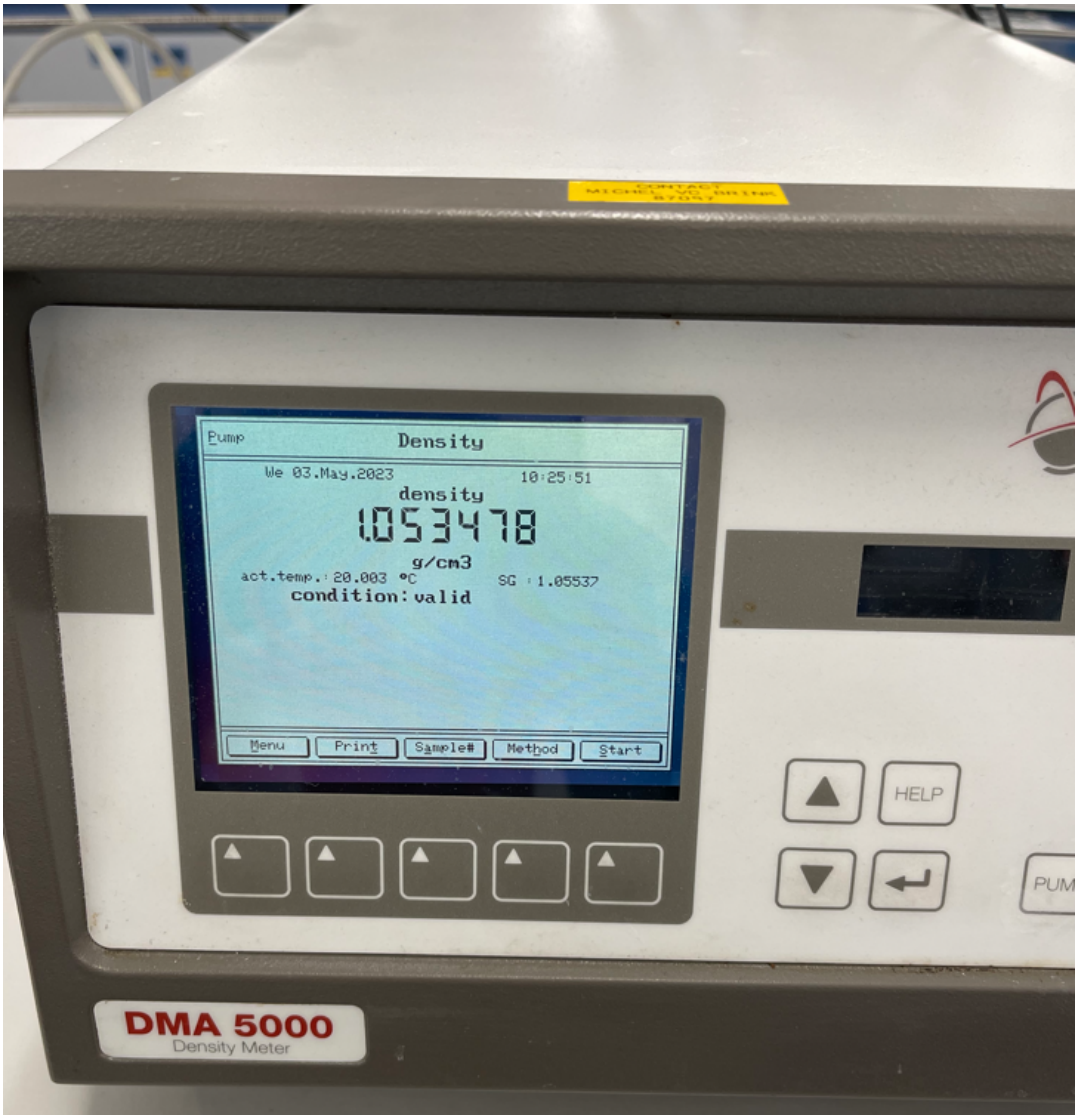

Figure 2.18: Density measurement result of the sample sodium sulfate solution.

In the current study (see table 2.1), all RIM measurements (experiment number 11

to 20) utilize a urea solution (wt% = 8.59%) and a sodium sulfate solution (wt% = 8.46%). Under the above two concentrations, the density difference is the same as non-RIM measurements (experiment number 1 to 10), where the tank fluid contains no urea (wt% = 0.00%) and the plume fluid has a sodium sulfate concentration wt% = 6.00%.

2.4 LIF Setup

This section discusses the concentration measurement technique that was chosen in §2.1.2, the laser induced fluorescence (LIF). First, we start with a brief introduction to the LIF theoretical in §2.4.1, explaining the fundamentals of fluorescence theory and why it is necessary to convert concentration value. Then, more detailed description about LIF data processing is outlined in §2.4.2. Finally, the experiment instruments will be introduced in §2.4.3.

2.4.1 Introduction to LIF

LIF measurement can be understood as a two-stage process and is based on the unique properties of natural fluorescent molecules. A fluorescent molecule is defined as a molecule that absorbs incident light at a specific wavelength and later emits light. In the first stage, the effect of incident light/laser is to excite a considerable number of fluorescent molecules from the lower energy level (ground state) to the higher energy level (excited state). Once molecules are promoted to a higher energy level, they may subsequently return to the ground level by emitting fluorescence at a certain wavelength in the second stage.

Naturally, based on the brief discussion of LIF principles, the LIF returns the concentration of fluorescent molecules from the intensity of the fluorescence signal. Yet, the conversion from signal intensity to concentration is accurate only if numerous factors that can lead to misleading intensity measurements are corrected, and this will be examined in the next subsection §2.4.2. In the current subsection, however, only the fundamental fluorescence theory and the conversion of different concentrations will be explained.

Fluorescence Theory Fundamentals

Mayinger et al. (2001) shows that the analysis of the energy level model yields the following relation between fluorescence FR and the concentration of the fluorescent dye C_f

$$FR = C_\mathrm{f} B_{12} I \left(\frac{A_{21}}{A_{21} + Q_{21}} \right) \left(\frac{1}{1 + I/I_\mathrm{sat}} \right),$$

where B_{12}, A_{21},and Q_{21} are constant, I is the local laser intensity used to excite the fluorescent dye, and I_{sat} is the saturation intensity of the dye. It is evident that the relation may be simplified as

$$FR \propto C_{\text{f}} \left(\frac{I}{1 + I/I_{\text{sat}}} \right). \tag{2.25}$$

This relation provides a way to calculate the concentration of the fluorescent dye based on the knowledge of local excitation laser intensity I and fluorescence FR.

The nonlinear Eq. 2.25 can be further simplified. Under the assumption that $I_{\text{sat}} \gg I$, Eq. 2.25 may be rewritten as

$$FR \propto C_{\text{f}} I, \tag{2.26}$$

and this equation is a simpler way to calculate the concentration of fluorescent dye. The assumption of $I_{\text{sat}} \gg I$ implies that the local laser intensity (used to excite the dye) is very small compared with the saturation intensity, and this assumption is generally valid in LIF (Mayinger et al., 2001). It should be noted, however, that not only a high excitation laser intensity causes non-linearity but also a high concentration of fluorescent dye. Crimaldi (2008) and Ferrier et al. (1993) showed that the linear Eq. 2.25 is not valid when the dye concentration is too high. Ferrier et al. (1993) concluded that for fluorescent dye Rhodamine 6G, a concentration of higher than 50 μg/l may cause non-linearity, and calibration of LIF should be done to ensure that the relation between FR and C_{f} is linear.

Nevertheless, using Eq. 2.26 is not as straightforward as it appears. On the one hand, the light intensity is not measured locally in the flow field and can vary spatially and temporally. Spatial variation, for instance, can be partly attributed to extinction/attenuation (light intensity decreases when traveling in a medium, such as water). On the other hand, measuring/interpreting the intensity of fluorescence may not be straightforward. To avoid a lengthy digression, detailed descriptions of how to correct these variations and how to interpret the fluorescence will be delayed to the next subsection §2.4.2. Now, another question about the conversion between different concentrations needs to be addressed.

Conversion between Dye Concentration and Salt Concentration

It should be reiterated that the concentration C_{f} measured by LIF in Eq. 2.26 is the concentration of the fluorescent dye, not the concentration of the sodium sulfate C. Because LIF determines the concentration based on the value of emitted light FR, and because sodium sulfate solution cannot be excited by a laser and cannot emit any light, the LIF only gives the concentration of the dye C_{f}.

However, one can infer the value of C from C_{f}. Despite the dye and sodium sulfate

being two different materials, the mass transfer process might be similar for them as long as the dimensionless number governing the process is alike. Similar to the Prandtl number in heat convection problems, the Schmidt number Sc, defined as the ratio of momentum diffusivity to mass diffusivity, governs the mass transfer problem in convection. Since Troy and Koseff (2005) reported that Sc of salt and that of Rhodamine 6G are on the same order of magnitude, the turbulent mixing for sodium sulfate and Rhodamine 6G is similar. In other words, even though LIF only measures the concentration of Rhodamine 6G, C_f, this value can be used to deduce the concentration value of sodium sulfate concentration C by using

$$C = \frac{\Delta C}{\Delta C_\mathrm{f}} \left[C_\mathrm{f} - C_{\mathrm{f}0} \right] + C_0, \tag{2.27}$$

where C_0 is the source concentration of the sodium sulfate, $C_{\mathrm{f}0}$ is the source concentration of the dye, ΔC is the maximum concentration difference presented in the experiment for the sodium sulfate, and ΔC_f is the maximum concentration difference presented in the experiment for the dye.

2.4.2 LIF Calibration

In the previous subsection §2.4.1, the fluorescence theory fundamentals were introduced, and it showed that LIF is based on the accurate measurement of fluorescence intensity. In reality, however, the fluorescence intensity can be affected by numerous factors, which may lead to erroneous results if left untreated. This subsection examines factors that influence the fluorescence intensity and explains the procedure to accurately evaluate concentration from the fluorescence intensity.

Incident Laser Intensity as a Function of Space

Numerous factors can change the laser intensity spatially (Ferrier et al., 1993). The first factor is attenuation. Attenuation is a phenomenon caused by the absorption or scattering of light as it travels through a medium. The intensity changes caused by attenuation can be describe by the Beer-Lambert law

$$\frac{dI}{I} = -\epsilon C_\mathrm{f} dr,$$

where ϵ is the absorption/extinction/attenuation coefficient, dr is the infinitesimal distance that light travels in the medium, and dI is the decreased amount of light intensity (or the absorbed amount of light intensity). Upon integration, the local laser intensity

I is a function of the spatial position:

$$I = I_0 \exp\left[-\epsilon \int C_{\mathrm{f}}(r)dr\right] = I_0 f\left(x, y\right), \tag{2.28}$$

where I_0 is the power of the incident laser beam. Any system satisfying $\epsilon \int_{r_0}^{r_1} C(r)dr \ll 1$ is termed as *optically thin*, meaning that the laser intensity change from $r = r_0$ to $r = r_1$ is negligible. It should also be noticed that the function f in the above expression is a neat collection that includes all the attenuation effects (because attenuation is a spatial variation only), and the trick of using a spatial function f will be used again later to include all the other fators described below.

The second factor is the light sheet distribution. The laser beam coming out from the laser heat must go through a series of optical lenses to become a laser sheet, yet the intensity of the laser sheet, in general, is not uniformly distributed. The following figure provides a sketch of such distribution, and according to Ferrier et al. (1993), the distribution of the laser sheet intensity may be approximated by a Gaussian function.

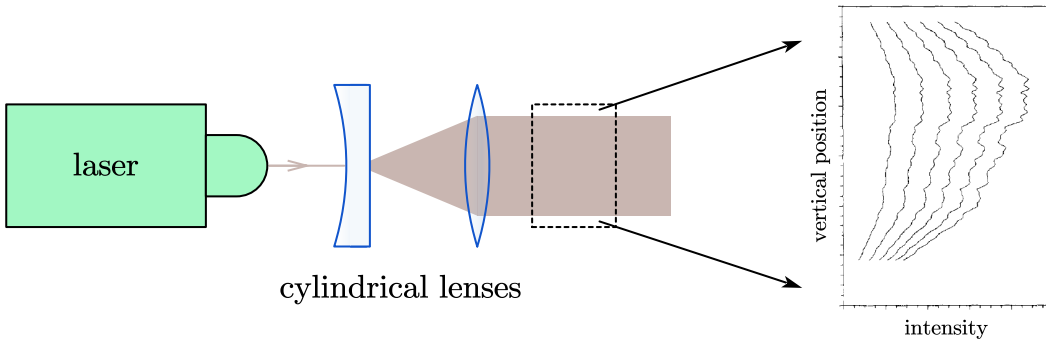

Figure 2.19: Sketch of the laser sheet intensity. Laser sheet is obtained by expanding a laser beam through optical lenses, and the intensity of a laser sheet is not uniform but is distributed in space. The shape of the distribution is Gaussian-like (Ferrier et al., 1993).

Apparently, the spatial distribution of laser sheet intensity can be corrected by multiplying the laser intensity by a spatial function, say $g\left(x, y\right)$. Without any loss of generality, the function $g\left(x, y\right)$ can be included by the aforementioned spatial function $f\left(x, y\right)$. Now, the correct function $f\left(x, y\right)$ in Eq. 2.28 takes into account two factors that cause laser intensity variations, namely the attenuation and the laser sheet distribution.

Outcoming Fluorescence Light as a Function of Space

As mentioned before, after the laser sheet illuminates the fluorescent molecules, fluorescent dye begins to fluoresce, and the fluorescence has to travel through the medium and be received by the LIF camera. Assuming that the emitted fluorescence will not be absorbed again, the fluorescence FR received by the camera may still be affected by

two factors.

The first factor that causes spatial variations in fluorescence FR is quantum efficiency. Only part of the absorbed laser intensity dI will be emitted as fluorescence FR. This process can be described by quantum efficiency ϕ, and by combining the Beer-Lambert law, the amount of fluorescence FR of a small volume is:

$$d\left(FR\right) = \phi\epsilon I C_{\mathrm{f}} dV,$$

where dV is the infinitesimal volume. It should be noted that quantum efficiency ϕ, defined as the ratio of emitted light to absorbed light, is another spatial function, namely $\phi = \phi\left(x, y\right)$. In other words, the quantum efficiency ϕ can be integrated into the correction function$f\left(x, y\right)$ in Eq. 2.28 without loss of generality. The above equation can be integrated over volume to give the total fluorescence FR.

The second factor is the actual amount of fluorescence received by the LIF camera. Not all emitted light FR is received by the camera, and only part of the light will be detected by the camera. Another coefficient, called the *omnidirectional coefficient*, can be used to relate the intensity received by the camera and the total fluorescence emitted (Crimaldi, 2008). Again, because the coefficient is a spatial function, which depends on the coordinates only, this coefficient can be incorporated by the correction function$f\left(x, y\right)$ in Eq. 2.28 without loss of generality.

Quick Summary: The Fluorescence Intensity as a Function of Space

Based on previous analyses of incident laser variation and fluorescent light variation, one can correct these variations altogether by the correction function$f\left(x, y\right)$. Since all the variations can be corrected by using proper coefficients that are a spatial function only, be it extinction coefficient ϵ or quantum efficiency ϕ, the intensity on the LIF image and actual dye concentration can be corrected by a single spatial function f as

$$I_{\mathrm{f}} = f\left(x, y\right) C_{\mathrm{f}}, \tag{2.29}$$

where I_{f} is the intensity perceived by the LIF camera and f incorporates all the spatial variation effects.

The LIF calibration should serve solely to determine the explicit expression for the spatial correction function f. It is evident that the spatial correction function is nonlinear because all the coefficients (extinction coefficient, quantum efficiency coefficient, etc.) that constitute f are nonlinear. As a result, a pixel-to-pixel calibration is used to automatically take into account all the above nonlinearities.

Once the LIF calibration is done, the fluorescent intensity may be converted into dye

by calculating

$$C_{\mathrm{f}}(x,y) = \frac{I_{\mathrm{f}}(x,y)}{f(x,y)}. \tag{2.30}$$

Again, it worth noting that the above equation is a pixel-wise expression; that is to say, the concentration is calculated for every pixel in the image.

2.4.3 LIF Instrumentation

Based on the principles of LIF measurement, the main components of the LIF system include the laser, the fluorescence dye, and the camera. The PIV measurement and LIF system share the same laser, and descriptions of the laser can be found in §2.3.2. Therefore, only information regarding fluorescence and LIF camera will be discussed in the discussion of LIF instrumentation.

The Fluorescent Dye

There are many laser dye options. In past research, Rhodamines were widely used as fluorescence dyes because of their excellent photophysical properties. Petracci et al. (2006), for example, used Rhodamine b as the fluorescence dye for LIF measurement, while Parker et al. (2020) used Rhodamine 6G as the dye for LIF. According to the logistics of the lab, both dyes are available to choose.

Rhodamine 6G was chosen as the fluorescent dye, and there are two reasons for the choice. The first reason is to match the mass transfer process of Rhodamine 6G and sodium sulfate. Since Troy and Koseff (2005) showed that the mass transfer for Rhodamine 6G and sodium sulfate is similar, the concentration of sodium sulfate can be easily deduced from the concentration of Rhodamine 6G based on Eq. 2.27. It is not very clear, however, whether Rhodamine b also shows a similar mass transfer process as sodium sulfate. Therefore, Rhodamine 6G is preferred over Rhodamine b from the mass transfer perspective.

The second reason for choosing Rhodamine 6G is to exclude the effect of temperature variation. Rhodamine b is sensitive to temperature changes, while Rhodamine 6G is less sensitive to temperature variations. Liu et al. (2022) gave a set of experimental data on fluorescence emission spectra for different Rhodamine solutions under different temperatures, and it was concluded that Rhodamine 6G showed less temperature sensitivity than its counterparts. Choosing Rhodamine 6G helps to mitigate the temperature-variation effects in the lab room.

In terms of photophysical properties, Rhodamine 6G is also a good choice. For Rhodamine 6G (Fig. 2.20), the peak excitation wavelength is around 530 nm (C. Beaumont et al., 1993; Liu et al., 2022), which is close to the laser's wavelength of 527 nm. Moreover, the peak emission wavelength is around 550 mm (C. Beaumont et al., 1993), which

implies that by applying appropriate filters, it is possible to separate the fluorescence from other lights of different wavelengths.

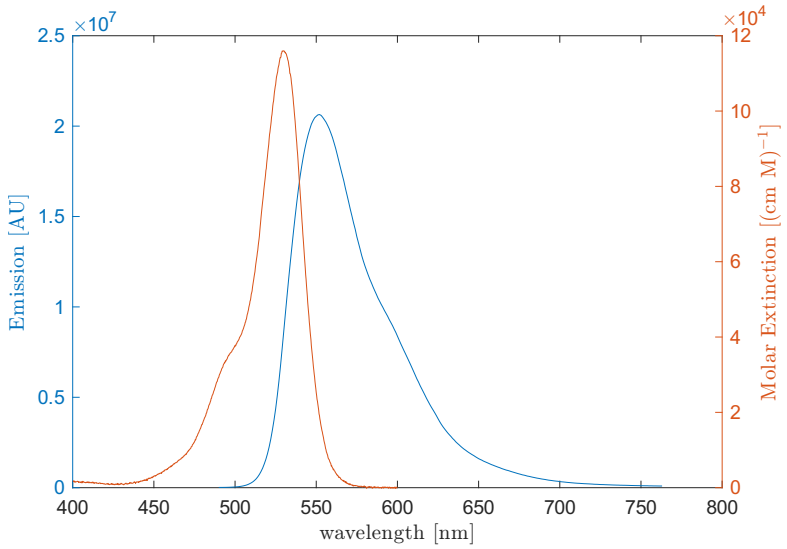

Figure 2.20: Extinction and emission data of the LIF dye Rhodamine 6G(Dixon et al., 2005).

The LIF Camera

Another camera with the same lens as the PIV camera was used for LIF imaging, except a different filter must be applied. In order to overlap the field of view on both PIV and LIF cameras as much as possible, the same type of CMOS camera and lens were used in the experiment. Nonetheless, a longpass filter must be used to block the signal from PIV. Because the PIV particles scatter the laser without changing its wavelength (527 nm), whereas the LIF dye fluoresces at a longer wavelength (around 550 nm), the longpass filter should attenuate shorter wavelengths and transmit longer wavelengths. The Schott OG570 longpass filter has been used on the LIF camera, and this filter allows wavelengths greater than 560 nm to pass while effectively blocking wavelengths shorter than 530 nm (Schott, 2023).

3

Experiment Configurations

The previous chapter explained the main methodology behind the experiment, and this chapter discusses the necessary preliminary steps before any measurement can be performed. These steps include a plume visualization to locate the measurement region (§3.1) and experiment apparatus calibration (§3.2).

3.1 Choose Measurement Region

A trial experiment was performed to visualize the plume, to estimate the measurement location, and to check the available measurement time window and other time scales. Despite the fact that a CFD simulation has been carried out, a trial experiment is necessary, given that real experiments can differ from simulations due to many different factors, such as small vibrations or disturbances, and simulations can also be different from reality due to turbulence modeling.

Since both the sodium sulfate solution (the dense liquid) and the freshwater (the light liquid) are both clear liquids (colorless liquids), visualizing the plume requires dying the fluid. In this experiment, the sodium sulfate solution was colored with methylthioninium chloride (also know as methylene blue). And the evolution of the plume was recorded by a phone camera mounted on a tripod.

3.1.1 Plume Evolution and "Filling Box" Effect

The visualization confirms that the plume is turbulent (Fig. 3.1). Soon after the heavy liquid leaves the nozzle, instability develops, and the plume becomes turbulent. The result confirms the theoretical prediction mentioned in §2.1.1 as the Reynolds number is greater than 30, and the plume should be turbulent.

Figure 3.1: The plume is turbulent. After the injection, the plume becomes unstable, as can be seen from the meandering pattern of the plume. The instability soon develops into a turbulent motion of the plume because the flow shows a chaotic fashion.

A "filling box" effect (Fig. 3.2) described in the work of Turner (1973) should be expected because the experimental setup is of finite size. The "filling box" effect refers to the phenomenon that once the heavy fluid released from the top falls to the bottom of the tank due to the buoyancy effect, it begins to accumulate because the plume is continuously supplied until the whole container is filled with the plume. The "filling box" effect implies that a stable stratification may be observed as the plume accumulates on the bottom of the tank.

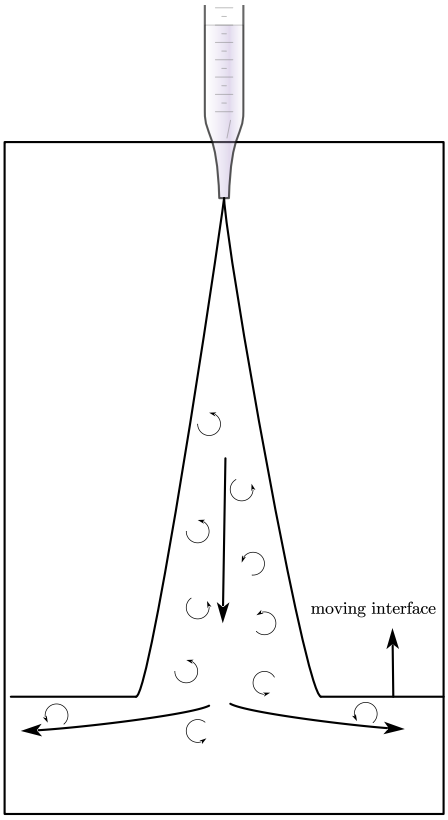

Figure 3.2: The "filling box" effect. The heavy fluid accumulates on the bottom of the tank, and the interface between heavy fluid and lighter fluid will move upwards continuously.

The stable stratification can be explained by the entrainment process. As the heavy plume leaves the nozzle and falls to the bottom of the tank, it will lose buoyance due to mixing with the entrained fluid. Because the tank may not be large enough, the plume may reach the boundary without losing all the buoyancy. Hence the plume will stay on the boundary due to the leftover buoyancy. However, since the plume is being supplied continuously, more and more plume fluid enters the accumulated heavy-fluid layer. This implies that plume fluid shall begin to entrain and mix with heavier fluid (rather than pure light liquid), which means that the buoyancy losing rate is further lowered, and the density of the plume remains relatively unchanged after entering the stratified layer. Therefore, a stable stratification of the plume should be observed because heavier plume fluids tend to rest on the bottom.

This plume visualization clearly illustrates the "filling box" effect. Figs. 3.3 showed the evolution of the plume: After around 16.5 seconds, the plume's cap is just about to touch the bottom surface of the tank and another 5 seconds later, the plume begins to sit on the bottom. With the plume being constantly supplied, the heavy dense accumulates, and the interface (outlined by red lines) begins to move upward.

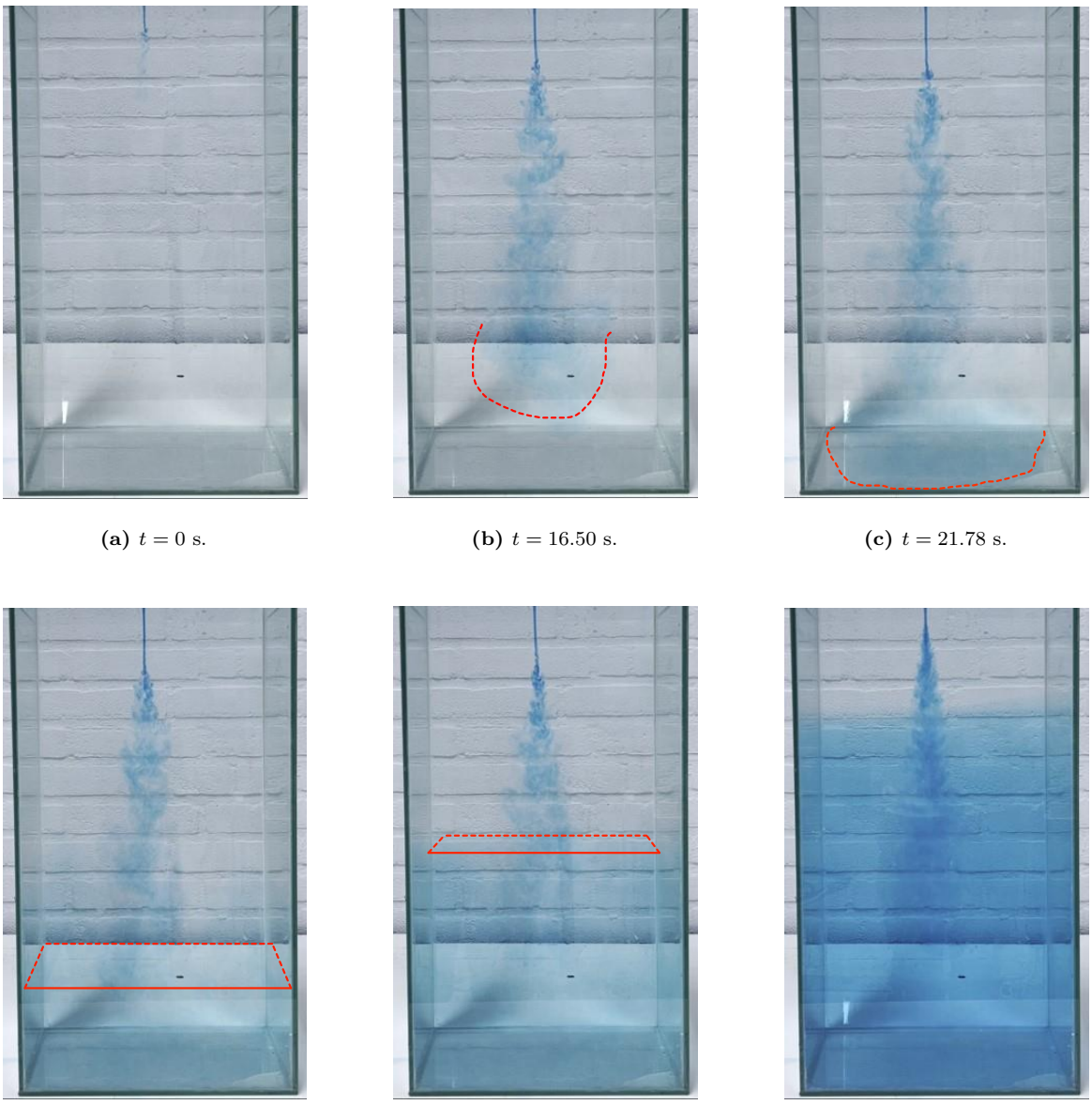

(a) $t = 0$ s. **(b)** $t = 16.50$ s. **(c)** $t = 21.78$ s.

(d) $t = 40.92$ s. **(e)** $t = 65.01$ s. **(f)** $t = 260.21$ s.

Figure 3.3: The "filling box" effect visualization. (a) the initialization of the plume. (b) The plume's cap is about to touch the bottom surface, and the red dashed line is the outline of the plume. (c) The plume begins to accumulate on the bottom, and the red dashed line is the outline of the plume. (d) and (e) the interface of dense fluid and light fluid (highlighted by red lines) keeps rising. (f) Stable stratification.

3.1.2 Estimate Measurement Location

The "filling box" effect puts a fundamental restriction on the measurement region both spatially and temporally. First, let's consider the location of measurement. On the one hand, it is necessary to keep the measurement region above the interface between accumulated dense fluid and light fluid. Because once the plume enters the accumulated layer, it begins to mix with a fluid whose density differs from the fresh tank fluid. Avoiding

measuring in the accumulated layer ensures that the local boundary condition, namely the uniform density outside the plume stream, remains consistent. If one fails to do so, it will be possible to obtain a misleading result as the boundary condition changes within the measurement region. On the other hand, one needs to keep the measurement region away from the inlet. Because if the measurement region is chosen too close to the nozzle outlet, the nozzle outlet boundary condition may affect the measurement; in addition, the plume may still be in the transition phase, while only the turbulent entrainment is of interest.

Then let's consider the time restriction. Recall that in §2.1.1, it was mentioned that there exists an available measurement window τ_{avail}, which should be much greater than both the eddy turnover time τ_{eddy} and the eddy traverse time τ_{trav}. The τ_{avail} is a limit beyond which the measurement will be affected by the undesirable "filling-box" effect. In our case, this translates to the time point *before* which the interface (between accumulated dense fluid and fresh tank liquid) enters the measurement region. Therefore, in our case, the τ_{avail} is the time range between the time point when the turbulent plume stream is completely formed in the measurement region and the time point when the interface just rises to the boundary of the measurement region.

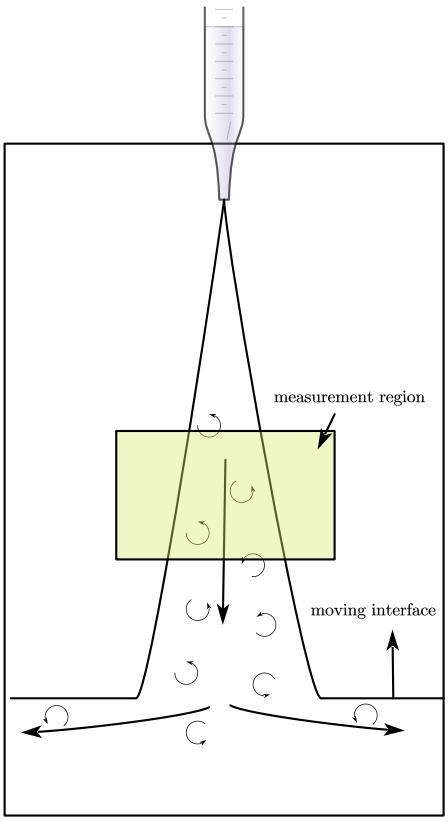

Figure 3.4: Sketch of the measurement location.

The above spatial restriction and temporal restriction limit the possible locations of the measurement, and introduce a trade-off. If the measurement location is chosen to be very close to the nozzle, one may have a very long measurement window (hence a large τ_{avail}) because it takes longer for the interface to rise to that measurement region; yet, one cannot get rid of the inlet condition because the measurement is too close to the inlet. If the measurement location is lowered, one can stay away from the nozzle inlet, yet the available measurement time τ_{avail} is reduced because it takes less time for the interface to reach the measurement region and start affecting the concentration measurement accuracy.

To maximize τ_{avail} while minimizing the effects of nozzle outlet conditions, one can examine the time-averaged image to determine the measurement location. Starting from the first frame recorded, a total of 150 frames were used to calculate the average, and the time average of the plume is obtained in Fig. 3.5. Since the geometry of the tank is known, the geometry of the measurement region can also be estimated by counting pixels, and the result is sketched in the same figure.

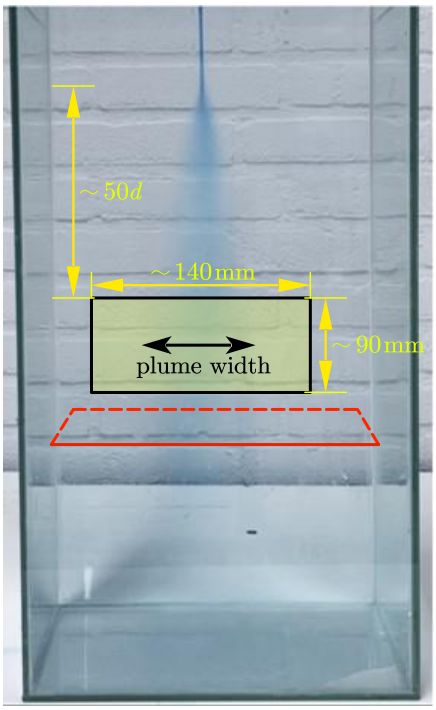

Figure 3.5: Time-averaged plume evolution. The time range used for averaging is between 0 seconds and 95.73 seconds. The red line is an indication of the location of the interface in the last frame. The light yellow rectangle is the proposed measurement region, whose geometry and relative location (the distance from the nozzle inlet) are highlighted by yellow dimension readings.

3.1.3 Check Time Scales

The last conclusion that can be derived from the trial visualization is the estimation of various scales mentioned in §2.1.1. Among all the scales, time scales will be checked so that the measurement can represent the time-averaged entrainment process.

First, consider the eddy traverse time. The camera recorded the moment when an eddy was just about to enter the measurement region and when the eddy was going to leave (Fig. 3.6). The eddy traverse time is, therefore, calculated by the time difference between the above two moments. Therefore, the eddy traverse time is $\tau_{\text{trav}} \simeq 4\text{s}$.

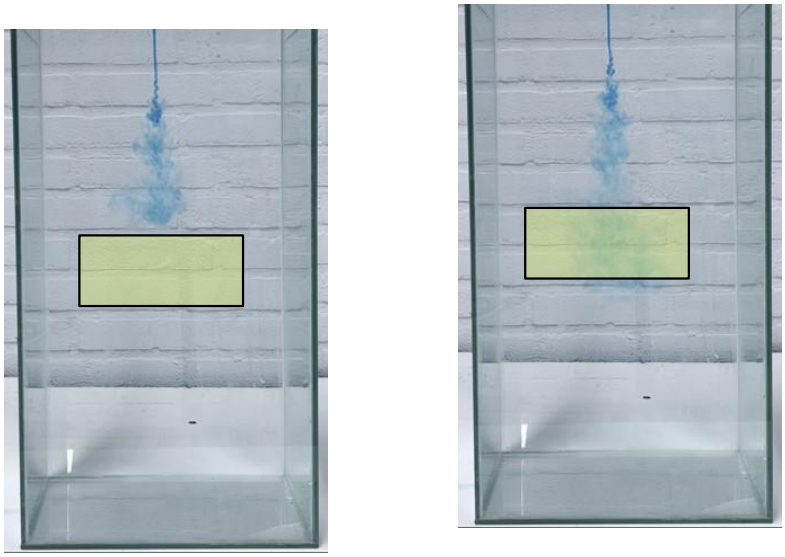

(a) The instantaneous photo when the first eddy is just about to enter the measurement region.

(b) The instantaneous image taken after 3.96 seconds, the same eddy in the previous photo will soon leave the measurement region.

Figure 3.6: Derivation of the eddy traverse time.

The vertical velocity scale $\mathcal{U}$ is then readily available. Since the eddy traverse time is known, and the vertical length of the measurement region L is also a constant, the vertical velocity scale is $\mathcal{U} \simeq \frac{L}{\tau_{\text{trav}}} \simeq \frac{0.09}{4} \simeq 0.023$ m/s.

Next, consider the eddy turnover time. By examining known dimensions, such as the tank's width, the plume's half width is estimated to be $\mathcal{L} \simeq 42\text{mm}$ (observed from the image by counting pixels). Therefore the eddy turnover time is $\tau_{\text{eddy}} \simeq \frac{\mathcal{L}}{\mathcal{U}} \simeq \frac{42}{23} \simeq 1.82$ s.

All the time scales should compare with the available time scale so that the measurement reflects the time-averaged entrainment properties. Since the available time window for measurement is $\tau_{\text{avail}} \simeq 90$ s, it is evident that $\tau_{\text{avail}} \gg \tau_{\text{eddy}}$ and $\tau_{\text{avail}} \gg \tau_{\text{trav}}$, it is therefore concluded that time scales satisfy the criteria mentioned in §2.1.1.

3.2 Calibrate the Setup

The last step before performing experiments is calibration, and this section describes how the setup was calibrated. In the current investigation, there are three major components to be calibrated: the peristaltic pump, the PIV system, and the LIF system. We shall start with the pump calibration.

3.2.1 Calibrate the Pump

The pump's speed dictates the amount of liquid that will be injected into the water tank, and the purpose of calibration is to obtain the relation between pump speed and the volume flow rate. As explained in §2.2.1, the experiment parameters can be specified by changing the Reynolds number and the Richardson number, and by varying the pump speed, the volume flow rate (thus the Reynolds number) can be changed. As a result, it is necessary to know the relation between pump speed and volume flow rate.

The pump is calibrated by recording the time needed to pump out a certain amount of plume. First, several marks were made on the gas-washing bottle such that the volume difference between any two adjacent marks is 100 ml. Then, for four different pumping speeds, the time required for the pump to purge out 100 ml is recorded (by a stopwatch), and the procedure is repeated five times.

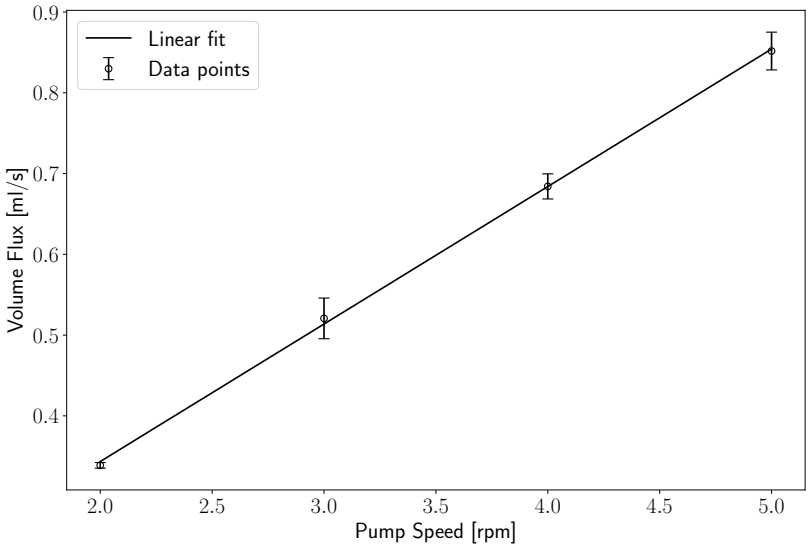

Figure 3.7: Pump calibration curve. Since five volume flow rates are available for each pumping speed (as time is recorded five times for each pumping speed), the error bar may be estimated using the standard deviation of these five volume flow rates.

3.2.2 Calibrate PIV

The PIV measurement requires position calibration, which is done by placing a target with a known geometric pattern in the water tank, as shown in Fig. 3.8. The target has a large array of dots engraved on it, and the distance between two dots is 15 mm. Since the geometry of the calibration target is known, its image can be used to calibrate the PIV system.

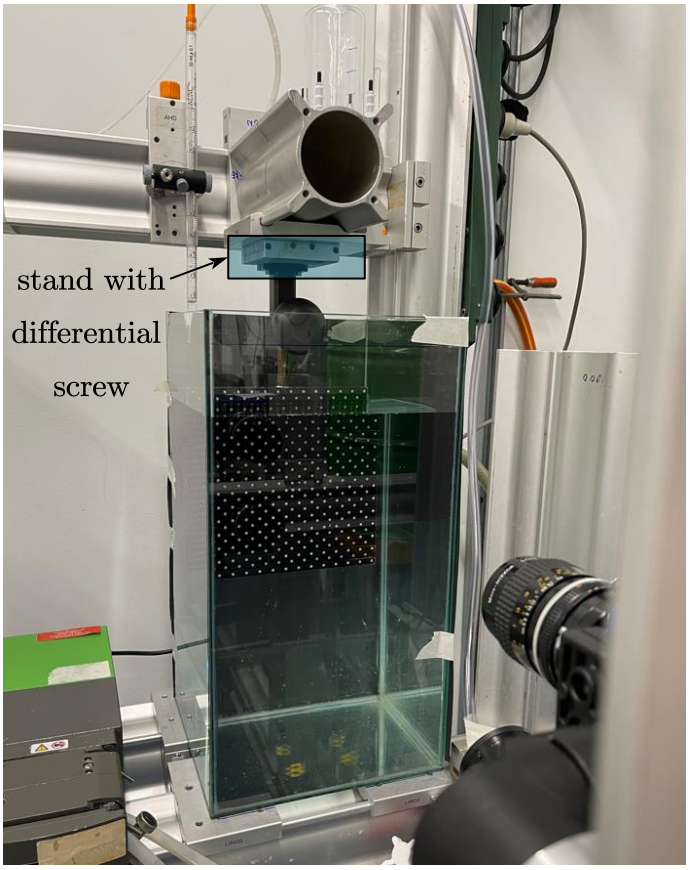

Figure 3.8: PIV calibration plate.

The target plate should be positioned correctly. On the one hand, the plane of the dotted array should be at the same location as the laser sheet, and the position of the calibration plate can be adjusted precisely with a differential screw stand. Moreover, the light sheet (and hence the plate) should be positioned at the required location such that the nozzle's axis is on the calibration plate's plane.

3.2.3 Calibrate LIF

As outlined in §2.4.2, the goal of the LIF calibration is to obtain the calibration function f in Eq. 2.30, which enables converting the measured fluorescent intensity to the local concentration. The method to find the calibration function is to measure the fluorescence

intensity in the water tank, whose dye concentration is uniform and known. Once the intensity I and the concentration C are known in Eq. 2.30, the calibration function can be easily calculated for every pixel. The uniform concentration C of the water tank may be accurately controlled by the amount of Rhodamine 6G dye added to the water tank. For this purpose, a sophisticated pipette from the chemical lab was used to transfer Rhodamine 6G dye to the water tank with high precision ($\pm$0.01ml).

It should be noted that by calibrating every pixel separately, the spatial variations of both laser and fluorescence intensity are considered automatically. Fig. 3.9 is a sample calibration image and it clearly indicates the distribution of fluorescence intensity in space. To take into account the spatial variation automatically, one can calibrate each pixel separately.

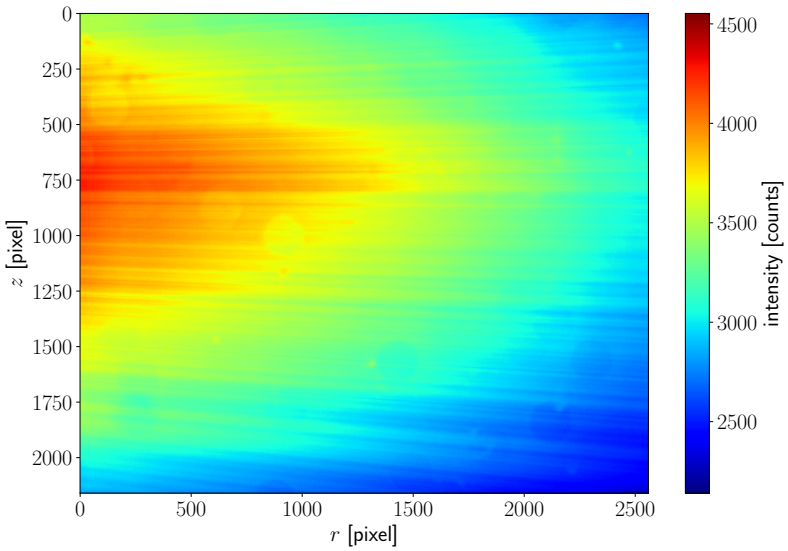

Figure 3.9: Fluorescence intensity distribution over the measurement plane (Rhodamine concentration is 16.5 μg/l). Vertically, a Gaussian-like distribution of intensity pattern can be observed, and this distribution may be attributed to the expanding laser sheet. Horizontally, decreasing fluorescence intensity can be identified, and this phenomenon can at least be partly attributed to the absorption of the fluorescence dye in the water tank.

Before the pixel-wise calibration can be applied, two problems must be addressed: where is the linear response of the fluorescence dye, and is the calibration valid? We start by finding the linear range of LIF response, and after that, a discussion of the calibration's validity will be given.

Determine the Linear Range of Fluorescence Dye

It is necessary to find the linear response range of the fluorescence dye. It should be noted that Eq. 2.30 is based on the assumption that the relation between fluorescence

intensity and concentration is linear, and numerous factors can render the response to become nonlinear, such as a high concentration of fluorescence dye. Fig. 3.10 presents the plot of image (mean) intensity against dye concentrations in the water tank, and it is clear that with a concentration higher than 40 μg/l, the response is nonlinear. In other words, it is necessary to carry out measurements with a concentration lower than 40 μg/l.

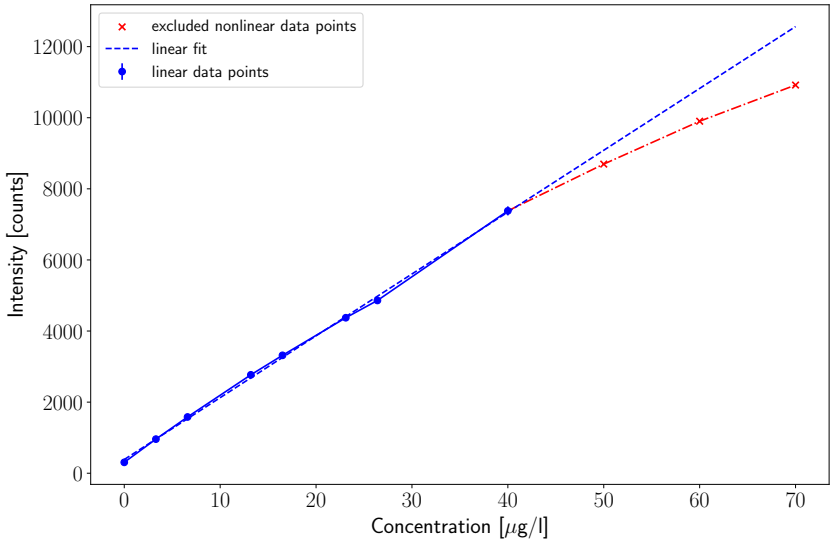

Figure 3.10: The overall image mean intensity and the fluorescence dye concentration plot. With a concentration higher than 40 μg/lthe fluorescence intensity becomes nonlinear. As a result, LIF calibration only uses data points in the linear range (blue points in the plot).

Nonetheless, the above linear response range is *not* the only constraint for the measurement. Another constraint is the calibration's validity, and the reason is evident: if the calibration cannot represent the experiment, the concentration will be wrong. The validity of calibration will be discussed in the following content.

On the Validity of LIF Calibration

Since LIF calibration is done with the water tank directly, one problem needs to be considered. Recall that in §2.4.2 it is explained that laser intensity decreases as the laser passes through a medium with fluorescence dye. One major concern about using the water tank to calibrate LIF is that the laser light could be absorbed before it reaches the measurement region. In other words, if the calibrations are done with the fluorescence dye presented in the whole water tank, the fluorescence dye will absorb part of the laser before the laser reaches the measurement region; however, in real experiments, fluorescence dye is *only* present in the plume, and the laser light will not be absorbed

before it reaches the plume. This laser intensity difference in calibration and experiment would introduce errors if left untreated.

The error may be better understood by considering the LIF principles mentioned in §2.4. The LIF is a two-stage process–the fluorescence molecules absorb laser light in the first stage and fluoresce in the second stage—and this means any variation in the process (local laser intensity, for example) causes the measured fluorescence intensity to change (Fig. 3.11a). Consider the local laser intensity on the tank's centerline, assuming the dye concentration is the same both in calibration and real experiments. Since the local laser intensity is different in calibration and real experiments, the measured fluorescence intensity at the point will *not* be the same even if the concentration is the same (Fig. 3.11b).

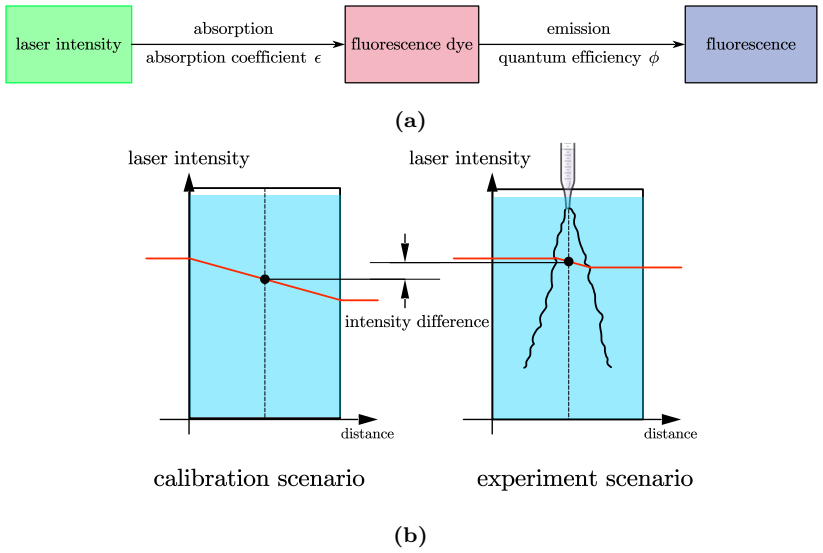

Figure 3.11: (a) Principles of LIF: A two-stage process. Any variation in the process, be it a variation in laser intensity or the concentration of the fluorescence dye, will change the measured fluorescence intensity. (b) Local laser intensity change in calibration and experiment. In the calibration, laser intensity constantly decreases once it enters the tank, while in the experiment, laser intensity only decreases when it touches the plume.

Specifically, the error will result in an overestimation of the dye concentration. The fluorescence intensity increases with the local laser intensity. Because the local laser intensity at the same point in experiments is higher than in the calibration, the image will perceive a higher fluorescence intensity in the experiments. The higher fluorescence intensity will, in turn, cause a higher estimation of the fluorescence concentration (see the linear calibration curve in Fig. 3.10).

A natural solution to the above concern is to find a condition under which the local laser intensity difference in calibration and experiment can be ignored. In other words, if the attenuation introduced by the fluorescence dye in the water tank is negligible, the laser intensity difference in calibration and experiment may be ignored. The condition,

as mentioned in §2.4.2, is termed *optically thin*. And according to Melton and Lipp (2003), as long as $\epsilon \int_{r_0}^{r_1} C(r)dr \leqslant 0.1$ (where r_0 is the starting point of the laser ray path and r_1 is the end point) the system can be regarded as optically thin and the measurement error is acceptable.

The system is optically thin only when the concentration is below 20 μg/l. The mean intensity difference of the first column of pixels on the left side and the middle column of pixels in the center of the image is calculated under different Rhodamine 6G concentrations. The results are plotted in Fig. 3.12, and this figure suggests that it is desirable to keep the Rhodamine 6G concentration lower than 20μg/l so that the intensity difference is kept within 10% and the system is optically thin.

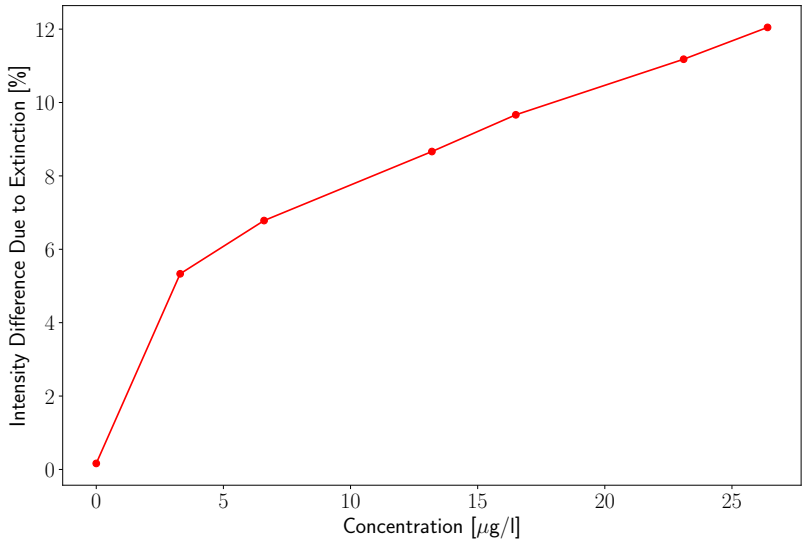

Figure 3.12: The mean intensity difference between the first and the center columns of pixels in the image under different LIF dye concentrations. The intensity difference increases as the fluorescence dye concentration increases. Specifically, when the concentration of fluorescence dye is higher than 20 μg/l, the system is no longer optically thin, and the calibration curve, even within the linear response range, cannot be justified to represent the situations in the experiment.

4

Results and Discussions

Under the guidance of experiment methodology in chapter 2 and experiment configurations in chapter 3, 20 sets of simultaneous PIV-LIF measurements were performed (see table 2.1). In these 20 measurements, 10 of them are under refractive index matching (RIM) condition, while the others were performed without RIM (all the other experimental parameters were kept unchanged except the refractive index). For all 20 sets, data were collected at 7 Hz, which corresponds to a time step size of around 0.14 seconds. For each set, a number of 1740 frames in total were recorded, and this translates to 580 measured velocity and density fields. Fig. 4.1 presents one sample (instantaneous) result from the 580 measured velocity and buoyancy fields.

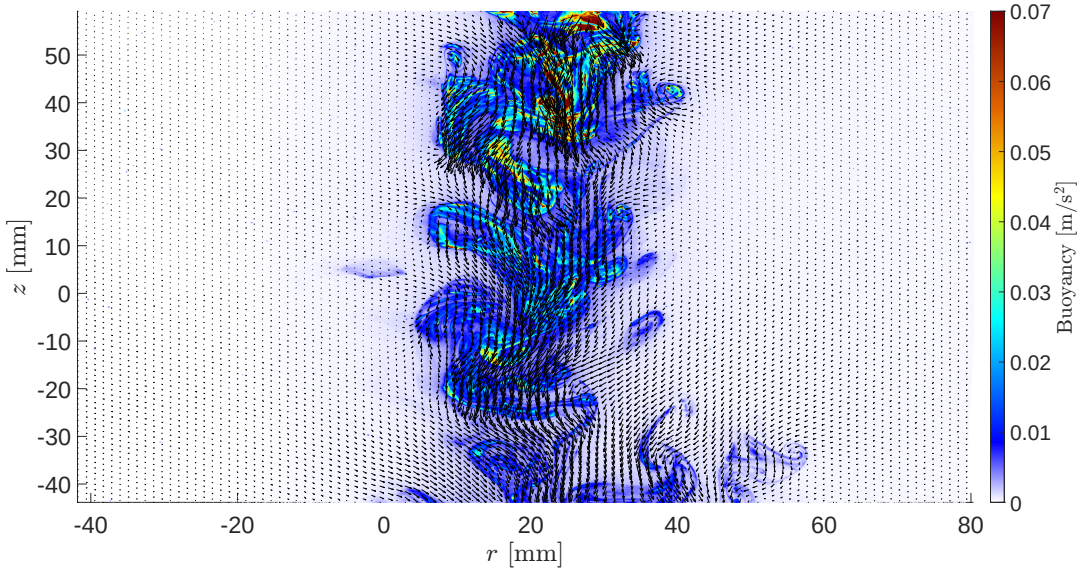

Figure 4.1: Velocity vector field and buoyancy scalar field. (Flow condition: No. 17. See table 2.1.)

This chapter presents and discusses the results of the above measurements. First, for measurements with RIM, the plume turbulence statistics will be analyzed in §4.1. Correspondingly, the measured entrainment coefficients in different sets will be discussed in §4.2. Then, §4.3 examines the effect of RIM by comparing measurements with and without RIM. Last, §4.4 compares CFD simulation results with the experiment, highlighting significant discrepancies.

4.1 Turbulent Statistics

Recall it was explained in chapter 1 that the entrainment coefficient model is a quasi-steady description of a complex plume entrainment process, and as a result, it is important to check the turbulent statistics. This section analyzes the turbulence statistics: In §4.1.1, the mean flow properties will first be analyzed, and the self-similarity shall offer us evidence of measurement validity. After that, in §4.1.2, the turbulence correlations in our flow are discussed in an attempt to investigate the turbulence structure.

4.1.1 Mean Flow Analysis

Mean flow analysis provides direct information regarding the plume evolution. Although 580 velocity and buoyancy fields are obtained for each experimental condition, plotting all the results as in Fig. 4.1 would not be beneficial. On the other hand, the mean velocity field and mean buoyancy field may give insightful information about the trend of plume evolution. We start by analyzing the mean velocity field.

Mean Velocity Field

The mean flow field is calculated by taking the ensemble average of each velocity component for the 580 velocity fields recorded, and the result is shown in Fig. 4.2. Along with the vector plot, the velocity magnitude is also given by the contour. Two observations are readily available qualitatively. First, it can be seen that the plume center has the highest velocity magnitude, and the vertical velocity component u_z dominates motion in the center because most arrows point downward. Second, the entrainment process may be observed at the (averaged) interface of the plume body and ambient fluid (the blue zone in the figure), as the velocity has a component towards the center.

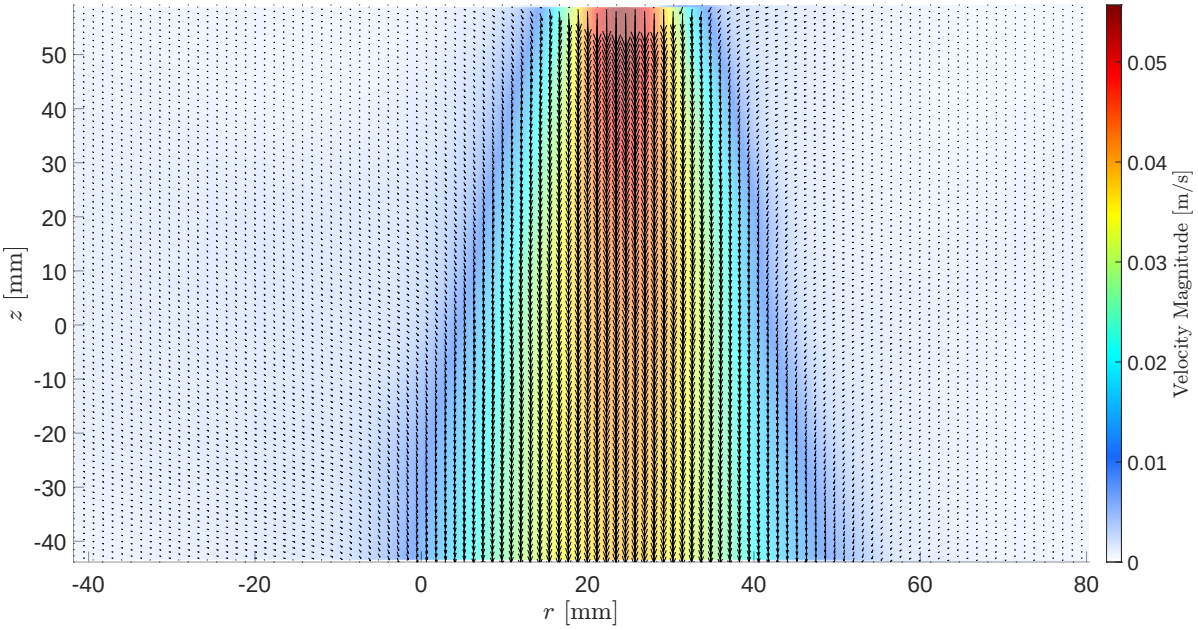

Figure 4.2: The mean velocity field with the background scalar field being the velocity magnitude (Case No. 17).

More insightful information may be obtained by considering the self-similar property of the plume, which also serves as a validation for the measurement. Recall from §2.2.1 that the plume was said to be self-similar after a distance of 10 times the nozzle outlet diameter d. Therefore experiment is expected to reveal self-similar because the field of view starts at around 36 times the diameter. To check the self-similar velocity profile, consider several horizontal lines in the above velocity field. For every horizontal line, the vertical velocity components should form a certain profile (approximately Gaussian-like profile). The profiles on different horizontal lines should collapse onto each other if the velocity is normalized by the centerline velocity and the r coordinate is normalized by the plume width. In our calculations, the centerline velocity u_{zc} and plume width r_c are defined by the following formula

$$u_z\left(r,z\right)=u_{zc}\left(z\right)\exp\left[-\frac{\left(r-r_0\right)^2}{r_c^2\left(z\right)}\right],$$

where u_{zc} and r_c are functions of z coordinate only and r_0 is the centerline's coordinate. To determine u_{zc}, r_c, and r_0, one may use Gaussian curve fitting. The normalized velocity profiles are plotted at different z coordinates, and the result is shown in Fig. 4.3.

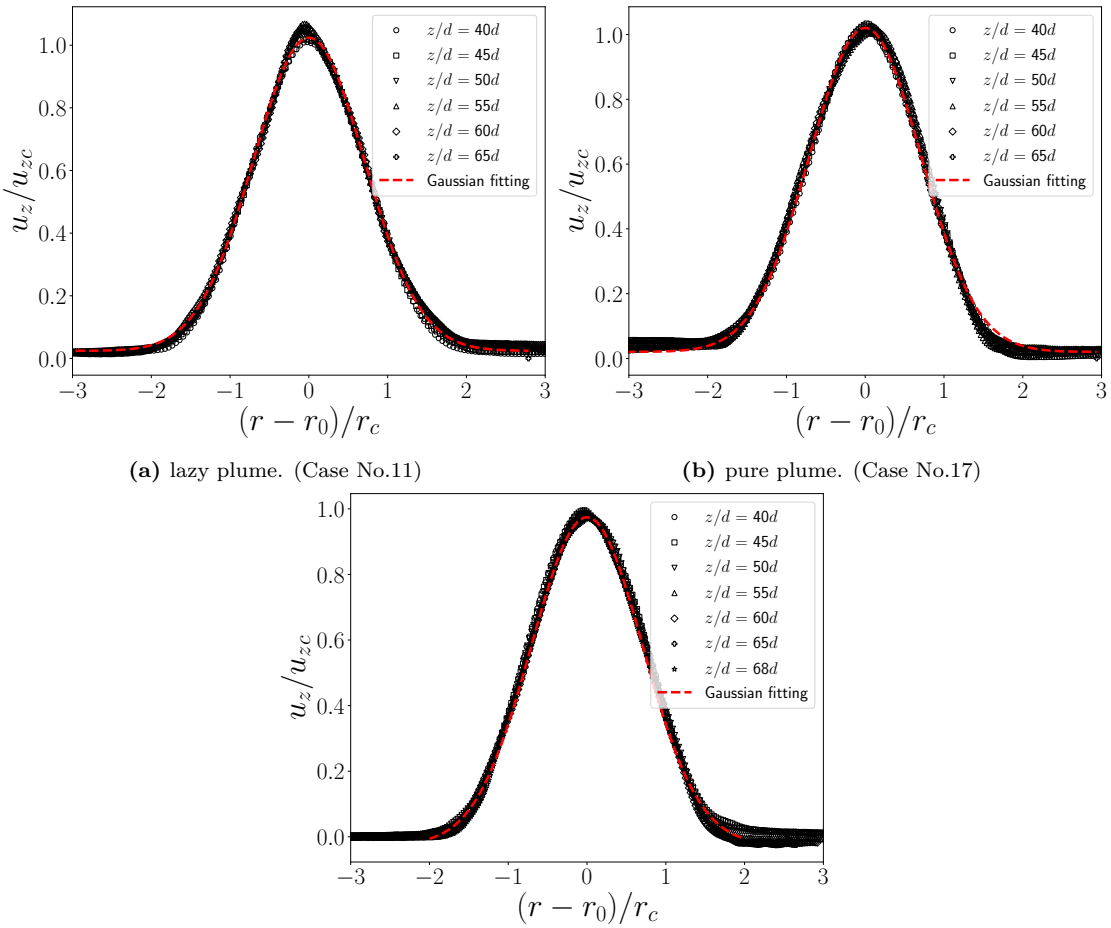

(a) lazy plume. (Case No.11)

(b) pure plume. (Case No.17)

(c) forced plume. (Case No.19)

Figure 4.3: Mean velocity self similarity observed in all plumes.

Besides showing self-similarity, the mean velocity field also gives information about the vertical evolution of the plume. We will consider two quantities in terms of the plume's vertical development, the first quantity is the plume width growth, and the second is the centerline velocity.

Theoretical analysis implies that the plume's half-width (or simply width r_c) should scale linearly with the distance from the virtual origin, which also implies it should scale linearly with z coordinate (Bejan, 2013). Fig. 4.4 plots the plume's width (normalized by the nozzle outlet diameter) against the vertical distance from the nozzle outlet (normalized by the nozzle diameter). It is clear that the width shows a linear growth, matching the theoretical analysis. Note that the plot has used the distance from the nozzle (not the distance from the virtual origin), but this does not change the fact that the plume follows a linear scaling growth.

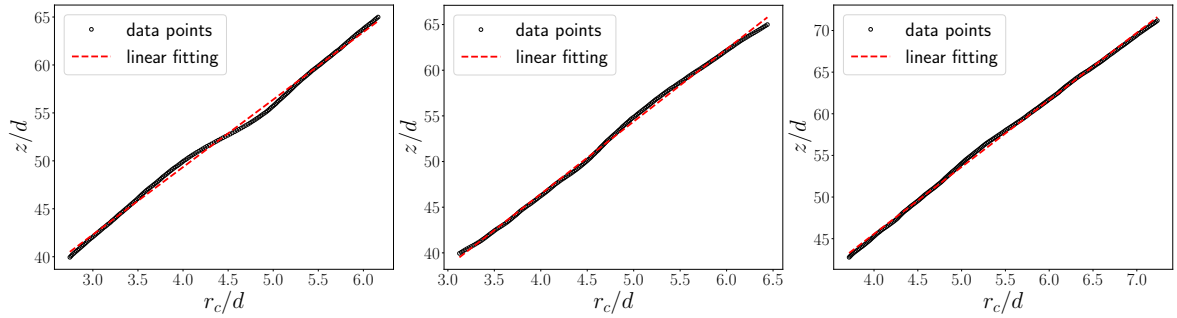

(a) lazy plume. (Case No.11) **(b)** pure plume. (Case No.17) **(c)** forced plume. (Case No.19)

Figure 4.4: The vertical evolution of plume width.

For the centerline velocity, Bejan (2013) shows that the centerline velocity scales with z^{-1} for pure turbulent jet but scales with $z^{-1/3}$ for plume (again, z is the distance from the virtual origin). Fig. 4.5 plots the centerline velocity of different plumes (normalized by the nozzle outlet velocity) against normalized distance (on a log scale). The results presented a somewhat counterintuitive feature as the pure plume and lazy plume are in the transition phase from a jet-like plume to a pure plume, while the forced plume behaves like a pure plume in the FOV. The reason could be that while the source Richardson number (at the nozzle outlet) has been used to identify different plume regimes, the plume may have evolved into a different form before it reached the field of view.

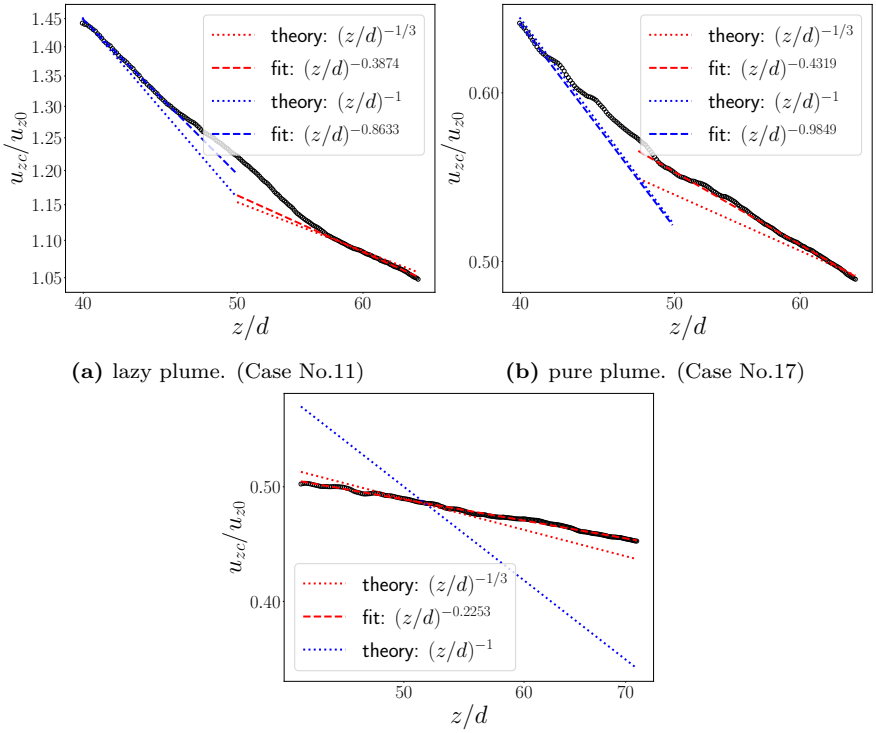

(a) lazy plume. (Case No.11) **(b)** pure plume. (Case No.17)

(c) forced plume. (Case No.19)

Figure 4.5: The vertical evolution of centerline velocity. Plots are in log scale.

Mean Buoyancy Field

The first step in obtaining the mean buoyancy field is to convert the averaged LIF image into the buoyancy field. Since the pixel intensity of every image is known, the LIF calibration information can then be used to convert intensity into fluorescence dye concentration, which can be used to calculate the concentration of sodium sulfate according to Eq. 2.27. Once the sodium sulfate concentration is known, the buoyancy is readily available by calculating the density according to the data provided by Haynes (2016).

Once the instantaneous buoyancy fields are obtained, the mean buoyancy field is obtained by taking the ensemble average. The result is plotted in Fig. 4.6.

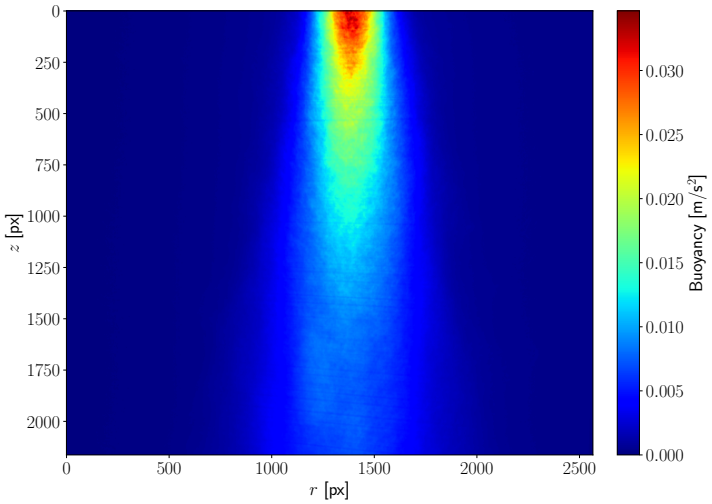

Figure 4.6: A typical mean buoyancy field (case No. 17).

The buoyancy profile is also found to be self-similar. A Gaussian fitting is used to determine the buoyancy profile width r_{bc}, centerline buoyancy b_c, and buoyancy centerline coordinate r_{b0}:

$$b\left(r,z\right)=b_c\left(z\right)\exp\left[-\frac{\left(r-r_{b0}\right)^2}{r_{bc}^2\left(z\right)}\right].$$

Fig. 4.7 shows the self-similar buoyancy profiles of different plumes. There are two things to note regarding the result. First, to a relatively mild extent, on the top region of some of these profiles, there exist some bumps. These bumpy noises are attributed to the fact the LIF is a very sensitive pixel-to-pixel measurement of buoyancy that any perturbation in the experiment (be it a dust particle in the water tank or a tiny bubble on the tank wall) can alter the recorded buoyancy, and therefore increase the noise. Applying a noise filtering technique may well solve this imperfection. Second, by scrupulously examining the horizontal axis value, it may be observed that the width buoyancy profile is a bit narrower compared with the velocity profile, which deserves more discussion.

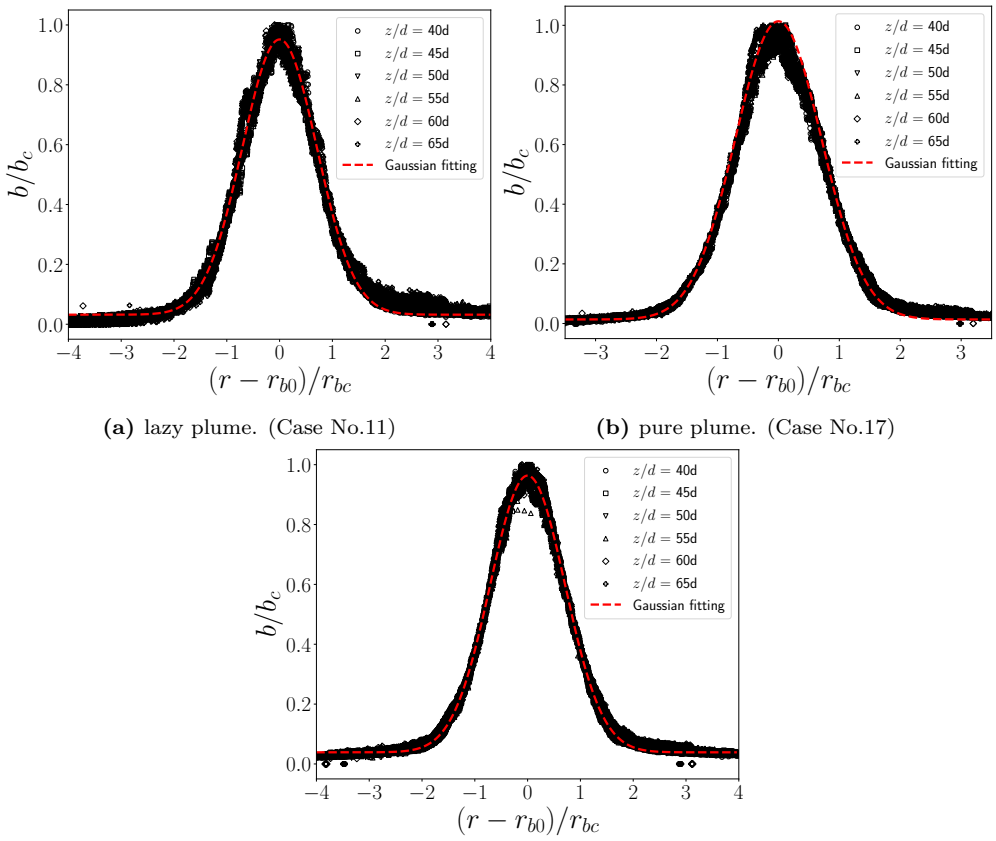

(a) lazy plume. (Case No.11)

(b) pure plume. (Case No.17)

(c) forced plume. (Case No.19)

Figure 4.7: Buoyancy profile self similarity.

The evolution of the buoyancy profile width is shown in Fig. 4.8. Obviously, the plume width follows a linear growth pattern, which should not be surprising because only the plume stream contains buoyancy, and the plume stream grows linearly, implying that buoyancy profile growth should also be linear. What is more striking is the difference between buoyancy profile width and the velocity profile width. Comparing Fig. 4.9 with the velocity profile width (Fig. 4.4), it may be found that the buoyancy profile width is narrower than the velocity profile width. Indeed, the ratio of buoyancy profile width to velocity profile width in Fig. 4.9 confirms this observation despite large variability. This observation stands in contrast to the measurement done by Ezzamel et al. (2015), whose results suggested that the buoyancy profile is wider than the velocity profile; nonetheless, our observation is similar to the study by George et al. (1977), who determined that the ratio is around 0.918. According to Ezzamel et al. (2015) this contradiction has been left unexplained.

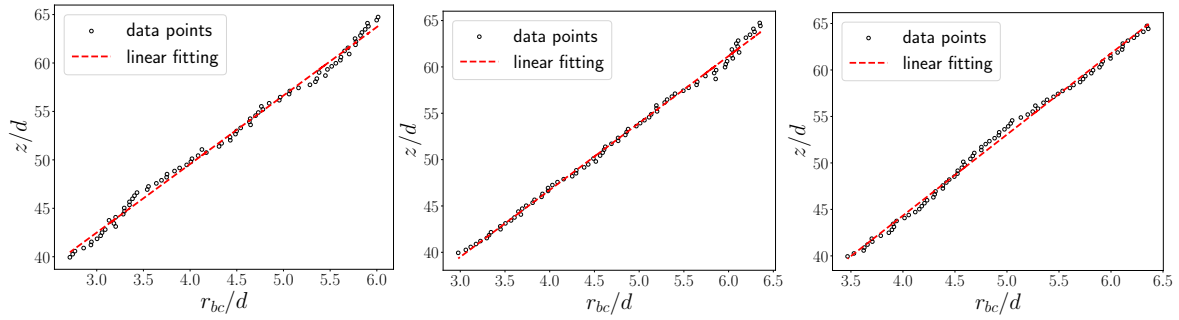

(a) lazy plume. (Case No.11) **(b)** pure plume. (Case No.17) **(c)** forced plume. (Case No.19)

Figure 4.8: Evolution of buoyancy width.

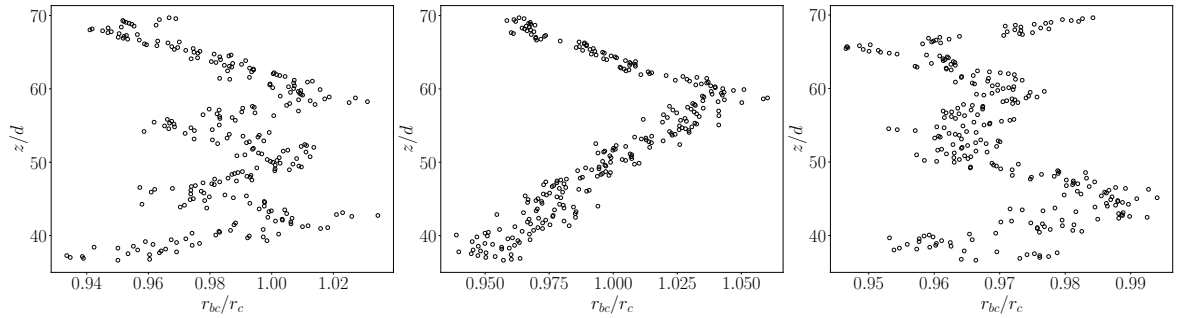

(a) lazy plume. (Case No.11) **(b)** pure plume. (Case No.17) **(c)** forced plume. (Case No.19)

Figure 4.9: Evolution of the ratio of buoyancy profile width to velocity profile width.

To conclude the discussion regarding the mean flow, we examine the centerline buoyancy. Bejan (2013) showed that the centerline buoyancy scales with z^{-1} for jet but scales with $z^{-5/3}$ for plume. The evolution of centerline buoyancy is plotted in Fig. 4.10. The result is consistent with the centerline velocity evolution (Fig. 4.5), that is, the pure plume and lazy plume (classified at the source) are in the transition from forced plume to pure plume, while the forced plume (classified at the source) follows a pure plume scaling in the FOV.

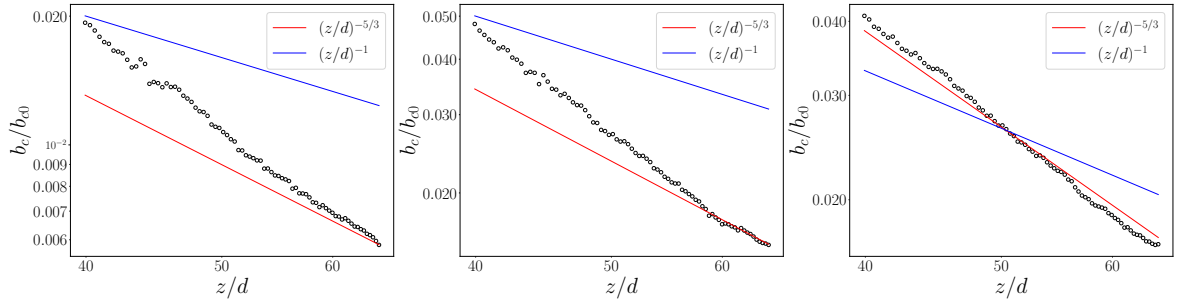

(a) lazy plume. (Case No.11) **(b)** pure plume. (Case No.17) **(c)** forced plume. (Case No.19)

Figure 4.10: Evolution of the centerline buoyancy. Plots are in log scale.

4.1.2 Turbulence Correlations

This subsection examines the turbulence spatial and temporal correlations, and the main purpose is to compare the PIV measurement results with the visualization estimation in §3.1 and to check the time scale mentioned in §2.1.1. The spatial correlation will first be discussed, followed by the time correlation.

Spatial Correlation

The two-point spatial correlation is given by

$$R_1(\mathbf{x},\ \mathbf{r}) = \overline{u_r'(\mathbf{x})\, u_r'(\mathbf{x}+\mathbf{r})} \Big/ \max\left(\overline{u_r'(\mathbf{x})\, u_r'(\mathbf{x}+\mathbf{r})}\right),$$

$$R_2(\mathbf{x},\ \mathbf{r}) = \overline{u_z'(\mathbf{x})\, u_z'(\mathbf{x}+\mathbf{r})} \Big/ \max\left(\overline{u_z'(\mathbf{x})\, u_z'(\mathbf{x}+\mathbf{r})}\right).$$

The above correlations give information about the extent to which the velocity in the flow field at two different locations ($\mathbf{x}$ and $\mathbf{x}+\mathbf{r}$) are correlated with each other (note that $\mathbf{r}$ is a position vector while r is the horizontal coordinate). Specifically, R_1 is the spatial correlation for the radial velocity component and R_2 is the spatial correlation for the streamwise velocity component.

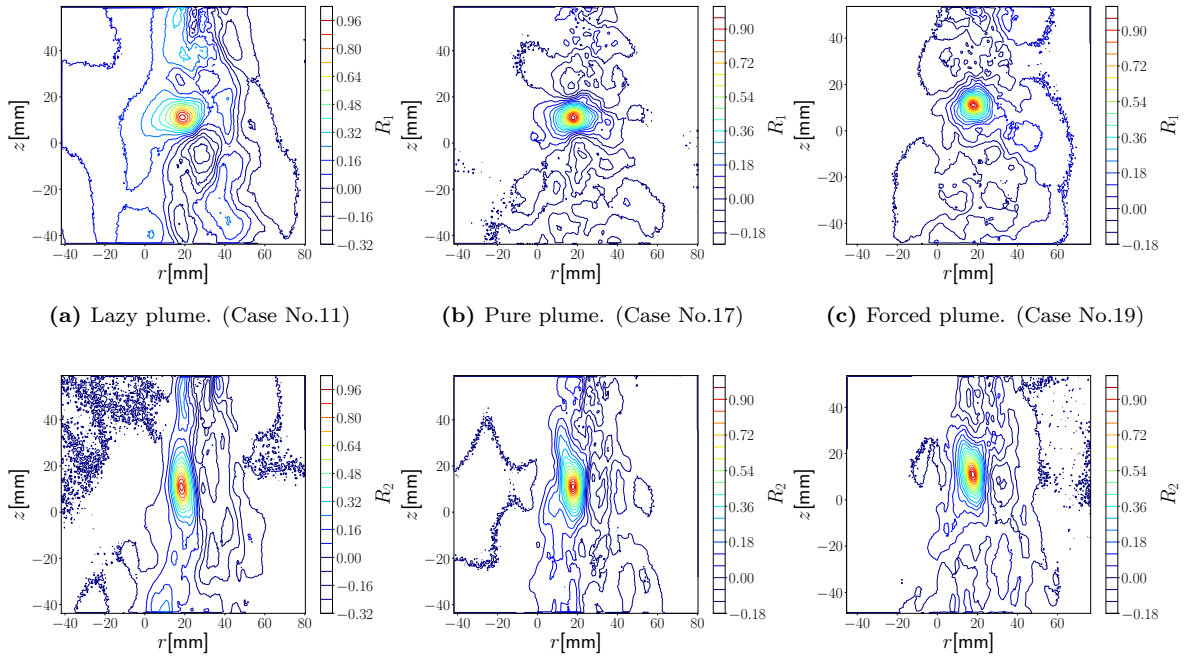

(a) Lazy plume. (Case No.11) **(b)** Pure plume. (Case No.17) **(c)** Forced plume. (Case No.19)

(d) Lazy plume. (Case No.11) **(e)** Pure plume. (Case No.17) **(f)** Forced plume. (Case No.19)

Figure 4.11: Spatial correlation for different plumes. The spatial correlation is calculated using the centerline point (z, r) =(17.7, 11.1) [mm], and this point corresponds to a distance of around $50d$ from the nozzle outlet.

Fig. 4.11 gives the contour plot of correlation for three different plumes. There are two observations. First, the spatial correlation confirms the scaling in §2.1.1. The above correlation indicates the diameter of large eddies is around 27 mm, which is consistent with the half-width given by Fig. 4.4, confirming the scaling analysis in §2.1.1. Second, the spatial correlation shows that the turbulence structure is anisotropy because the spatial correlation in the horizontal direction is different from the vertical direction at the point. Specifically, the diameter of a correlation contour is longer in the vertical direction than in the horizontal direction.

Time Correlations

Next, we consider the time correlations, and it will be shown that these time correlations are consistent with the spatial correlation. The autocorrelation coefficient ρ_u gives information about the correlation of a signal u with the signal itself on different time lags τ.

$$\rho_u(\tau) = \frac{R_u(\tau)}{\lim_{N\to\infty} \frac{1}{N} \sum_{n=0}^{N-1} [u(t)]^2}, \quad \text{with} \quad R_u(\tau) = \lim_{N\to\infty} \frac{1}{N} \sum_{n=0}^{N-1} u(t) \cdot u(t+\tau).$$

The signals, in our case, are different velocity components (u_z or u_r).

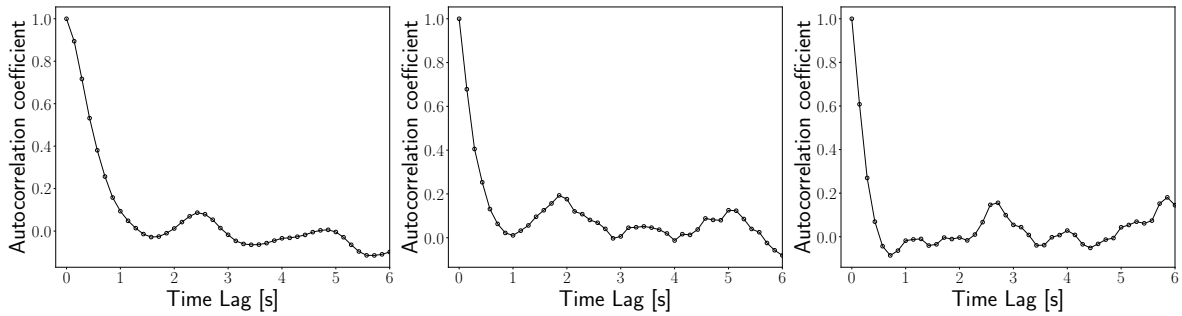

(a) Lazy plume u_z component. **(b)** Pure plume u_z component. **(c)** Forced plume u_z component.

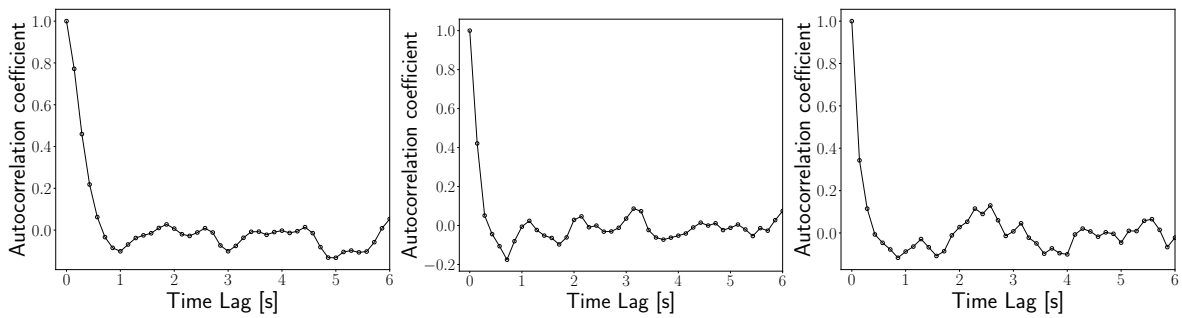

(d) Lazy plume u_r component. **(e)** Pure plume u_r component. **(f)** Forced plume u_r component.

Figure 4.12: Autocorrelation for different plumes.

Fig. 4.12 shows the autocorrelation coefficients for the two velocity components

of different plumes. The time correlations are consistent with the spatial correlation. The lazy plume, for example, whose u_z component needs roughly 1.5 seconds to lose correlation, and the u_z mean velocity at this point is 0.0148 [m/s], suggesting the large eddy size in the streamwise direction is around $1.5 \times 14.8 = 22.2$ [mm], which is consistent with the spatial correlation map in Fig. 4.11d where the diameter of a large eddy is roughly 27 [mm]. Furthermore, it can also be seen that for all three plumes, the u_z component needs a longer time to lose correlation than the u_r component, which agrees with the observations in Fig. 4.11 where the spatial correlation of the u_z component is narrow and slender but the spatial correlation of the u_r component is somehow rounded.

Inconsistency with Visualization

In the previous discussion, it has been shown that (a) the spatial correlation is consistent with the theoretical scaling analysis, and (b) the spatial correlation is consistent with the time correlation. However, there exists an inconsistency with the observations in plume visualization. Table 4.1 summarized the scales results obtained here and from the previous visualization in §3.1.3 for a pure plume.

Table 4.1: Comparison between scales estimated by PIV measurement and visualization.

Variable	Correlation analyzed here	Visualization[1]	Difference [%]
characteristic length $\mathcal{L}$ [mm]	$\simeq 27$[2]	$\simeq 42$	55
characteristic velocity $\mathcal{U}$ [mm/s]	$\simeq 18$	$\simeq 22$	22
Macrostructure time scale τ_{eddy} [s]	$\simeq 1.5$[3]	$\simeq 1.85$	35

The scales estimated here by PIV measurement and turbulent correlation certainly have more credibility than the scales estimated by the visualization. In the plume visualization experiment, the images are recorded by a commercial (phone) camera, and both the FOV and the depth of focus are large, making estimating lengths in the image quite difficult due to *perspective distortion*. The fact can be easily checked by looking at Fig. 3.6. In those photos, the depth of focus is large enough to make the bottom of the water tank completely visible (and clear), complicating the estimation of length scales in the flow (it would be wrong to use the lengths at the bottom of the photo to estimate the lengths of the plume, which is at the center of the photo).

4.2 The Entrainment Coefficient

This section answers the research question of the current study. First, in §4.2.1, several variables in profile coefficient calculation are checked and will be shown to be consistent

[1] see §3.1.3
[2] estimated from Fig. 4.11e
[3] estimated from Fig. 4.12b

with the previous mean flow analysis. Then, the entrainment coefficient, obtained by both the new theory and the old theory, will be analyzed in §4.2.2.

4.2.1 Profile Coefficients Calculation Validation

This subsection checks several variables that are used to calculate the entrainment coefficient and compares the results in the previous section. Specifically, the characteristic velocity u_{zc} and buoyancy b_c will be checked. In previous mean flow analysis, these two variables are obtained by directly fitting a Gaussian function to the velocity and buoyancy field. However, in theories that determine the entrainment coefficient (both old and new theories), these variables are computed through the volume flux, momentum flux, and buoyancy flux (Eq. 2.16). Since it has been discovered that it is possible to have a misleading flux result from numerical integration (Virtanen et al., 2020), variables predicted by fluxes should be compared against the direct results from curve-fitting to validate the calculation. As a result, the two variables have been chosen to perform the validation because their calculations require numerically integrating the velocity field and buoyancy field.

Using the pure plume (case No. 17) as an example, its characteristic velocity u_{zc} and buoyancy b_c predicted by fluxes (in black points) are plotted in Fig. 4.13. In the same figure, the characteristic velocity u_{zc} and buoyancy b_c predicted by Gaussian curve fitting are plotted as red points. It can be seen from the figure that the Gaussian fitting predicted value is about two times larger than the value calculated by fluxes.

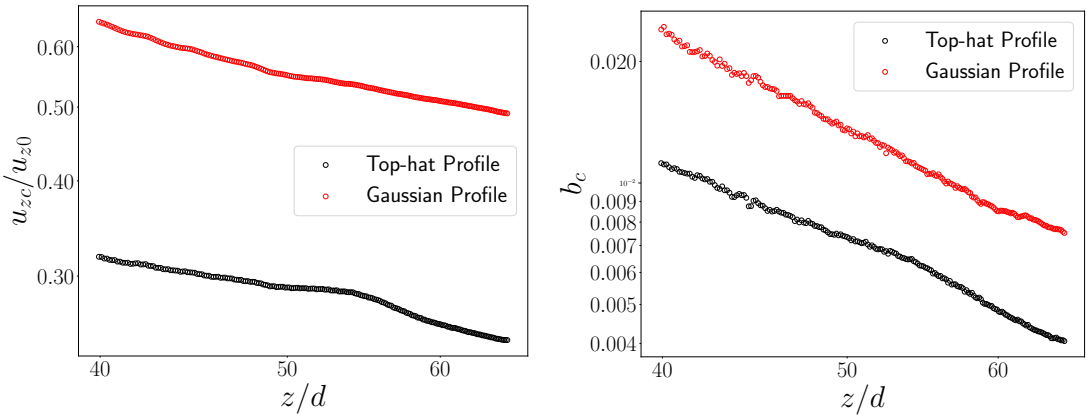

(a) Centerline velocity comparison.

(b) Centerline buoyancy comparison.

Figure 4.13: Values of u_{zc} and b_c given by Gaussian curve fitting and the theory.

Indeed, Fig. 4.14 plots the ratio of Gaussian predicted value to fluxes predicted value, which confirms this observation. This result is not surprising; after all, the value predicted by fluxes is consistent with the so-called *top-hat profile* convention (Reeuwijk & Craske, 2015), whereas the value predicted by curve fitting is clearly consistent with

the *Gaussian profile* convention. And Henderson-Sellers (1981) showed that centerline velocity and buoyancy associated with top hat profile is two times lower than with the Gaussian profile. Therefore, the fluxes predicted results are consistent with the curve fitting result, proving that the calculation is valid (no numerical integration pitfalls).

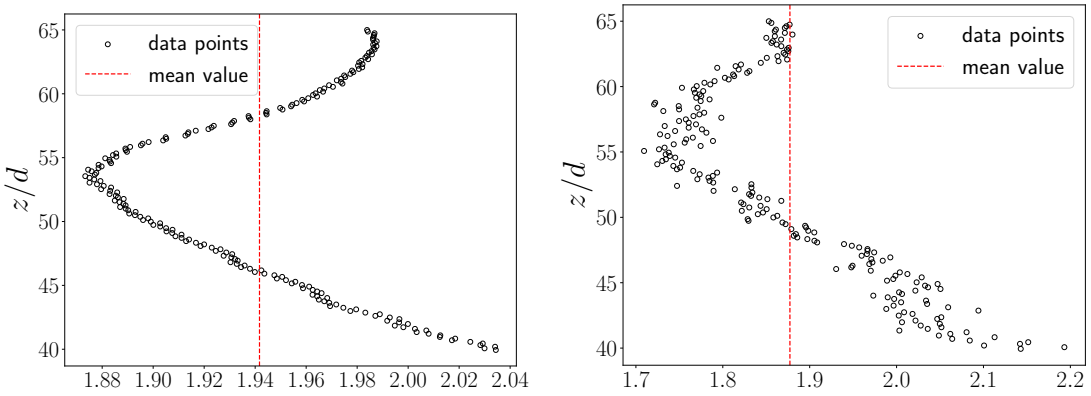

(a) Centerline velocity ratio of Gaussian profile to top-hat profile.

(b) Centerline buoyancy ratio of Gaussian profile to top-hat profile.

Figure 4.14: Ratio of Gaussian curve fitting predicted values to theory predicted values.

4.2.2 Calculate the Entrainment Coefficient

Fig. 4.15 gives the entrainment coefficient calculated by the new theory (Eq. 2.18) and the old theory (Eq. 2.19) for the three cases analyzed previously. There are several observations. First, the measured entrainment coefficient in all plumes is approximately 0.11, which agrees with other studies (Kaye, 2008; Richardson & Hunt, 2022). Both the old theory and the new theory give an entrainment coefficient value of around 0.11. Indeed, table 4.2 summarizes the entrainment coefficient of all measurements. It can be seen that the entrainment coefficient takes a value of 0.11.

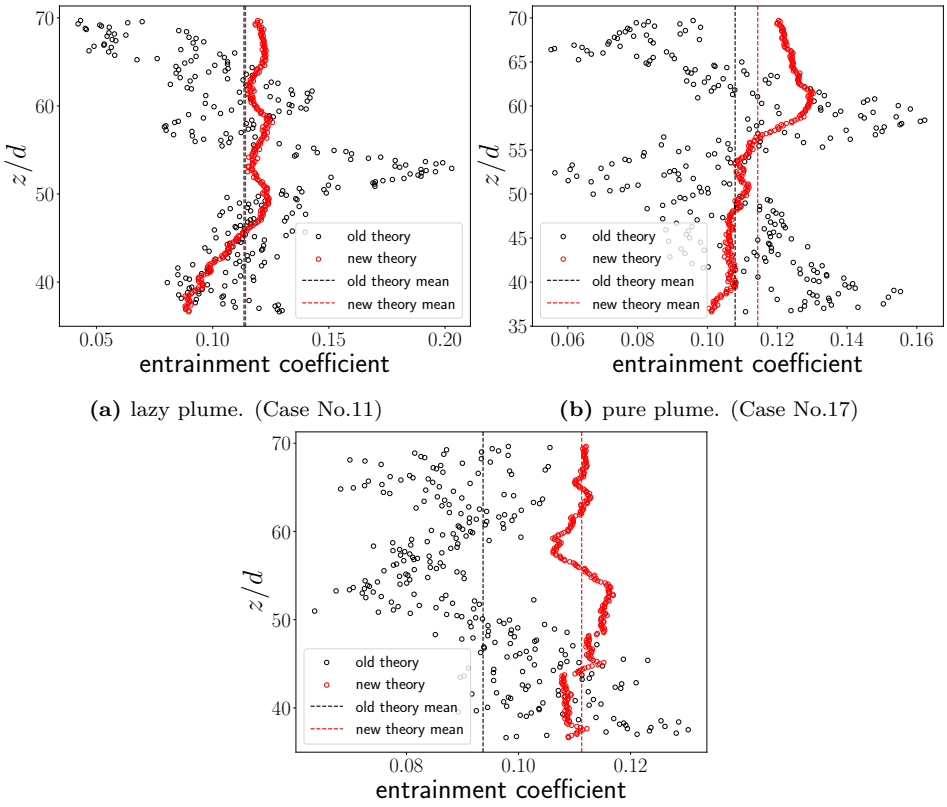

(a) lazy plume. (Case No.11)

(b) pure plume. (Case No.17)

(c) forced plume. (Case No.19)

Figure 4.15: Entrainment coefficient for typical plumes.

Table 4.2: Measured entrainment coefficients.

Case No.	α New Theory	α old Theory	α Std. New Theory	α Std. Old Theory
11	0.1142	0.1135	0.0106	0.0324
12	0.1143	0.1059	0.0089	0.0346
13	0.1340	0.1051	0.0137	0.0336
15	0.1274	0.0737	0.0124	0.0360
17	0.1144	0.1079	0.0088	0.0241
18	0.1058	0.1027	0.0035	0.0202
19	0.1113	0.0937	0.0027	0.0135
20	0.1357	0.1071	0.0082	0.0245

Second, it is evident that there can be substantial variations when using the old theory to determine the entrainment coefficient compared to the old theory, see Fig. 4.15 and standard deviations summarized in table 4.2 (the standard deviation is defined as $\sqrt{\frac{1}{N}\sum_{i=1}^{N}(x_i-\mu)^2}$, where$\mu = \frac{1}{N}\sum_{i=1}^{N} x_i$ and N is the size of the population). This observation may help explain why many variations were observed in previous studies (Richardson & Hunt, 2022), as these studies had mainly used the old theory to determine the entrainment coefficient (see table 1.1).

In hindsight, these large variations may stem from the absence of buoyancy in the old theory. The new theory (Eq. 2.18) uses two terms to determine the entrainment coeffi-

cient: the first term $-\frac{\delta_m}{2\gamma_m}$ contributes to the entrainment through turbulent production (the velocity field only), and the second term $\left(1-\frac{\theta_m}{\gamma_m}\right)\Gamma$ is designed to be consistent with the buoyancy effect (the buoyancy field). On the other hand, the old theory relies solely on the velocity field, failing to take the buoyancy effect into account.

One natural inference of the above reasoning is that one may also use $-\frac{\delta_m}{2\gamma_m}$ to predict the entrainment of a turbulent jet because it is the only non-zero term for a pure jet. At the same time, since the old theory does not consider any buoyancy effect, the old theory should be pretty good at predicting the entrainment coefficient of a pure turbulent jet. In other words, for the entrainment coeffcient resulting from the turbulence, both the term $-\frac{\delta_m}{2\gamma_m}$ and the old theory should be consistent. Since our plumes are turbulent, separating the turbulent production from buoyancy is possible by only considering the $-\frac{\delta_m}{2\gamma_m}$. Fig. 4.16 presents the term $-\frac{\delta_m}{2\gamma_m}$ versus the distance. It is clear that the entrainment coefficient resulting from the turbulence production in our experiments is 0.06. This is a remarkable result, because this value is consistent with the experiment done by Falcone and Cataldo (2003), who used the old theory to determine the entrainment coefficient of an axisymmetric jet and concluded the entrainment coefficient is 0.06.

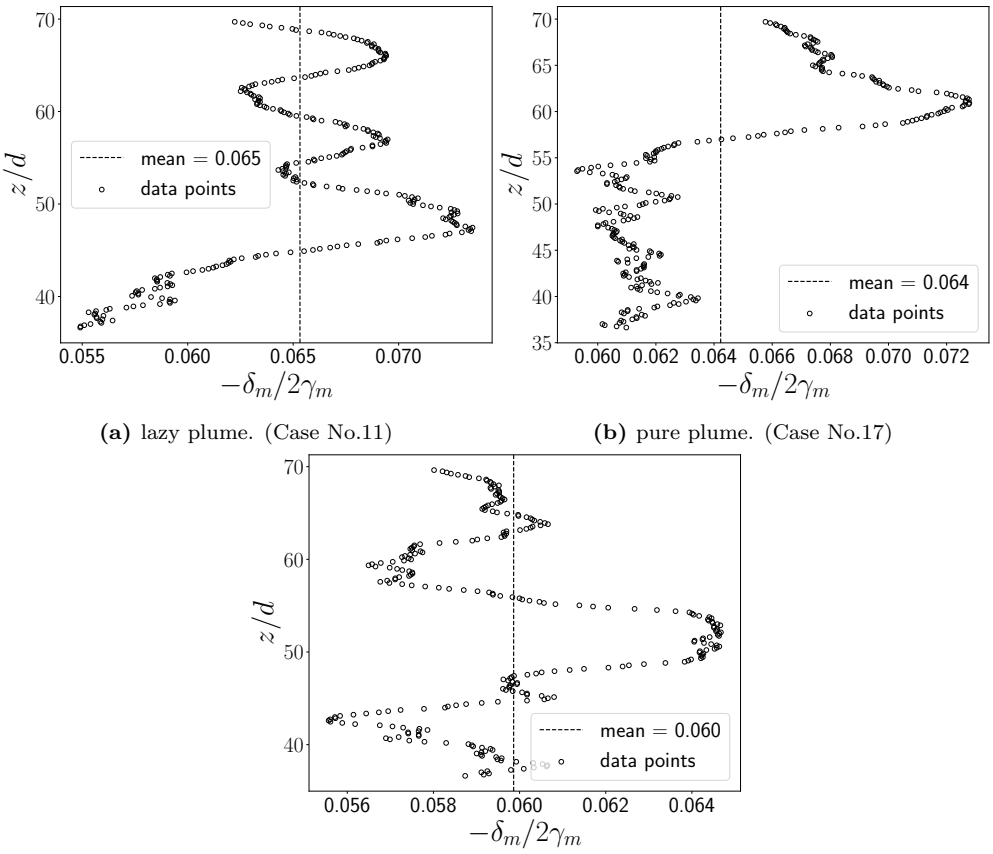

(a) lazy plume. (Case No.11)

(b) pure plume. (Case No.17)

(c) forced plume. (Case No.19)

Figure 4.16: Turbulence contribution for entrainment coefficient.

4.2.3 Local Richardson Number and Entrainment Coefficient

By examining the local Richardson number, which is a ratio of buoyancy to inertial force, this subsection tries to gain more insight into the plume evolution and to explain the contradictions raised by Figs. 4.5 and 4.10. In Figs. 4.5 and 4.10, it was observed that the initially lazy plume behaves like a forced plume (case No. 11) in the FOV, while the initially forced plume resembles a pure plume (case No. 19) in the FOV. This contradiction raised doubts about the plume evolution between FOV and the source, and the local Richardson number may help answer the doubts.

Fig. 4.17 gives the plot of local Richardson number Γ (Eq. 1.7) versus the distance from the nozzle. Fig. 4.17a shows that the initially lazy plume begins (rather counterintuitively) with a low Γ (around 0.7), which means that the plume has relatively strong inertial force and is forced at the entrance of the FOV. Furthermore, similar to the observation by Ezzamel et al. (2015), Γ in this case constantly increases and approaches unity (meaning that buoyancy stays relatively strong in the FOV). On the other hand, Fig. 4.17c seems to suggest that the initially forced plume starts with a Γ close to the unity (0.94), which means the plume has comparable buoyancy and inertial forces at the entrance of the FOV; furthermore, Γ begins to drop, meaning that buoyancy becomes relatively weaker in the FOV. The initially pure plume (Fig. 4.17b) lies in between the lazy plume and forced plume, with Γ hovering around unity (meaning buoyancy stays relatively comparable to inertial forces).

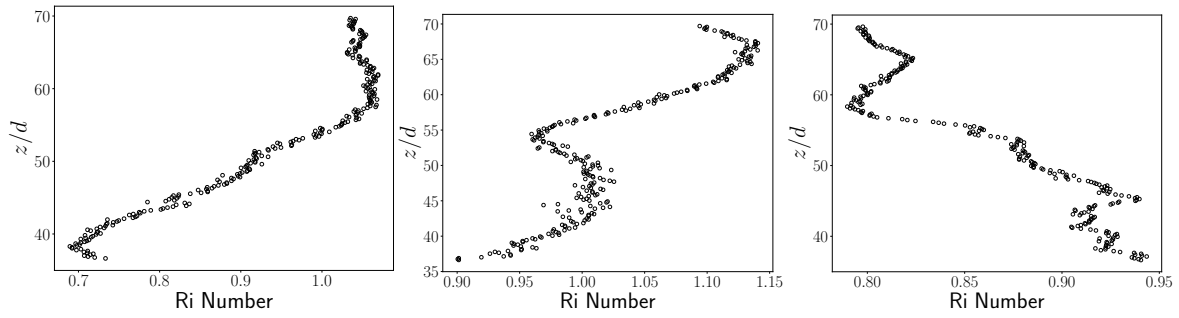

(a) lazy plume. (Case No.11) **(b)** pure plume. (Case No.17) **(c)** forced plume. (Case No.19)

Figure 4.17: Richardson number for typical plumes.

The above observation implies that, compared with the inertial force, the initially lazy plume seems to have relatively strong buoyancy, the initially pure seems to have relatively comparable buoyancy, and the forced plume seems to have relatively weak buoyancy. The following explanation from plume visualization shall provide some support for the above observations, yet further measurements performed at locations closer to the nozzle outlet should be used to confirm the following explanation.

One of the possible explanations is that because of the low initial velocity at the

nozzle outlet, the lazy plume and pure plume retain their buoyancy in the plume stream as the turbulence (which is good at mixing and reducing buoyancy) develops slower than that of a forced plume. In a forced plume (case No. 19), turbulence develops as soon as the plume leaves the nozzle, and the buoyancy starts decreasing its buoyancy due to turbulent mixing. Fig. 4.18 is a plume visualization (for a pure plume) that illustrates this phenomenon, and it can be seen that the turbulence did not develop until some distance away from the nozzle. Therefore, it is not surprising that lazy plume is observed to be "jet-like"; after all, compared with its forced plume counterparts, it has a relatively long distance to accelerate without losing its buoyancy due to turbulence.

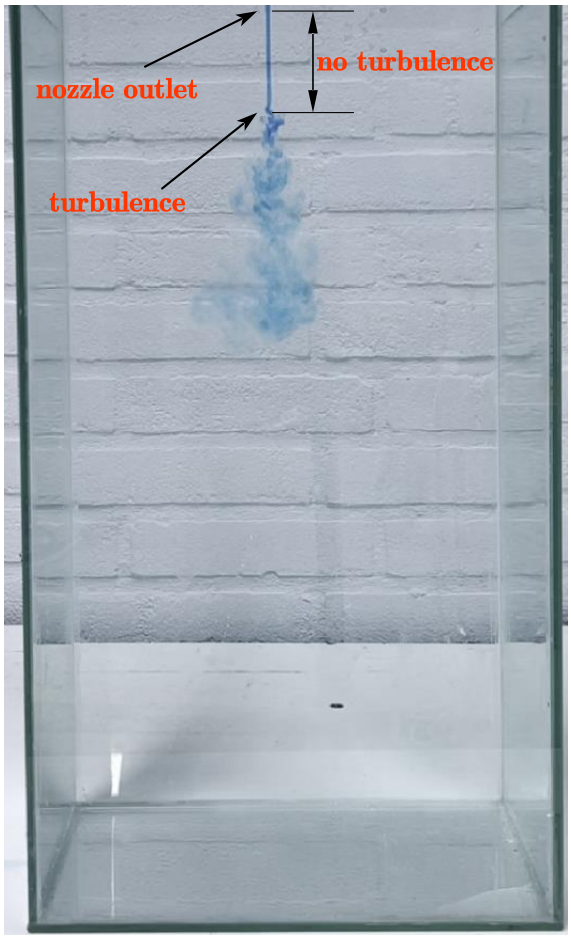

Figure 4.18: Turbulence develops after some distance from the nozzle. (The flow condition is the same as Case 11.)

4.3 Effect of RIM

This section analyzes the effect of refractive index matching (RIM). First, the direct effect of RIM on the quality of PIV measurement will be discussed. Then, the refractive index change's impact on the mean flow properties will be examined.

4.3.1 Effects on PIV Vector Goodness

When performing PIV image cross-correlation, interrogation window shifts that correspond to 4 highest correlation peaks are recorded as 4 different vector choices. As a rule of thumb, the first choice usually represents a good quality in terms of cross-correlation. As a result, all vectors that are not the first choice are considered as "bad vectors" in the following analysis.

Fig. 4.19 is the histogram of bad vectors observed in different images. It may be readily observed that RIM reduces the number of bad vectors. Indeed, a statistical t-test shows that $p \ll 0.05$, meaning that there is a statistically significant difference between the observed number of bad vectors for RIM and non-RIM. In other words, the RIM statistically reduces the number of bad vectors.

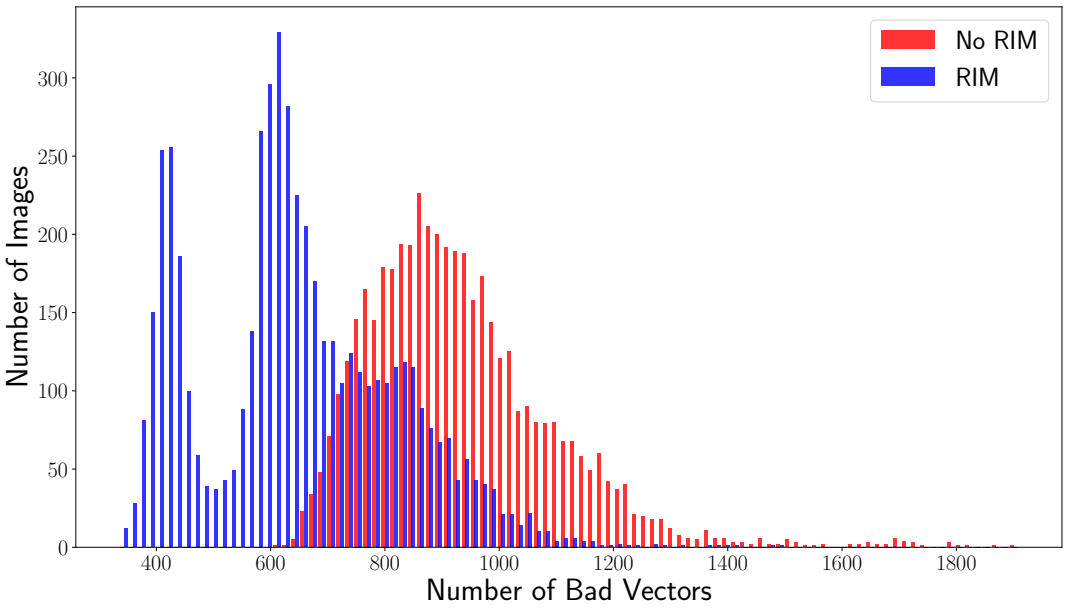

Figure 4.19: Histogram of bad vectors. In total, 5800 PIV vector field images are available for the statistical analysis because 580 PIV results are available for every pump speed, and there are 10 different pump speeds in either RIM or non-RIM experiment.

The increase in the number of bad vectors is not the only problem. These bad vectors tend to cluster together, which may lead to incorrect results if replaced by, for example, interpolation. Fig. 4.20 compares the original PIV image (no RIM) and the vector field result. In this figure, the original PIV image is plotted as the background, while bad vectors are shown in the yellow arrow (good vectors are omitted in the plot). As can be seen from the figure, blurred lumps cause the vector field to have bad vectors, and these bad vectors cluster together around the blurred lump. Since the calculation of fluxes requires numerical integration (and thus interpolation), these bad vectors may lead to erroneous results.

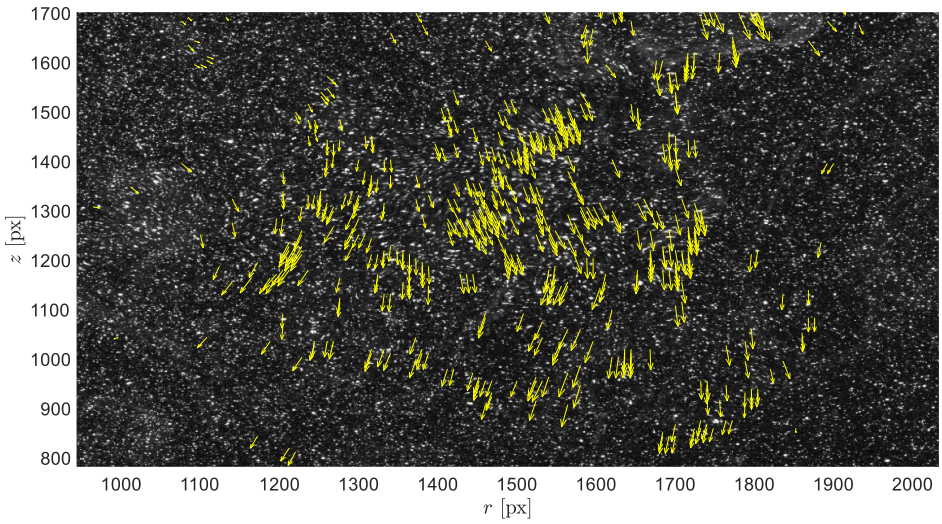

Figure 4.20: A comparison of PIV original image (no RIM) and the positions of bad vectors.

4.3.2 Effects on Turbulent Statistics

As mentioned before, it was found that the distortion of particle blur may lead to velocity and position errors. There is every reason to believe that non-RIM experiments may give different turbulent statistical results than RIM experiments. This subsection examines the effect of RIM on mean flow properties, and we start with the velocity field.

Effect on Mean Velocity Field

Fig. 4.21 shows the velocity profiles at different distances. All blue points are data from the RIM measurement, while all red points are data from the non-RIM measurement. It seems that the existence of a refractive index field acts to *overestimate* the velocity magnitude. This observation is consistent with the previous observation by Mishra and Philip (2021).

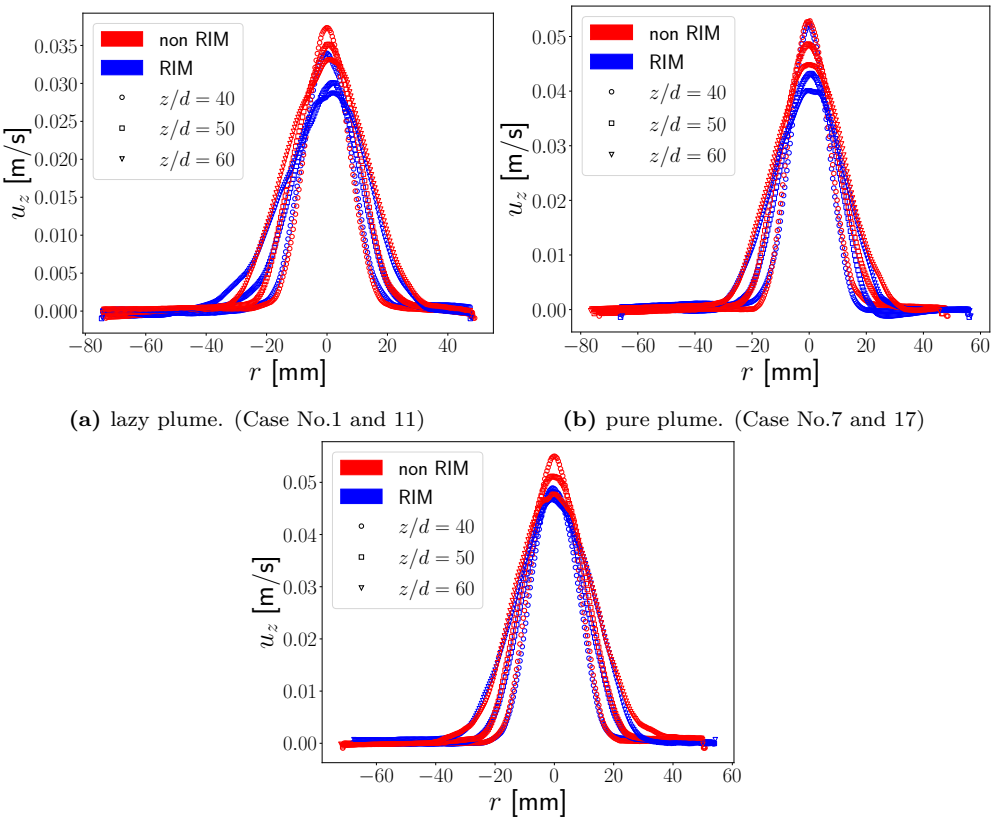

(a) lazy plume. (Case No.1 and 11)

(b) pure plume. (Case No.7 and 17)

(c) forced plume. (Case No.9 and 19)

Figure 4.21: Effects of RIM on velocity profiles.

Indeed, Fig. 4.22 plots the centerline velocity evolution over the vertical direction, and it is evident that non-RIM measurements overpredict the velocity. The result should not be surprising because, according to Elsinga et al. (2005), the velocity error contributes positively to the measured velocity if the velocity gradient and the position error are in the same (opposite) direction of the mean flow.

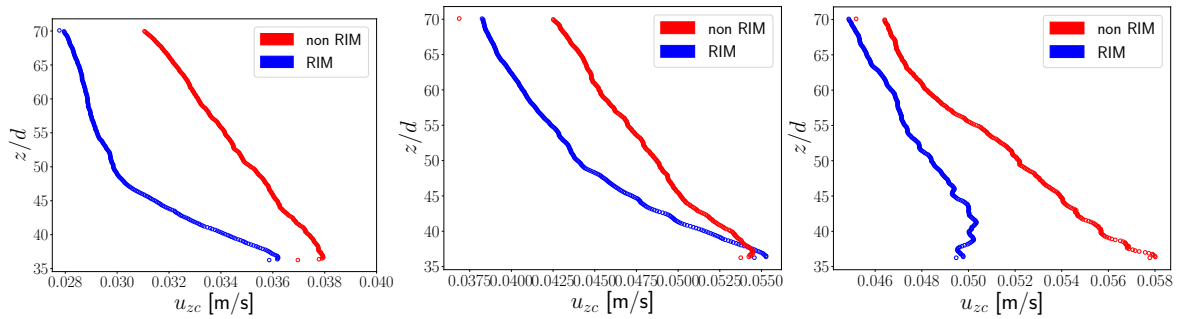

(a) lazy plume. (Case No.1 and 11)

(b) pure plume. (Case No.7 and 17)

(c) forced plume. (Case No.9 and 19)

Figure 4.22: Effects of RIM on centerline velocity.

Effect on Mean Buoyancy Field

RIM has a contrary effect on the mean buoyancy field. Fig. 4.23 plotted the mean buoyancy profiles at three different heights, with all red data points being non-RIM measurements and all blue data points being RIM measurements. It seems that the existence of a refractive index field *underestimates* the fluorescence intensity (and thus the buoyancy). Indeed, the centerline buoyancy evolution in Fig. 4.24 shows that non-RIM measurements generally have a lower centerline buoyancy.

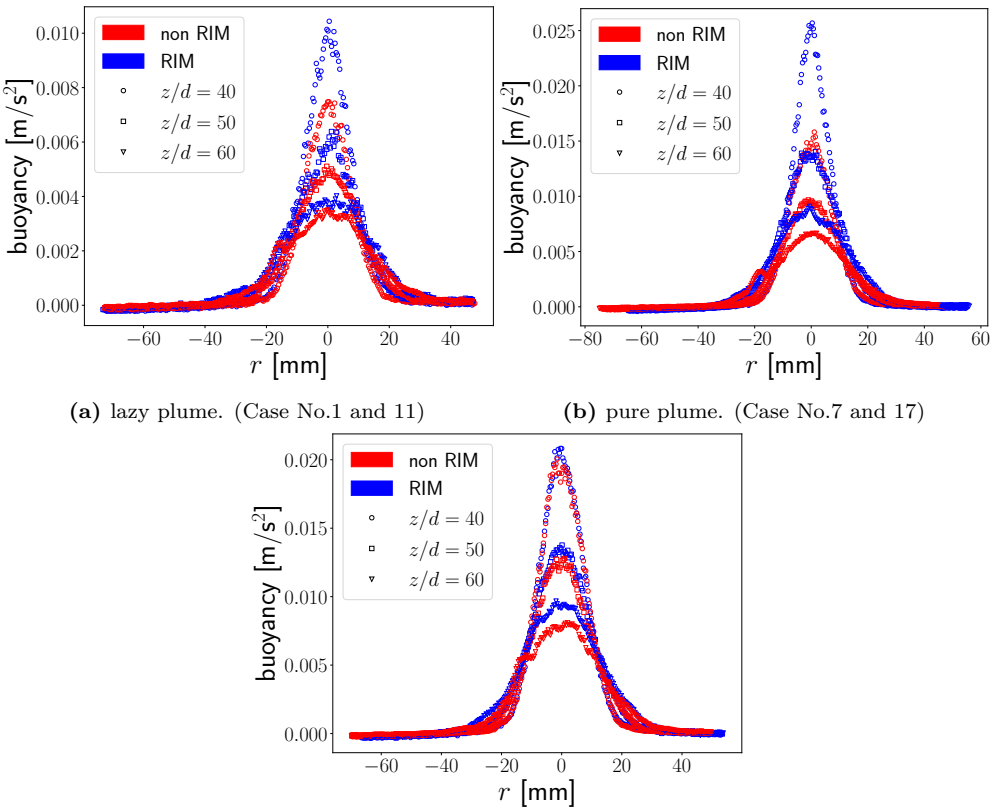

(a) lazy plume. (Case No.1 and 11)

(b) pure plume. (Case No.7 and 17)

(c) forced plume. (Case No.9 and 19)

Figure 4.23: Effects of RIM on buoyancy profiles.

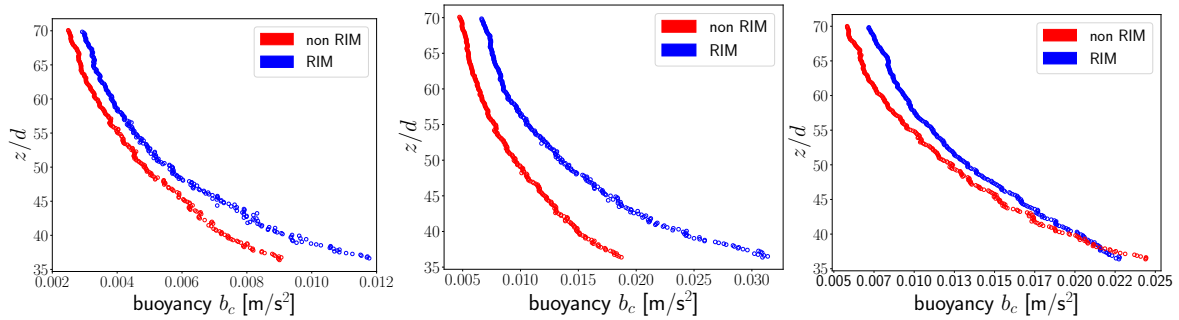

(a) lazy plume. (Case No.1 and 11)

(b) pure plume. (Case No.7 and 17)

(c) forced plume. (Case No.9 and 19)

Figure 4.24: Effects of RIM on centerline buoyancy.

The underestimation of buoyancy caused by the refractive index field is not surprising either; after all, some fluorescence must be diverted, causing the intensity perceived by the camera to reduce (note that the camera is calibrated without a refractive index field). Consider one fluorescence molecule in the plume. After it fluoresces, the fluorescence has to travel through a refractive index field to reach the camera. In both the radial and vertical directions, the refractive index field changes the ray path, causing the perceived intensity to change. Figs. 4.25 and 4.26 are the results of a simple ray path simulation, and it can be seen that the presence of an interface makes the perceived energy power (denoted as p) decrease. This result may explain why non-RIM measurements tend to underestimate buoyancy.

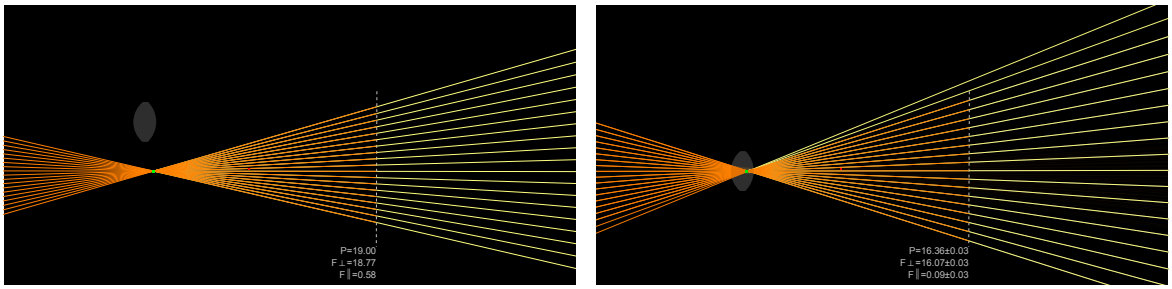

(a) With RIM. **(b)** Without RIM.

Figure 4.25: RIM effects on the ray path: radial direction.

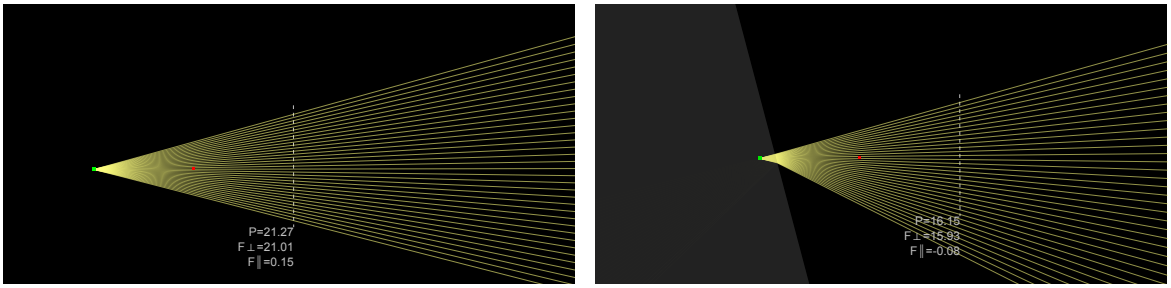

(a) With RIM. **(b)** Without RIM.

Figure 4.26: RIM effects on the ray path: vertical direction.

4.4 Comparison between CFD and Experiment

In the experiment setup design stage, a CFD simulation was carried out. This section compares the CFD simulation results and that of the experiment.

The CFD simulation uses a larger computational domain. A computational domain of a width of 300 mm and a height of 1000 mm has been used. The width in CFD is comparable to the experiment water tank, but the vertical dimension is almost two times larger than the experiment tank's height. The purpose of choosing a longer height is to prevent the boundary condition from influencing the simulation. In the CFD, the top

inlet condition is a uniform flow downwards, with the same velocity as the experiment; however, the outlet boundary condition is an outflow at the bottom of the computational domain, which is different from the experiment (a rising water level in the tank). The reason for using such an outlet boundary condition is to simplify the meshing procedure.

The CFD simulation uses the 2D unsteady RANS $k-\omega$ model with a structured mesh. In the computation domain, there are 99000 cells in total, and the mesh is a structured grid given the simple geometry; furthermore, a mesh convergence has been used to check the mesh quality. A time step of 0.01 seconds has been used to perfume the unsteady RANS $k-\omega$ calculation, and again, different time steps have been tested.

The CFD simulation uses the species transport module with a user-defined mixture to generate buoyancy. A mixture is defined, and its density is the same as in the experiment. The mass diffusion coefficient is kept the same as the mass diffusion coefficient of sodium sulfate reported in the literature.

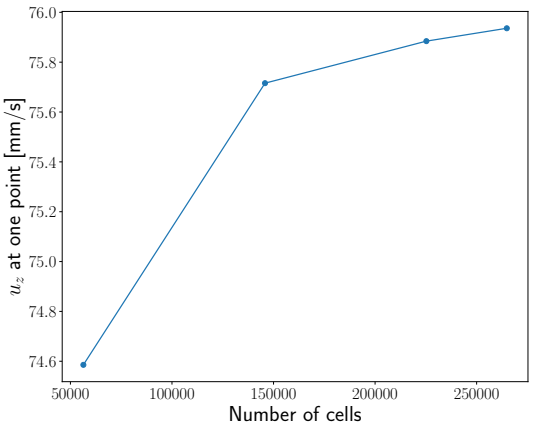

Figure 4.27: Mesh convergence plot.

Fig. 4.27 is the mesh convergence plot. One point in the flow field has been chosen, and the variations of the vertical velocity component are plotted against mesh number counts. It is clear that after a mesh with roughly 220000 cells, the variation in the velocity component is reasonably small, and the mesh convergence may be confirmed.

Fig. 4.28 is a typical result of the velocity field in CFD simuations. Apparently, the velocity magnitude is also much higher than in the experiment. Moreover, there is backflow in the CFD simulation as the plume floats up at the cap of the plume. The plume "collapse" feature was not observed in the experiment at all; instead, the filling box effect was seen in the plume, as mentioned in §3.1.1.

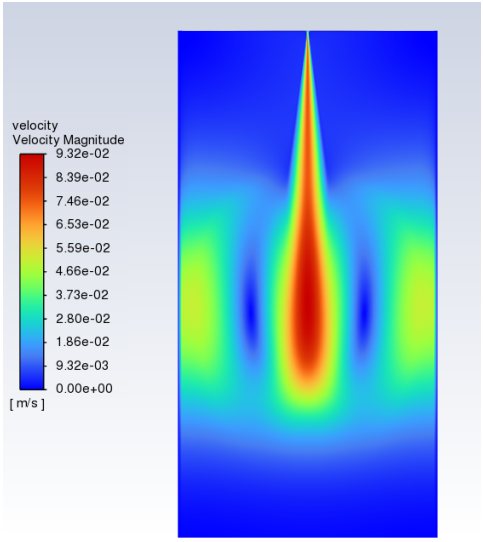

Figure 4.28: The velocity field from CFD simulation.

Indeed, the velocity profiles at the same distance from the nozzle outlet confirm that the velocity magnitude in CFD is much higher than in the experiment. Fig. 4.29 shows the velocity profiles at three different locations, with red points denoting the CFD result and blue points denoting the experiment result. It is clear that the vertical velocity component in the CFD is more than two times higher than in the experiment. Furthermore, the centerline velocity in the CFD does not decrease over the distance, which stands in contrast to the decreasing centerline velocity in PIV measurements.

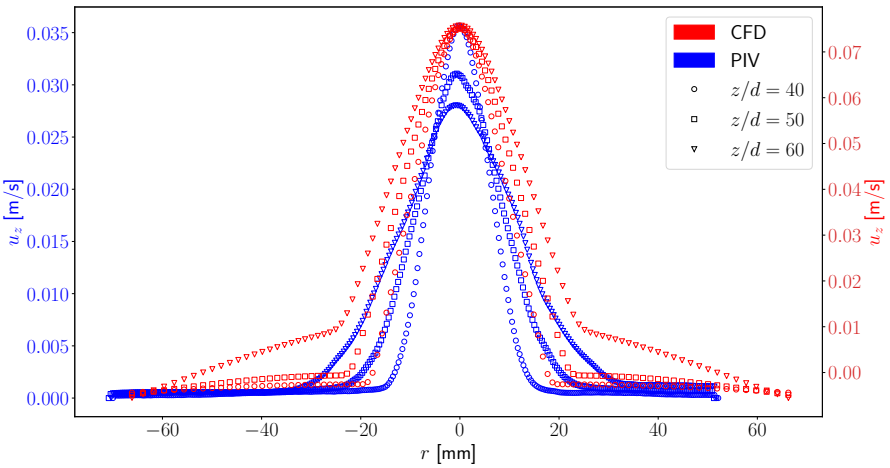

Figure 4.29: Velocity profiles at three different locations in PIV and CFD.

In conclusion, the present CFD simulation has proven inadequate in accurately capturing flow in the experiment. This outcome suggests limitations or inaccuracies within the CFD model, possibly due to factors like assumptions, boundary conditions, numerical errors, etc. Yet, further investigation should be warranted to identify the causes of this disparity, highlighting the need for refinement and validation of simulation models.

5

Conclusion and Outlook

5.1 Conclusion

A buoyancy-driven plume was created in a water tank. The plume was created by injecting a dilute solution with a higher density into a cuboid tank full of ambient fluid with a lower density. Depending on whether RIM was used, the densities of the plume and the ambient fluid were different. For non-RIM experiments, the plume was a wt% = 6% sodium sulfate solution, while the ambient fluid was pure water, and this combination generated a density difference of 55.6 kg/m^3 at the injection point. For RIM experiments, the plume was a wt% = 8.46% sodium sulfate solution, while the ambient fluid was a wt% = 8.59% urea solution, and this combination was able to generate a same density difference as in the non-RIM experiments at the injection point.

A combined PIV and LIF technique was employed to measure the velocity and buoyancy field of the plume, respectively. The PIV system followed a standard approach for the velocity measurement, and the data processing procedure was similar to typical workflow. For the measurement of buoyancy using the LIF system, the selection of fluorescence must ensure that the mass transfer of fluorescence matched that of the sodium sulfate so that the measured fluorescence dye concentration could be converted into sodium sulfate concentration. As a result, Rhodamine 6G was selected as the fluorescence dye because it shares similar mass transfer properties with sodium sulfate and is not significantly affected by variations in temperature. Eventually, the buoyancy value could be obtained by converting sodium sulfate concentration to density difference.

The entrainment coefficient value was obtained with two different approaches. The first approach (called the old method) is the original theory for entrainment coefficient

calculation, which was proposed by Morton et al. (1956) and relies solely on the measurement of the velocity field. The second approach (called the new method) is the recently developed theory on entrainment coefficient calculation, which considers not only the velocity field but also the buoyancy field (Reeuwijk & Craske, 2015). Both approaches showed that the mean entrainment coefficient is 0.11, which was consistent with a recent meta-analysis by Richardson and Hunt (2022). Although the two theories gave the same mean value of the entrainment coefficient, the old method presented larger standard deviations around the mean value, which might help explain large variations in the entrainment coefficient in past studies.

The contribution of the local Richardson number on the entrainment coefficient was separated and confirmed. The new method successfully decomposes contributions to the entrainment coefficient into two parts: the contribution from the turbulent production term and the term associated with the local Richardson number. Since the turbulent production term is the only non-zero term in a turbulent jet, the thesis compared our results with the entrainment coefficient in a pure jet measured by Falcone and Cataldo (2003), and the results showed reasonably good consistency. Because there are only two terms in the entrainment coefficient decomposition, by proving the validity of the first term in the decomposition, the results also confirmed the validity of the second term, which links the local Richardson number with the buoyancy profile and velocity profile.

The existence of a refractive index field was observed to affect both the velocity and the buoyancy measurement. For the velocity measurement, non-RIM measurements had a statistically significant larger number of bad velocity vectors; furthermore, these bad velocity vectors tend to cluster around the blurred lumps in the images. In addition, non-RIM measurements tended to overestimate the velocity magnitude but underestimate the buoyancy magnitude.

Large discrepancies were observed between the experiment and the unsteady RANS simulation. The CFD simulation yielded velocity results that did not match both the PIV measurements and the plume visualization; neither did it show the typical decaying feature of centerline velocity. Therefore, the simulation was erroneous. The reason for the failed CFD simulation remains unclear.

5.2 Outlook

Further measurements above the current measurement regions should be performed to investigate the plume's evolution. As mentioned in previous chapters, the plume's pattern (lazy, pure, or forced) was observed to be different in the measurement region and at the nozzle outlet. While one possible explanation based on the plume visualization was provided, it may not be possible to draw a concrete conclusion without additional

measurements taken at a location higher than the current measurement point.

A more comprehensive CFD study may be necessary to determine the reason for discrepancies between simulation and experiments. In the current study, lots of simplifications were used in the CFD simulation, such as the different outlet boundary conditions or the use of a RANS model. In order to improve the accuracy of the CFD simulation and ultimately compare its results with experimental data, it should be advisable to utilize a more advanced model, such as a large eddy simulation, in a three-dimensional space.

Moreover, the Reynolds stress and turbulent/non-turbulent interface (TNTI) detection may be utilized to provide more information regarding the entrainment coefficients. The Reynolds stress resulting from the PIV measurements can be potentially useful when explaining the turbulent dynamics and momentum transfer. The TNTI, once successfully detected by choosing proper thresholds, can be used to examine the conditional statistics (such as the conditionally averaged velocity and buoyancy profiles), which may give more insights into the entrainment coefficients.

References

Abdalla, I. E., Cook, M. J., & Hunt, G. R. (2009). Numerical Study of Thermal Plume Characteristics and Entrainment in an Enclosure with a Point Heat Source. *Engineering Applications of Computational Fluid Mechanics*, *3*(4), 608–630. https://doi.org/10.1080/19942060.2009.11015294

Abdelhamed, A. S., Yassen, Y. E.-S., & ElSakka, M. M. (2015). Design optimization of three dimensional geometry of wind tunnel contraction. *Ain Shams Engineering Journal*, *6*(1), 281–288. https://doi.org/10.1016/j.asej.2014.09.008

Barnett, S. J. (1992). *Dynamics of buoyant releases in confined spaces.* (Thesis) [Accepted: 2015-10-15T09:07:56Z]. University of Cambridge. https://doi.org/10.17863/CAM.16149

Bejan, A. (2013). *Convection Heat Transfer*. John Wiley & Sons, Incorporated. Retrieved February 27, 2023, from http://ebookcentral.proquest.com/lib/delft/detail.action?docID=7103548

Bergman, T. L., Lavine, A. S., Incropera, F. P., & DeWitt, D. P. (2018). *Fundamentals of Heat and Mass Transfer* (8th Edition). Wiley. https://www.wiley.com/en-us/Fundamentals+of+Heat+and+Mass+Transfer%2C+8th+Edition-p-9781119353881

C. Beaumont, P., G. Johnson, D., & J. Parsons, B. (1993). Photophysical properties of laser dyes: Picosecond laser flash photolysis studies of Rhodamine 6G, Rhodamine B and Rhodamine 101 [Publisher: Royal Society of Chemistry]. *Journal of the Chemical Society, Faraday Transactions*, *89*(23), 4185–4191. https://doi.org/10.1039/FT9938904185

Carey, S. N., Sigurdsson, H., & Sparks, R. S. J. (1988). Experimental studies of particle-laden plumes. *Journal of Geophysical Research: Solid Earth*, *93*(B12), 15314–15328. https://doi.org/10.1029/JB093iB12p15314

Chrzan, J. C. (2012). Laser-induced fluorescence measurements of dual plumes and comparison of laser-induced fluorescence and conductivity probe measurements [Accepted: 2012-09-20T18:22:18Z Publisher: Georgia Institute of Technology]. Retrieved February 2, 2023, from https://smartech.gatech.edu/handle/1853/44857

Contini, D., Donateo, A., Cesari, D., & Robins, A. G. (2011). Comparison of plume rise models against water tank experimental data for neutral and stable crossflows. *Journal of Wind Engineering and Industrial Aerodynamics*, *99*(5), 539–553. https://doi.org/10.1016/j.jweia.2011.02.003

Craske, J., & Reeuwijk, M. v. (2015). Energy dispersion in turbulent jets. Part 1. Direct simulation of steady and unsteady jets [Publisher: Cambridge University Press]. *Journal of Fluid Mechanics*, *763*, 500–537. https://doi.org/10.1017/jfm.2014.640

Craske, J., Salizzoni, P., & Reeuwijk, M. v. (2017). The turbulent Prandtl number in a pure plume is 3/5 [Publisher: Cambridge University Press]. *Journal of Fluid Mechanics*, *822*, 774–790. https://doi.org/10.1017/jfm.2017.259

Crimaldi, J. P. (2008). Planar laser induced fluorescence in aqueous flows. *Experiments in Fluids*, *44*(6), 851–863. https://doi.org/10.1007/s00348-008-0496-2

Dadonau, M., Partridge, J., & Linden, P. (2019). The effect of double diffusion on entrainment in turbulent plumes. *Journal of Fluid Mechanics*. https://doi.org/10.1017/jfm.2019.925

Davidson, P. A. (A. (2004). *Turbulence: An introduction for scientists and engineers*. Oxford University Press. Retrieved December 19, 2022, from https://search.ebscohost.com/login.aspx?direct=true&scope=site&db=nlebk&db=nlabk&AN=843590

Dellino, P., Dioguardi, F., Mele, D., D'Addabbo, M., Zimanowski, B., Büttner, R., Doronzo, D. M., Sonder, I., Sulpizio, R., Dürig, T., & La Volpe, L. (2014). Volcanic jets, plumes, and collapsing fountains: Evidence from large-scale experiments, with particular emphasis on the entrainment rate. *Bulletin of Volcanology*, *76*(6), 834. https://doi.org/10.1007/s00445-014-0834-6

Dey, A. K. (2018). Cooling Towers: Basics, Common terms, Factors Affecting, Cooling Tower Types, Natural Draft Cooling Towers (PDF). Retrieved January 18, 2023, from https://whatispiping.com/cooling-tower-and-cooling-water-system-1/

Dixon, J. M., Taniguchi, M., & Lindsey, J. S. (2005). PhotochemCAD 2: A refined program with accompanying spectral databases for photochemical calculations. *Photochemistry and Photobiology*, *81*(1), 212–213. https://doi.org/10.1562/2004-11-06-TSN-361

Edmund, O. (2023). 525nm CWL, 50mm Dia, 15nm Bandwidth, OD 6 Fluorescence Filter. Retrieved July 13, 2023, from https://www.edmundoptics.eu/p/525nm-cwl-50mm-dia-15nm-bandwidth-od-6-fluorescence-filter/28801/

Elsinga, G. E., van Oudheusden, B. W., & Scarano, F. (2005). Evaluation of aero-optical distortion effects in PIV. *Experiments in Fluids*, *39*(2), 246–256. https://doi.org/10.1007/s00348-005-1002-8

Ezzamel, A., Salizzoni, P., & Hunt, G. R. (2015). Dynamical variability of axisymmetric buoyant plumes [Publisher: Cambridge University Press]. *Journal of Fluid Mechanics*, *765*, 576–611. https://doi.org/10.1017/jfm.2014.694

Falcone, A. M., & Cataldo, J. C. (2003). Entrainment Velocity in an Axisymmetric Turbulent Jet. *Journal of Fluids Engineering*, *125*(4), 620–627. https://doi.org/10.1115/1.1595674

Fan, Y., Wang, Q., Ge, J., & Li, Y. (2020). Conditions for transition from a plume to a dome above a heated horizontal area. *International Journal of Heat and Mass Transfer*, *156*, 119868. https://doi.org/10.1016/j.ijheatmasstransfer.2020.119868

Ferrier, A. J., Funk, D. R., & Roberts, P. J. W. (1993). Application of optical techniques to the study of plumes in stratified fluids. *Dynamics of Atmospheres and Oceans*, *20*(1), 155–183. https://doi.org/10.1016/0377-0265(93)90052-9

Figliola, R. S., & Beasley, D. E. (2014). *Theory and Design for Mechanical Measurements*. John Wiley & Sons.

Fox, D. G. (1970). Forced plume in a stratified fluid. *Journal of Geophysical Research (1896-1977)*, *75*(33), 6818–6835. https://doi.org/10.1029/JC075i033p06818

Gavish, N., & Promislow, K. (2016). Dependence of the dielectric constant of electrolyte solutions on ionic concentration: A microfield approach. *Physical Review E*, *94*(1), 012611. https://doi.org/10.1103/PhysRevE.94.012611

Gebhart, B., Pera, L., & Schorr, A. W. (1970). Steady laminar natural convection plumes above a horizontal line heat source. *International Journal of Heat and Mass Transfer*, *13*(1), 161–171. https://doi.org/10.1016/0017-9310(70)90032-3

George, W. K., Jr., Alpert, R. L., & Tamanini, F. (1977). Turbulence measurements in an axisymmetric buoyant plume [ADS Bibcode: 1977IJHMT..20.1145G]. *International Journal of Heat and Mass Transfer*, *20*, 1145–1154. Retrieved July 1, 2023, from https://ui.adsabs.harvard.edu/abs/1977IJHMT..20.1145G

Haynes, W. M. (Ed.). (2016). *CRC Handbook of Chemistry and Physics* (97th ed.). CRC Press. https://doi.org/10.1201/9781315380476

Henderson-Sellers, B. (1981). Shape constants for plume models. *Boundary-Layer Meteorology*, *21*(1), 105–114. https://doi.org/10.1007/BF00119371

Jaluria, Y. (1980). *Natural Convection: Heat and Mass Transfer*. Elsevier Science & Technology.

Jiao, Z., Zhao, J., Chao, Z., You, Z., & Zhao, J. (2019). An air-chamber-based microfluidic stabilizer for attenuating syringe-pump-induced fluctuations. *Microfluidics and Nanofluidics*, *23*(2), 26. https://doi.org/10.1007/s10404-019-2193-2

Kang, Y. J., Yeom, E., Seo, E., & Lee, S.-J. (2014). Bubble-free and pulse-free fluid delivery into microfluidic devices. *Biomicrofluidics*, *8*(1), 014102. https://doi.org/10.1063/1.4863355

Kaye, N. B. (2008). Turbulent Plumes in Stratified Environments: A Review of Recent Work. *ATMOSPHERE-OCEAN*, *46*(4), 433–441. https://doi.org/10.3137/ao.460404

Kewalramani, G., Pant, C. S., & Bhattacharya, A. (2022). Energy consistent Gaussian integral model for jet with off-source heating [Publisher: American Physical Society]. *Physical Review Fluids*, *7*(1), 013801. https://doi.org/10.1103/PhysRevFluids.7.013801

Klespitz, J., & Kovács, L. (2014). Peristaltic pumps — A review on working and control possibilities. *2014 IEEE 12th International Symposium on Applied Machine Intelligence and Informatics (SAMI)*, 191–194. https://doi.org/10.1109/SAMI.2014.6822404

Kumar, R. K., Chiang, H. W., & Kalos, F. (1996). Entrainment and Mixing in Vertical Buoyant Light-Gas Plumes. *Journal of Energy Resources Technology*, *118*(1), 77–81. https://doi.org/10.1115/1.2792697

LaVision, G. (2023). Cameras for PIV. Retrieved April 21, 2023, from https://www.lavision.de/en/products/cameras/cameras-for-piv/

Li, X., Gurgenci, H., Guan, Z., Wang, X., & Xia, L. (2019). A review of the crosswind effect on the natural draft cooling towers. *Applied Thermal Engineering*, *150*, 250–270. https://doi.org/10.1016/j.applthermaleng.2018.12.147

Liu, T., Huang, J., Ding, H., Zhan, C., & Wang, S. (2022). Molecular structure perspective on Temperature-Sensitive properties of rhodamine aqueous solutions. *Spectrochimica Acta Part A: Molecular and Biomolecular Spectroscopy*, *275*, 121166. https://doi.org/10.1016/j.saa.2022.121166

Mayinger, F., Feldmann, O., Mewes, D., & Mayinger, F. (Eds.). (2001). *Optical Measurements*. Springer. https://doi.org/10.1007/978-3-642-56443-7

Melton, L. A., & Lipp, C. W. (2003). Criteria for quantitative PLIF experiments using high-power lasers. *Experiments in Fluids*, *35*(4), 310–316. https://doi.org/10.1007/s00348-003-0632-y

Milton-McGurk, L., Williamson, N., Armfield, S. W., & Kirkpatrick, M. P. (2022). Characterising entrainment in fountains and negatively buoyant jets [Publisher: Cambridge University Press]. *Journal of Fluid Mechanics*, *939*, A29. https://doi.org/10.1017/jfm.2022.152

Mishra, H., & Philip, J. (2021). Importance of Refractive Index Matching of Fluids for PIV and PLIF Measurements in Buoyant Jets. In L. Venkatakrishnan, S. Ma-

jumdar, G. Subramanian, G. S. Bhat, R. Dasgupta, & J. Arakeri (Eds.), *Proceedings of 16th Asian Congress of Fluid Mechanics* (pp. 277–284). Springer. https://doi.org/10.1007/978-981-15-5183-3_30

Morton, B. R., & Middleton, J. (1973). Scale diagrams for forced plumes [Publisher: Cambridge University Press]. *Journal of Fluid Mechanics*, *58*(1), 165–176. https://doi.org/10.1017/S002211207300220X

Morton, B. R., Taylor, G. I., & Turner, J. S. (1956). Turbulent gravitational convection from maintained and instantaneous sources [Publisher: Royal Society]. *Proceedings of the Royal Society of London. Series A. Mathematical and Physical Sciences*, *234*(1196), 1–23. https://doi.org/10.1098/rspa.1956.0011

Nesbitt, B. (Ed.). (2006a). 1 - Pump types. In *Handbook of Pumps and Pumping* (pp. 1–54). Elsevier Science Ltd. https://doi.org/10.1016/B978-185617476-3/50003-2

Nesbitt, B. (Ed.). (2006b). 5 - Pumps and piping systems. In *Handbook of Pumps and Pumping* (pp. 155–174). Elsevier Science Ltd. https://doi.org/10.1016/B978-185617476-3/50007-X

Nieuwstadt, F. T., Westerweel, J., & Boersma, B. J. (2016). *Turbulence: Introduction to Theory and Applications of Turbulent Flows*. Springer International Publishing. https://doi.org/10.1007/978-3-319-31599-7

Paillat, S., & Kaminski, E. (2014). Entrainment in plane turbulent pure plumes [Publisher: Cambridge University Press]. *Journal of Fluid Mechanics*, *755*, R2. https://doi.org/10.1017/jfm.2014.424

Parker, D. A., Burridge, H. C., Partridge, J. L., & Linden, P. F. (2020). A comparison of entrainment in turbulent line plumes adjacent to and distant from a vertical wall [Publisher: Cambridge University Press]. *Journal of Fluid Mechanics*, *882*, A4. https://doi.org/10.1017/jfm.2019.790

Paul, E. L., Atiemo-Obeng, V. A., & Kresta, S. M. (2004). 2.3.2 Turbulence Spectrum: Quantifying Length Scales. In *Handbook of Industrial Mixing - Science and Practice*. John Wiley & Sons. https://app.knovel.com/hotlink/pdf/id:kt007ENQG8/handbook-industrial-mixing/turbulence-spectrum-quantifying

Petracci, A., Delfos, R., & Westerweel, J. (2006). Combined PIV/LIF measurements in a Rayleigh-Bénard convection cell, 12.

Photonics Industries, I. (2023). DM Dual Head Series Nanosecond Lasers (Multi-Mode). Retrieved April 20, 2023, from https://www.photonix.com/product/dm-dual-head-green-series/

Plourde, F., Pham, M. V., Kim, S. D., & Balachandar, S. (2008). Direct numerical simulations of a rapidly expanding thermal plume: Structure and entrainment

interaction [Publisher: Cambridge University Press]. *Journal of Fluid Mechanics*, *604*, 99–123. https://doi.org/10.1017/S0022112008001006

Priestley, C. H. B., & Ball, F. K. (1955). Continuous convection from an isolated source of heat. *Quarterly Journal of the Royal Meteorological Society*, *81*(348), 144–157. https://doi.org/10.1002/qj.49708134803

Raffel, M., Willert, C. E., Scarano, F., Kähler, C. J., Wereley, S. T., & Kompenhans, J. (2018). *Particle Image Velocimetry: A Practical Guide*. Springer International Publishing. https://doi.org/10.1007/978-3-319-68852-7

Ramaprian, B. R., & Chandrasekhara, M. S. (1989). Measurements in Vertical Plane Turbulent Plumes. *Journal of Fluids Engineering*, *111*(1), 69–77. https://doi.org/10.1115/1.3243602

Reeuwijk, M. v., & Craske, J. (2015). Energy-consistent entrainment relations for jets and plumes [Publisher: Cambridge University Press]. *Journal of Fluid Mechanics*, *782*, 333–355. https://doi.org/10.1017/jfm.2015.534

Reynolds, A. J. (1962). Observations of a liquid-into-liquid jet [Publisher: Cambridge University Press]. *Journal of Fluid Mechanics*, *14*(4), 552–556. https://doi.org/10.1017/S0022112062001433

Richardson, J., & Hunt, G. R. (2022). What is the entrainment coefficient of a pure turbulent line plume? [Publisher: Cambridge University Press]. *Journal of Fluid Mechanics*, *934*, A11. https://doi.org/10.1017/jfm.2021.1070

Scase, M. M., Caulfield, C. P., & Dalziel, S. B. (2006). Boussinesq plumes and jets with decreasing source strengths in stratified environments [Publisher: Cambridge University Press]. *Journal of Fluid Mechanics*, *563*, 463–472. https://doi.org/10.1017/S0022112006000784

Schott. (2023). OG570 | SCHOTT Advanced Optics. Retrieved July 13, 2023, from https://www.schott.com/shop/advanced-optics/en/Matt-Filter-Plates/OG570/c/glass-OG570

Troy, C. D., & Koseff, J. R. (2005). The generation and quantitative visualization of breaking internal waves. *Experiments in Fluids*, *38*(5), 549–562. https://doi.org/10.1007/s00348-004-0909-9

Turner, J. S. (1973). *Buoyancy Effects in Fluids*. Cambridge University Press. https://doi.org/10.1017/CBO9780511608827

Virtanen, P., Gommers, R., Oliphant, T. E., Haberland, M., Reddy, T., Cournapeau, D., Burovski, E., Peterson, P., Weckesser, W., Bright, J., Van Der Walt, S. J., Brett, M., Wilson, J., Millman, K. J., Mayorov, N., Nelson, A. R. J., Jones, E., Kern, R., Larson, E., … Vázquez-Baeza, Y. (2020). SciPy 1.0: Fundamental

algorithms for scientific computing in Python. *Nature Methods*, *17*(3), 261–272. https://doi.org/10.1038/s41592-019-0686-2

Wilke, C. R., & Chang, P. (1955). Correlation of diffusion coefficients in dilute solutions [_eprint: https://onlinelibrary.wiley.com/doi/pdf/10.1002/aic.690010222]. *AIChE Journal*, *1*(2), 264–270. https://doi.org/10.1002/aic.690010222

Woods, A. W. (2010). Turbulent Plumes in Nature. *Annual Review of Fluid Mechanics*, *42*(1), 391–412. https://doi.org/10.1146/annurev-fluid-121108-145430

Zhang, W., He, Z., & Jiang, H. (2017). Scaling for turbulent viscosity of buoyant plumes in stratified fluids: PIV measurement with implications for submarine hydrothermal plume turbulence. *Deep Sea Research Part I: Oceanographic Research Papers*, *129*, 89–98. https://doi.org/10.1016/j.dsr.2017.10.006

A

Chapter 2 Equations Derivation

To derive the continuity equation (Eq. 2.10), apply the Reynolds decomposition

$$u_i = \overline{u_i} + u_i' \tag{A.1}$$

to the continuity equation (Eq. 2.7) to give

$$\frac{1}{r}\frac{\partial}{\partial r}\left[r\left(\overline{u_r} + u_r'\right)\right] + \frac{\partial}{\partial z}\left(\overline{u_z} + u_z'\right) = 0. \tag{A.2}$$

Take the average of the above formula to get

$$\overline{\frac{1}{r}\frac{\partial}{\partial r}\left[r\left(\overline{u_r} + u_r'\right)\right]} + \overline{\frac{\partial}{\partial z}\left(\overline{u_z} + u_z'\right)} = 0, \tag{A.3}$$

or

$$\frac{1}{r}\frac{\partial}{\partial r}\left(r\overline{u_r}\right) + \frac{1}{r}\frac{\partial}{\partial r}\left(r\overline{u_r'}\right) + \frac{\partial}{\partial z}\left(\overline{u_z}\right) + \frac{\partial}{\partial x}\left(\overline{u_z'}\right) = 0, \tag{A.4}$$

where $\frac{1}{r}\frac{\partial}{\partial r}\left(r\overline{u_r'}\right)$ and $\frac{\partial}{\partial z}\left(\overline{u_z'}\right)$ drop out. Hence we have Eq. 2.10:

$$\frac{1}{r}\frac{\partial}{\partial r}\left(r\overline{u_r}\right) + \frac{\partial \overline{u_z}}{\partial z} = 0.$$

To derive the stream-wise momentum equation (Eq. 2.11), first rewrite the LHS of

Eq. 2.8:

$$\begin{aligned}
&\frac{1}{r}\frac{\partial u_\theta u_z}{\partial \theta} - \frac{u_z}{r}\frac{\partial u_\theta}{\partial \theta} - u_z\frac{\partial u_z}{\partial z} + 2u_z\frac{\partial u_z}{\partial z} + \frac{1}{r}\frac{\partial u_\theta u_z}{\partial \theta} - \frac{u_z}{r}\frac{\partial u_\theta}{\partial \theta} - u_z\frac{\partial u_z}{\partial z} + 2u_z\frac{\partial u_z}{\partial z} \\
&= \left(\cancel{\frac{\partial u_z}{\partial t}} + \frac{1}{r}\frac{\partial r u_r u_z}{\partial r} + \cancel{\frac{1}{r}\frac{\partial u_\theta u_z}{\partial \theta}} + 2u_z\frac{\partial u_z}{\partial z}\right) - \cancel{\left(\frac{u_z}{r}\frac{\partial r u_r}{\partial r} + \frac{u_z}{r}\frac{\partial u_\theta}{\partial \theta} + u_z\frac{\partial u_z}{\partial z}\right)} \\
&= \frac{1}{r}\frac{\partial r u_r u_z}{\partial r} + 2u_z\frac{\partial u_z}{\partial z} \\
&= \frac{1}{r}\frac{\partial r u_r u_z}{\partial r} + \frac{\partial u_z^2}{\partial z},
\end{aligned}$$

then apply the Reynolds decomposition to give

$$\overline{\frac{1}{r}\frac{\partial}{\partial r}\left(r\left(\overline{u_z}+u_z'\right)\left(\overline{u_r}+u_r'\right)\right)} + \overline{\frac{\partial\left(\overline{u_z}+u_z'\right)^2}{\partial z}} = \frac{1}{r}\frac{\partial}{\partial r}\left(r\overline{u_z}\,\overline{u_r} + r\overline{u_z'u_r'}\right) + \frac{\partial}{\partial z}\left(\overline{u_z}\,\overline{u_z} + \overline{u_z'u_z'}\right). \tag{A.5}$$

For the RHS, the viscous term may be neglected due to the assumption of neglecting viscous effects. In other words, it is clear that after taking the average, the RHS becomes $-\frac{1}{\varrho}\frac{\partial \overline{p}}{\partial z} + g\frac{\overline{C}}{C_0}$. And now, Eq. 2.11 is obtained by combining the above results.

For the derivation of Eq. 2.12, one should notice that the LHS derivation is similar to the derivation of Eq. 2.11. The RHS becomes zero because the Peclet number, which is the product of the Reynolds number and the mass transfer Schmidt number, is very large under the assumption of neglecting viscous effect, and the diffusion term may be neglected.

To derive Eq. 2.13, multiply Eq. 2.11 with $\overline{u_z}$ on both sides

$$\frac{1}{r}\overline{u_z}\frac{\partial}{\partial r}\left(r\overline{u_z}\,\overline{u_r} + r\overline{u_z'u_r'}\right) + \overline{u_z}\frac{\partial}{\partial z}\left(\overline{u_z}\,\overline{u_z} + \overline{u_z'u_z'}\right) = -\frac{1}{\varrho}\overline{u_z}\frac{\partial \overline{p}}{\partial z} + g\overline{u_z}\frac{\overline{C}}{C_0}. \tag{A.6}$$

Now rewrite every term in the above equation. The first term on the LHS can be arranged as

$$\begin{aligned}
\frac{1}{r}\overline{u_z}\frac{\partial}{\partial r}\left(r\overline{u_z}\,\overline{u_r}\right) &= \frac{1}{r}\frac{\partial}{\partial r}\left(r\overline{u_z}\,\overline{u_z}\,\overline{u_r}\right) - \frac{1}{r}\overline{u_z}\,\overline{u_r}\frac{\partial}{\partial r}\left(r\overline{u_z}\right) \\
&= \frac{1}{r}\frac{\partial}{\partial r}\left(r\overline{u_z}^2\overline{u_r}\right) - \frac{1}{2}\frac{1}{r}\left(\frac{\partial}{\partial r}\left(r\overline{u_z}^2\overline{u_r}\right) - \overline{u_z}^2\frac{\partial}{\partial r}\left(r\overline{u_r}\right)\right) \\
&= \frac{1}{2}\frac{1}{r}\frac{\partial}{\partial r}\left(r\overline{u_z^2}\,\overline{u_r}\right) + \frac{1}{2}\frac{1}{r}\overline{u_z^2}\frac{\partial}{\partial r}\left(r\overline{u_r}\right).
\end{aligned} \tag{A.7}$$

The second term on the LHS can be arranged as

$$\frac{1}{r}\overline{u_z}\frac{\partial}{\partial r}\left(r\overline{u_z'u_r'}\right) = \frac{1}{r}\frac{\partial}{\partial r}\left(r\overline{u_z}\,\overline{u_z'u_r'}\right) - \overline{u_z'u_r'}\frac{\partial}{\partial r}\left(\overline{u_z}\right). \tag{A.8}$$

The third term on the LHS can be arranged as

$$\overline{u_z}\frac{\partial}{\partial z}\left(\overline{u_z u_z}\right) = \frac{\partial}{\partial z}\left(\overline{u_z}^3\right) - \overline{u_z}^2\frac{\partial}{\partial z}\left(\overline{u_z}\right). \tag{A.9}$$

The fourth term on the LHS can be arranged as

$$\overline{u_z}\frac{\partial}{\partial z}\left(\overline{u_z' u_z'}\right) = \frac{\partial}{\partial z}\left(\overline{u_z}\,\overline{u_z' u_z'}\right) - \overline{u_z' u_z'}\frac{\partial}{\partial z}\left(\overline{u_z}\right). \tag{A.10}$$

The first term on the RHS can be arranged as

$$-\overline{u_z}\frac{1}{\varrho}\frac{\partial \overline{p}}{\partial z} = -\frac{1}{\varrho}\frac{\partial}{\partial z}\left(\overline{u_z p}\right) + \frac{1}{\varrho}\overline{p}\frac{\partial \overline{u_z}}{\partial z}. \tag{A.11}$$

It should be noted that $\frac{\overline{p}}{\varrho}$ is the kinematic pressure and $\overline{p}$ shall be used denote kinematic pressure for simplicity. Combine Eqs. A.7 to A.11 and notice that

$$\begin{aligned}
\frac{1}{2}\frac{1}{r}\overline{u_z}^2\frac{\partial}{\partial r}\left(r\overline{u_r}\right) - \overline{u_z}^2\frac{\partial}{\partial z}\left(\overline{u_z}\right) &= -\frac{1}{2}\overline{u_z}^2\frac{\partial}{\partial z}\left(\overline{u_z}\right) - \overline{u_z}^2\frac{\partial}{\partial z}\left(\overline{u_z}\right) \\
&= -\frac{3}{2}\overline{u_z}^2\frac{\partial}{\partial z}\left(\overline{u_z}\right) \\
&= -\frac{1}{2}\frac{\partial}{\partial z}\left(\overline{u_z}^3\right),
\end{aligned}$$

then Eq. 2.13 can be obtained by multiplying a factor of 2.

To derive the Eqs. 2.14 and 2.15, one can follow the derivation by (Morton et al., 1956) except the fact that quantities such as momentum flux or buoyancy flux should include both the turbulence production and transport terms. For instance, the momentum flux

$$M_{\text{old}} \equiv 2\int_0^\infty u_z^2 r dr$$

originally defined by Morton et al. (1956) should now be modified to include the turbulence production contribution (Craske & Reeuwijk, 2015):

$$M \equiv 2\int_0^\infty \overline{u_z}^2 r dr + 2\int_0^\infty \overline{u_z' u_z'} r dr + 2\int_0^\infty \bar{p} r dr,$$

where the above two equations may be related by a profile coefficient β_g as

$$\beta_g \equiv \frac{M}{M_{\text{old}}} = \frac{M}{w_m^2 r_m^2} = \frac{1}{w_m^2 r_m^2}\left(M_{\text{old}} + 2\int_0^\infty \overline{u_z' u_z'} r dr + 2\int_0^\infty \bar{p} r dr\right).$$

It should be noted that $M_{\text{old}} = w_m^2 r_m^2$. Other equations are similar.